TECHNISCHE UNIVERSITÄT MÜNCHEN
Physik-Department
Lehrstuhl für Funktionelle Materialien (E13)

Influence of the short-range order on the atomic dynamics in metallic melts

Sandro Szabó

Vollständiger Abdruck der von der Fakultät für Physik der Technischen Universität München zur Erlangung des akademischen Grades eines

Doktors der Naturwissenschaften (Dr. rer. nat.)

genehmigten Dissertation.

Vorsitzender:	Prof. Dr. David Egger
Prüfer der Dissertation:	1. Prof. Dr. Winfried Petry
	2. Prof. Dr. Dirk Holland-Moritz

Die Dissertation wurde am 17.08.2020 bei der Technischen Universität München eingereicht und durch die Fakultät der Physik am 26.08.2020 angenommen.

dedicated to

Dr. Salomon Njemirovsky

Summary

Although diffusion is a fundamental property in physics and materials science, the diffusion mechanism in liquids is still not very well understood. For example, it is unclear how structural properties like the atomic packing, topological and chemical short-range order influence the atomic dynamics in metallic melts.

Objective of this work is a detailed study of the structure-dynamics relation in metallic melts, which were processed using containerless levitation techniques. Quasielastic neutron scattering (QENS), carried out at the multi-disc chopper time-of-flight spectrometer TOFTOF at Heinz Maier-Leibnitz Zentrum (MLZ), was used to study the atomic transport processes. In addition, structural investigations were conducted by neutron and synchrotron X-ray diffraction experiments.

QENS measurements on pure Mercury revealed that at the melting point the diffusion coefficient of pure metallic melts can be predicted according to atomic mass and packing fraction, when assuming similar dynamics like these of the alkali metals. The semi-empirical approach based on uncorrelated binary collisions, however, underestimates the activation energy of the temperature dependence of the diffusion.

Binary mixtures of the Zr-Ti system exhibit for all concentrations a similar atomic packing than pure Mercury. In Zr-rich mixtures, the Ti mobility obtained by QENS decreases with increasing Ti content. Structural investigations revealed, that barely any chemical short-range order is present in Zr-Ti melts. The concentration dependent dynamics can be fully understood according to the prediction of the mode-coupling theory (MCT) on a binary hard-sphere mixture and attributed to differences in the atomic radii, indicating a dominant impact of the topological structure on the atomic motion.

Melts of the Zr-Cu(-Al/Ti) system exhibit higher packing fractions than Mercury and Zr-Ti, what is accompanied by slower melt dynamics. Moreover, the minor addition of only 4 at.% Al or Ti to $Zr_{50}Cu_{50}$ melts lowers the self-diffusivity almost by a factor of two. Similar observations of slowing down of the dynamics upon minor Al addition can be made also on the melt viscosity. Despite the different dynamics, the static structure as well as the average packing fractions of $Zr_{50}Cu_{50}$ and $(Zr_{50}Cu_{50})_{96}(Ti, Al)_4$ melts are very similar. Therefore, whereas for Hg and Zr-Ti the dynamics can be understood by topological effects, here apparently contributions from chemical interactions are expected to dominate the atomic dynamics.

Zusammenfassung

Obwohl Diffusion eine funamentale Größe in der Physik und Materialwissenschaft ist, sind die Diffusionsmechanismen in Flüssigkeiten noch nicht hinreichend verstanden. Beispielsweise ist unklar, wie strukturelle Eigenschaften wie die Atompackung sowie die topologische und chemische Nahordnung die atomare Dynamik in Metallschmelzen beeinflussen.

In dieser Arbeit wird die Struktur-Dynamik-Beziehung in Metallschmelzen, welche durch tiegelfreie Levitationsverfahren prozessiert wurden, untersucht. Quasielastische Neutronenstreuexperimente (QENS), die am Flugzeitspektrometer TOFTOF des Heinz Maier-Leibnitz Zentrum (MLZ) durchgeführt wurden, geben dabei Rückschluss auf die atomaren Transportprozesse. Zusätzliche wurde die Struktur mittels Beugung von Neutronen und Synchrotron-Röntgenstrahlen untersucht.

QENS-Messungen von Quecksilber zeigen, dass der Diffusionskoeffizent reiner Metalle am Schmelzpunkt mittels der Atommasse und Packungsdichte vorhergesagt werden kann, wenn eine ähnliche Dynamik wie in Alkalimetallen angenommen wird. Der semi-empirische Ansatz, welcher auf unkorrelierten binären Stöße beruht, ist jedoch bei der Vorhersage der Temperaturabhängigkeit der Diffusion durch die Aktivierungsenergie ungenau.

Zusammensetzungen des binären Zr-Ti Systems haben ein ähnliches Packungsverhalten wie Quecksilber. In Zr-reichen Mischungen verringert sich die mittels QENS bestimmte Ti-Mobilität mit zunehmenden Ti-Gehalt. Durch Strukturmessungen lässt sich zeigen, dass in Zr-Ti Schmelzen kaum chemische Nahordnung vorhanden ist. Die konzentrationsäbhängige Dynamik kann durch Vorhersagen der Modenkopplungstheorie (MCT) von binären Hartkugeln erklärt werden und auf die unterschiedlichen Atomradien des Systems zurückgeführt werden. Dies weist auf einen vorherrschenden Einfluss der topologischen Struktur auf die Atombewegung hin.

Zr-Cu(-Al/Ti) Schmelzen besitzen höhere Packungsdichten als Quecksilber und Zr-Ti, was mit einer verringerten Dynamik einhergeht. Zudem führen geringfügige Zugaben von nur 4 at.% Al oder Ti fast zu einer Halbierung des Selbstdiffusion in $Zr_{50}Cu_{50}$-Schmelzen. Eine ähnliche Verlangsamung der Dynamik kann bei geringfügiger Al-Zugabe auch in der Viskosität der Schmelze beobachtet werden. Trotz unterschiedlicher Dynamiken, sind sowohl die statische Struktur als auch die makroskopische Packungsdichte von $Zr_{50}Cu_{50}$- und $(Zr_{50}Cu_{50})_{96}(Ti, Al)_4$-Schmelzen nahezu identisch. Während für Hg und Zr-Ti die Dynamik durch topologische Effekte bestimmt wurde, sind hier dominante Beiträge von chemischer Wechselwirkungen zu erwarten.

Contents

1 Introduction **1**

2 Theoretical Background **7**

2.1 Diffusion mechanism in condensed matter . . . 8
2.2 Introduction to neutron scattering . . . 12
  2.2.1 Neutron source . . . 12
  2.2.2 Scattering cross-section . . . 13
  2.2.3 Elastic and inelastic scattering . . . 15
  2.2.4 Coherent and incoherent scattering . . . 16
  2.2.5 Correlation function . . . 17
  2.2.6 Scattering from diffusive processes . . . 19
  2.2.7 Structural analysis of binary alloys . . . 21
2.3 Short-range order in metallic melts . . . 23
2.4 Packing fraction . . . 25
2.5 Mode-coupling theory . . . 26
2.6 Viscosity . . . 28
2.7 Stokes-Einstein relation . . . 29

3 Experimental methods and instruments **31**

3.1 Levitation . . . 32
  3.1.1 Electrostatic levitation (ESL) . . . 32
  3.1.2 Electromagnetic levitation (EML) . . . 35
  3.1.3 Temperature measurement . . . 38
3.2 Scattering experiments . . . 39
  3.2.1 Quasielastic neutron scatting (QENS) . . . 39
  3.2.2 Neutron diffraction . . . 45
  3.2.3 X-ray diffraction . . . 47
3.3 Density measurements . . . 49
3.4 Viscosity measurements . . . 50

3.5 Sample preparation 52

4 Results 53
4.1 Self-diffusion in Mercury investigated with quasielastic neutron scattering . 54
4.1.1 Experimental 55
4.1.2 Sample holder 56
4.1.3 Data reduction 58
4.1.4 Results of QENS 60
4.1.5 Semi-empirical diffusion theory of binary collisions 62
4.1.6 Relation between self-diffusion and viscosity 65
4.1.7 Conclusion 69
4.2 Short-range order in binary Zr-Ti melts 70
4.2.1 Neutron diffraction of zero scattering composition 73
4.2.2 X-ray diffraction using synchrotron radiation 75
4.2.3 Density measurement and calculation of the molar volume 78
4.2.4 Concentration-dependent atomic dynamics as seen by quasielastic neutron scattering 81
4.2.5 Calculated motion by mode-coupling theory using hard spheres . . 86
4.2.6 Conclusion 89
4.3 Structure and dynamics in bulk metallic glass forming liquids with minor additions 90
4.3.1 Structural investigation and packing fraction 92
4.3.2 Viscosity 94
4.3.3 Atomic dynamics as studied by quasielastic neutron scattering . . . 96
4.3.4 Phase selection during solidification 98
4.3.5 Conclusion 104

5 Conclusion and Outlook 105
5.1 Conclusion 105
5.2 Outlook 107

Appendices 111
A Diffusion coefficients 112
A.1 Diffusion coefficients from section 4.1 112
A.2 Diffusion coefficients from section 4.2 113
A.3 Diffusion coefficients from section 4.3 114
B Viscosity Data 115

Bibliography **119**

List of Figures **151**

List of Tables **153**

Copyright permissions **155**

Acknowledgments **157**

Abbreviations

BMG	Bulk metallic glass
DFG	German Research Foundation
DLR	German Aerospace Center
DLR-MP	Institute of Materials Physics in Space at DLR
D20	High intensity 2-axis diffractometer at the ILL
EDX	Energy dispersive X-ray spectroscopy
EML	Electromagnetic levitation
ESL	Electrostatic levitation
ESRF	European Synchrotron Radiation Facility, Grenoble
FRIDA	Fast reliable interactive data analysis
HWHM	Half-width at half-maximum
ID11	Materials science beamline at the ESRF
ILL	Institut Laue-Langevin, Grenoble
MCT	Mode-coupling theory
MLZ	Heinz Maier-Leibnitz Zentrum, Garching
QENS	Quasielastic neutron scattering
SEM	Scanning electron microscope
TOFTOF	Cold neutron time-of-flight spectrometer at MLZ
TUM	Technische Universität München

α_V	Volume expansion coefficient
$A(Q)$	Quasielastic intensity
b	Scattering length
bcc	Body-centered cubic
$bg(Q)$	Background function
D	Diffusion coefficient
D_0	Diffusion coefficient at infinite temperature
η	Viscosity
E	Energy
E_A	Activation energy
F	Force
fcc	Face-centered cubic
$\Gamma(Q)$	Half-width at half-maximum
$G(r,t)$	Van Hove correlation function
$\hbar$	Planck constant
hcp	hexagonal closest packed
$I(Q,t)$	Intermediate scattering function
k_B	Boltzmann constant
k	Wave number
λ	Wave length
$L(Q,\omega)$	Lorentzian function
m	Mass
M	Molar mass
n	Number density

N_A	Avogadro constant
ω	Wave frequency
ϕ	Packing fraction
Q	Momentum transfer
ρ	Density
r	Radius
$R(Q, \omega)$	Instrumental resolution function
σ	Scattering cross-section
$S(Q)$	Structure factor
S_{CC},S_{NN},S_{NC}	Partial structure factors
$S(Q, \omega)$	Dynamic structure factor
τ	Relaxation time
t	Time
T	Temperature
θ	Scattering angle
V	Volume
V_m	Molar volume
$W(t)$	Mean-squared displacement
Z	Atomic number

1 Introduction

Diffusion describes the transport of mass via (random) walks. In condensed matter this process is strongly influenced by the short-range order, which can be differentiated into the topological arrangement of the atoms within the range of a few coordination shells around a given atom (topological short-range order) and their chemical arrangement (chemical short-range order).

In case of liquids the first theoretical consideration on diffusive motion was given by Albert Einstein in his PhD thesis in 1905 [1]. Einstein described the mobility of glucose molecules in solution by the internal friction of the solution. He connected the microscopic diffusion coefficient obtained by Thomas Graham [2] with macroscopic viscosity data [3] and was able to calculate the glucose molecule dimensions based on a hard-sphere model. In doing so, Einstein obtained a - more or less - exact value of the Avogadro number [4]. It was the very first explanation of the Brownian motion [5, 6] and a proof of the (at that time controversial) existence of atoms.

Diffusion is a fundamental property in physics and materials science [7]. Examples are chemical reactions in liquid [8] and solid states [9, 10], solidification [11, 12] and crystal growth from melts [13, 14], or permeation trough membranes [15]. However, it is also relevant to many other fields [16, 17]. For example, it can be used to describe the motion of oceans and atmospheres to forecast the daily weather [18, 19] or to explain the dynamics of population, e.g. how languages disperse [20, 21]. Furthermore, the mobility of human travel can be explained by diffusive dynamics [22, 23] e.g. to forecast and control the spreading of infectious diseases [24, 25], which are at the time this thesis is written (the COVID-19 pandemic [26]) a topic of daily discourse.

In crystalline solids the diffusion mechanism is governed by to the periodic crystal structure. Here, atoms diffuse e.g.: via either interstitial, interstitialcy or vacancy mechanisms [7, 27–32].

Due to the disordered nature of the liquid structure such mechanisms are inapplicable in liquids, where the diffusion mechanism is more complicated. For example, Einstein assumed in his consideration the short-range order of the dissolved molecules to be homogeneous and completely structureless. In addition, describing molecules by hard-spheres neglects the internal degrees of freedom and the bonding characteristics. In contrast, metallic liquids are composed of single atoms without any internal degrees of freedom. The repulsive nature of metallic bonds at short distances are making them a closer analogy of hard-spheres and therefore an ideal candidate to investigate diffusion in the liquid.

Since decades, a lot of research efforts have been put in measuring and understanding the diffusion in metallic melts [33–38]. Classically, diffusion coefficients in metallic liquids are measured in long capillaries, where thin cylindrical sample couples are molten under inert atmosphere and annealed at a certain temperature [34, 39–43]. After cooling, one can then determine ex-situ the diffusion coefficients by analyzing the diffusion profile. However, this method comes with some disadvantages, which sum up in deviations of up to 100 % [44]. These are mainly:

1. The volume change of the sample as a function of temperature, also through a phase transition, and, therefore, the diffusion length is different in the melted and the solid phase due to thermal expansion. Known thermal expansion coefficients are subject to error.

2. As it is an ex-situ method, the melting and solidification process of the material give certain inaccuracy to the diffusion profile due to sedimentation and concentration change during phase transition. In case of non-congruent melting materials the diffusion profile can be destroyed during solidification.

3. Already existing density or temperature gradients (Buoyancy and Marangoni convetion) in the melt can create convection within the sample and also affect the result.

Another method to determine diffusion coefficients is quasielastic neutron scattering (QENS), which allows an in-situ observation of atomic transport processes [45]. Due to their wavelength, which is comparable to typical interatomic spacings of 1-2 Å and energies similar to excitation energies in condensed matter, neutrons enable a detailed microscopic probing of the liquid-state structure and dynamics [46–48]. Structural information is obtained by those neutrons, which are elastically scattered by the nuclei of the sample components. In addition to this, an energy transfer occurs in case of atomic movement within the sample. This is known as inelastic scattering, through which neutrons lose or gain energy as a result of their interaction with the sample and, therefore, change their velocity / wavelength. In case of self-diffusion in liquids, this energy transfer is rather small, in the order of some tens to hundreds of µeV [49]. Since QENS probes atomic motion directly on a pico-to-nano-second time scale, which is not affected by any convective flow, this allows a rather accurate determination of the self-diffusion coefficient on an absolute scale, nevertheless this technique is limited to incoherent scatterers [50].

Using quasielastic neutron scattering accurate studies of atomic diffusion in pure elements like the alkali metals [51], Al [52, 53], Cu [54], Fe [55], Ge [56] and Ni [57] were carried out.

In case of Nickel the self-diffusivity was not only investigated for the pure element, but also for Ni-P, Pd-Ni-P and Pd-Ni-Cu-P alloys [58], where the mixing has a drastic effect on the liquidus temperature of the respective alloys. Therefore, the atomic dynamics could be studies in a broad temperature range of almost 1.000 K. A decreased Nickel mobility towards lower temperatures was found, which is suggested to be related to the packing fraction of atoms [58].

Also in binary Zr-Cu melts a slower self-diffusion of Cu in Cu-rich concentrations is accompanied with an increased packing fraction [59]. Similar observations were made in case of Al-Ni melts. Here, the overall Nickel self-diffusion remains unchanged in different Ni-rich binary alloys, where also the atomic volume is similar. The diffusivity is correlated to the density of packing over the entire composition range [60]. In case of the Al-rich concentration a denser packing causes slower diffusion, which could be explained by an increased chemical interactions between the constituents in this alloys [61].

Pronounced chemical short-range order explains also slower atomic dynamics in Zr-Co and Zr-Ni melts when Aluminum is added [62]. However, the packing fraction is contrarily decreased in ternary Zr-(Co,Ni)-Al alloys when compared to the binary Zr-Co and Zr-Ni mixtures.

In case of Zr-Ni and Hf-Ni melts, where Zr is substituted by Hf, the packing fraction is also not suitable to explain changes in the melt dynamics [63]. Here, directly measured partial structure factors reveal that structural changes at the atomic scale influence atomic diffusion [64].

Hence, for some binary systems a slower diffusion could be correlated to a higher packing fraction, whereas for other systems no correlation was found. Here, increased chemical interactions were found to explain the slower dynamics. This raises the question how packing fraction and chemical short-range order influence the atomic dynamics in metallic melts.

The diffusion mechanism in liquids can best be studied for single component metallic melts. Subject of the first result section of this work is the investigation of the self-diffusion of Mercury, which exhibits the lowest melting point ($T_m = 234.3$ K) of all metallic elements and hence small kinetic energy of the atoms in the melt. A number of models describing the mass transport in metallic liquids end up in semi-empirical terms with thermodynamic parameters [33–38]. Comparing Mercury to the other single component liquid metals reveals if the diffusion coefficient and the activation energy of atomic motion can be related. Additionally, the large density of 13.5 g/cm^3 of Mercury leads to the question how the diffusion in liquids depends on the atomic mass, the atomic radii and the atomic packing.

Next, the binary Zr-Ti system is investigated. Zirconium and Titanium are both Group 4 elements and show very similar chemical and structural properties [65, 66]. However, both elements exhibit slightly different atomic radii [67], which leads to the question, how the structure and dynamics depend on the composition. Therefore, the melt properties are comprehensively studied. Neutrons and x-rays from sychrotron radiation are used to investigate the liquid structure. From density measurements the molar volume, volume expansion, excess volume and packing fraction are derived, which can be related to the structure on the atomic scale and the melt dynamics as investigated using QENS. A link of structure and dynamics is given by theoretical considerations, e.g. the mode-coupling theory [68], which is used to predict diffusion coefficients.

Since Zr-Ti melts are chemically very reactive containerless electromagnetic levitation (EML) is used to process the melts in order to avoid reactions with the crucible materials [69]. In combination with neutron and x-ray scattering this leads also to an excellent signal-to-noise ratio [70–73].

If even minor composition changes can affect the melt dynamics, is discussed in the third result section of this work. For example, in bulk metallic glass forming liquids, where cooling the melt under a critical temperature leads to a suppression of crystallization while forming an amorphous structure, minor additions can have a huge influence on properties like e.g. the glass-forming ability [74–78]. One example is the Zr-Cu system, where minor Al and Ti additions cause a rather large improvement of the glass-forming ability [77, 79]. This work investigates, if the melt dynamics can be sensitive to minor composition changes, which is in contrast to an average packing fraction description.

Therefore, $(Zr_{50}Cu_{50})_{96}(Ti, Al)_4$ melts are processed in electrostatic levitation (ESL) in combination with experiments using neutron and x-ray scattering [80, 81]. Complementary, macroscopic melt properties like the viscosity and density can be studied with high accuracy [82–85].

2 Theoretical Background

Objective of this chapter is to present all the necessary basic information and principles for the following experiments. These mainly deal with theoretical concepts of diffusion, the structure of metallic melts and how those quantities can be investigated using neutron scattering.

2.1 Diffusion mechanism in condensed matter

Diffusion comes from the Latin verb “diffundere”, which means “spreading out” and describes particle displacement in matter by internal and external driving forces. In 1855 the physician Adolf Fick first described diffusion mathematically by concentration gradients on water-permeable membranes [86]. For systems in thermodynamic equilibrium, where all external factors are constant per definition, there are no concentration gradients. On a macroscopic scale this means a homogeneous particle distribution.

The microscopic motion then is only driven by internal kinetic energy, as reflected by the temperature [87]. Random motion was already described in 1827 by Robert Brown and is also known as Brownian motion or “pedesis” (ancient greek for “leaping”) [5]. This broad theory, however, got a physical crosslink in 1905 by Albert Einstein via the diffusion coefficient [6]. It describes the thermally driven random transport of matter and is a temperature and pressure dependent material parameter.

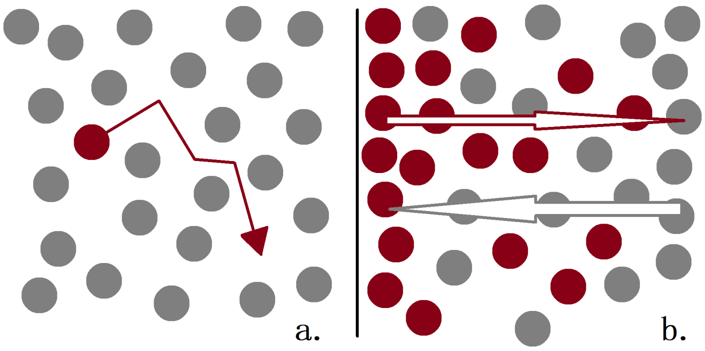

Figure 2.1: The two main types of diffusion processes, where (a.) refers to self-diffusion and (b.) to inter-diffusion at the interface between two substances

Generally speaking, diffusion describes the long-range transport of particles within matter (i.e. gases, liquids and solids) by thermal motion. It plays an important role in various fields of nature, technology and society [16, 17]. Relevant literature can be found in in [88–91].

Two main types of diffusion can be distinguished, which are sketched in Fig. 2.1. In the case of no chemical concentration gradients, self-diffusion (Fig. 2.1.a.) represents the long-range transport of a single particle in a uniform system via thermal motion and concomitantly density fluctuations.

Inter-diffusion (Fig. 2.1.b.) describes collective mass transport due to the presence of a chemical potential gradient in multi-component systems. Conventionally, inter-diffusion is depicted as occurring from regions of high concentrations to regions of lower concentrations along a concentration gradient, as implied by the arrows in Fig. 2.1.b.. However, diffusion can also happen in same direction as the concentration gradients, e.g. in case of thermodynamic forces, which lower the total free energy in the systems. This can happen for example during spinodal decomposition or on defects, impurities and during nucleation. It is so-called "uphill" diffusion.

In crystalline materials, atoms form a long-range ordered arrangement. Within this structure, single atoms are surrounded by nearest neighbors on well-defined lattice sites and localized around an equilibrium position. Diffusion can occur, for example, via the hopping of single atoms through vacancies within the lattice, on interstitial lattice sites or highly correlated motion of several atoms at the same instant. In gaseous materials, whose dynamics can be described by ideal gas theory, particle displacement is generally free and continues uninterrupted until collision.

However, in liquids, the diffusion mechanism is situated somewhere between that of crystals and gases. In liquids, atoms are surrounded at short times by a highly dynamic "cage" with a cage-escape frequency dominated by random collisions (see 2.5). In the limit of long time and length scales, this results in translational diffusion described by Brownian motion.

Mathematically, random walk diffusion can be described by the mean-squared displacement $W(t)$ with the equation

$$W(t) \equiv < |r(t) - r_0|^2 >, \tag{2.1}$$

where $r(t)$ is the position of an atom at time t, r_0 is the position of the center of mass at $t = 0$, and the brackets $< \dots >$ denote an ensemble averaging.

In isotropic media, diffusion occurs randomly in all directions with equal probability. As such, the single average particle displacement $< \delta r(t) >$ tends towards zero in the long-time limit and is therefore not a suitable metric.

According to Albert Einstein's relation, the diffusion constant is defined by the thermal motion of atoms

$$D = \mu k_B T, \tag{2.2}$$

where μ is the atomic mobility, k_B the Boltzmann constant and T the temperature. This equation can also be expressed by the (one dimensional) attempt frequency ν and diffusion length l.

$$D = \frac{1}{2} l^2 \nu. \tag{2.3}$$

Due to the absence of external forces, the mean squared displacement is only due to thermal motions and can be expressed by

$$W_s(t) = 2Dt. \tag{2.4}$$

Diffusional mass transport also result from gradients in concentration. A mathematical depiction is given by Adolf Fick's laws. The first law describes the particle flux $\vec{J}$ in relation to a concentration gradient δc/δx. Because uphill diffusion occurs seldom diffusion is usually considered to run against the concentration gradient. The particle flux is conventionally expressed with a minus sign as follows:

$$\vec{J} = -D \frac{\delta}{\delta x} c = -D \nabla c. \tag{2.5}$$

Since mass is neither created nor destroyed during motion, it is considered as conserved and Fick's second law can be obtained employing the continuity equation

$$\frac{\delta c}{\delta t} = -\frac{\delta \vec{J}}{\delta x}, \tag{2.6}$$

which yields the space and time dependence of the concentration profile

$$\frac{\delta c}{\delta t} = \frac{\delta}{\delta x} \left(D \frac{\delta}{\delta x} c \right) \equiv \nabla \left(D \nabla c \right). \tag{2.7}$$

In case of self-diffusion, microscopic concentrations are expressed as atoms per unit volume, which can be described by the probability density function $P(r,t)$. Assuming isotropic motion, Fick's second law can be rewritten as

$$\frac{\delta}{\delta t} P\left(\vec{r}, t\right) = D \left[\frac{\delta^2}{\delta x^2} + \frac{\delta^2}{\delta y^2} + \frac{\delta^2}{\delta z^2} \right] P\left(\vec{r}, t\right) \equiv D \nabla^2 P\left(\vec{r}, t\right), \tag{2.8}$$

for a diffusion in direction $\vec{r} = \vec{r}(x, y, z)$. The three dimensional mean-squared displacement can be expressed by adding two dimensions to the already described one dimensional Einstein relation:

$$W_s(t) = 6Dt. \tag{2.9}$$

Using the correlation of the mean-squared displacement and the probability density function

$$W_s(t) = \int \mathrm{d}\vec{r}\; r^2 P(\vec{r}, t), \tag{2.10}$$

the probability density function is expressed

$$P(\vec{r}, t) = \frac{1}{[4\pi Dt]^{\frac{3}{2}}} / \exp\left(-\frac{r^2}{4Dt}\right), \tag{2.11}$$

which is a Gaussian function with a width increasing in time.

2.2 Introduction to neutron scattering

The 1994 Nobel laureates in physics (for pioneering contributions to the development of neutron scattering techniques for studies of condensed matter) Clifford Shull and Bertram Brockhouse are quoted with the phrase “neutrons tell us where atoms are and how they move” [92]. Neutrons interact as uncharged particles with nuclei in condensed matter and are very sensitive to light elements, in contrast to x-rays and electrons, which interact with the electron cloud. Relevant literature of the scattering theory can be found in [46–48].

2.2.1 Neutron source

The objective of a neutron source is to produce a high flux of free neutrons, which have an average lifetime of 879.4 ± 0.6 seconds [93, 94]. There are many processes that can produce free neutrons as final products, including nuclear reactions (indeed, this was the first reported production of free neutrons as a released product after bombarding beryllium nuclei with α-particles [95]), decay of radioisotopes [96] or through manipulation of plasma [97], electric fields [98] or photofission [99]. Currently, there are two commonly used techniques to specifically achieve a high neutron flux: fission and spallation.

Nuclear fission was discovered by Meitner and Hahn [100, 101]. High performance fission neutron research sources such as the High Flux Isotope Reactor (HFIR) in Oak Ridge, the Institut Laue-Langevin (ILL) in Grenoble and the Heinz Maier-Leibnitz Zentrum (MLZ) in Munich all use the uranium isotope ^{235}U, which produces, by absorbing slow neutrons, 2 or 3 free neutrons (on average 2.4) and emits an average energy of about 192.9 MeV [102].

$$^{235}U + neutron \rightarrow fission\ fragments + 2.4\ neutrons + 192.9\ MeV \tag{2.12}$$

This reaction runs typically within ps-ns and the produced neutrons can cause by their own the fission of another 2 or 3 nuclei to initiate thereby a chain reaction. In order to increase the reaction probability the neutrons have to be decelerated, which is likely done by collisions with energy absorbing light elements, such as in heavy water D_2O. Typical fission fragments are ^{93}Kr or ^{141}Ba, which can also emit “delayed” neutrons after some seconds, which are, however, very important to control the chain reaction, even though they mark only about 0.64 % of the total amount of produced neutrons. By allowing some of the moderated neutrons to escape or by use of proper neutron absorbers, a constant neutron flux can be adjusted.

Spallation is another method of generating a high neutron flux [103]. Here, high-energy protons are accelerated to an energy up to 1 GeV and hit targets made from heavy elements like lead, mercury, uranium or tungsten, which excites the nuclei to "evaporate" up to 20 high-energy neutrons. As this process is directly linked to the incoming particles, spallation generates not a continuous flux of neutrons, but rather a pulsed neutron beam. This principle is used e.g. at ISIS in UK, SNS in USA, J-SNS in Japan and will be implemented in the European Spallation Source (ESS), which is currently under construction in Lund, Sweden. Even though spallation might produce an order of magnitude higher flux in the pulse the fine average flux remains in the same order as for high performance continuous sources. This is due to the limits of the necessary heat dissipation during one pulse. Lastly, laser-induced fusion has been announced as an alternative neutron source and is recently under research to reach applicability [104–106].

2.2.2 Scattering cross-section

For a neutron scattering experiment an incident neutron beam of well defined wavelength hits a sample consisting of neutron scatterers. The beam is scattered in different directions in space. By analyzing the scattered intensity as a function of the scattering angle and/or the energy of the scattered neutrons, diverse measurements can be performed, which are expressed in terms of a quantity called the double differential scattering cross-section. This is the physical quantity measured by a scattering experiment and is related to the detected intensity.

Considering the Fraunhofer approximation (neutron detector is located at a distance larger compared to the dimensions of the scattering system and detector itself [107]), the number n' of scattered neutrons per unit time in a given direction $d\Omega$ (in terms of θ and ϕ as defined in Fig. 2.2) can be counted as a function of energy at the scattered neutrons in an interval between E' and $E' + dE'$. The double differential cross-section is defined by

$$\frac{d^2\sigma}{d\Omega dE'} = \frac{n'}{j d\Omega dE'}, \tag{2.13}$$

where j refers to the incident neutron flux (number of neutrons per unit area and second).

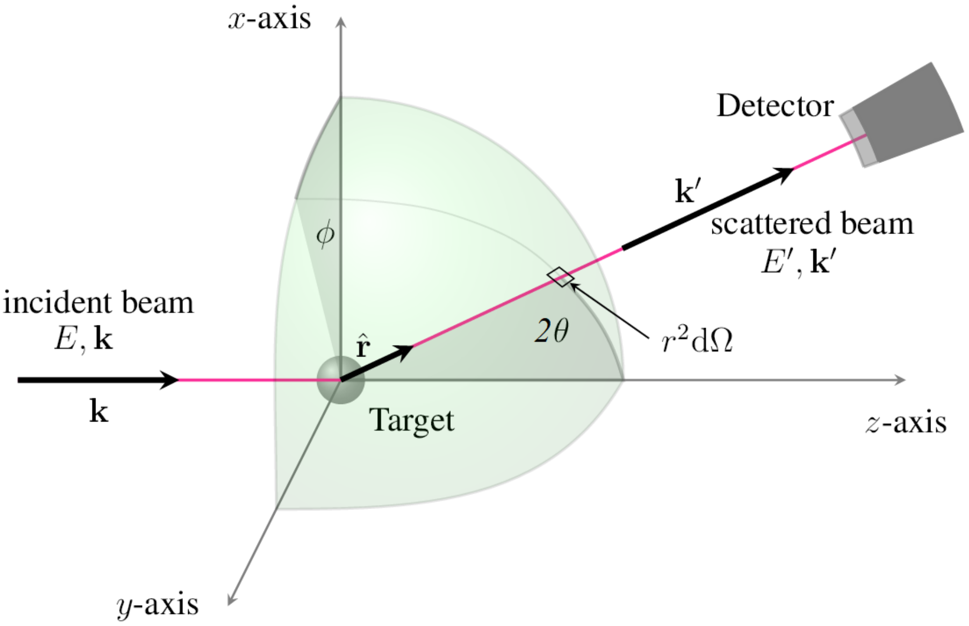

Figure 2.2: The general geometry of an experiment, where an incident beam is scattered by a sample. E indicates the energy and $\vec{k}$ the wave vector [108]

If information about possible energy changes by the scattering process is not relevant or detectable, then the angular dependence is described by the differential cross-section

$$\frac{d\sigma}{d\Omega} = \frac{n'}{jd\Omega} = \int_0^\infty \frac{d^2\sigma}{d\Omega dE'} \mathrm{d}E'. \tag{2.14}$$

Finally, the scattering cross-section, which, as the name implies, has the dimensions of an area, gives a measure of the total number of scattered neutrons in all directions

$$\sigma = \int_{all\ directions} \frac{\delta\sigma}{\delta\Omega} \mathrm{d}\Omega. \tag{2.15}$$

For a fixed target in the origin of the illustration in Fig. 2.2, the wave function of the incident neutrons, which travel in the direction of $\vec{k}$, can be represented by a plane wave

$$\Psi_{incident} = \exp(i\vec{k}z). \tag{2.16}$$

Since the range of nuclear forces (in fm) that cause scattering is much smaller than the wavelength of the incident neutrons (in Å), in case of nuclear scattering the scattered neutron wave can be considered as spherical

$$\Psi_{scattered} = \frac{-b}{r} \exp(i\vec{k}\vec{r}), \tag{2.17}$$

where b is the direction-independent scattering length (in fm), which depends on the type of the scattered nucleus and its spin state. The scattering cross-section can be expressed by

$$\sigma = 4\pi b^2. \tag{2.18}$$

The cross-sectional unit is typically expressed in barn, which is defined as 10^{-28} m^2.

2.2.3 Elastic and inelastic scattering

Referring back to Fig. 2.2, a scattering vector $\vec{Q}$ can be defined as

$$\vec{Q} = \vec{k} - \vec{k}'. \tag{2.19}$$

In case of elastic scattering, the incident and scattered wave vector have the same length ($|\vec{k}| = |\vec{k}'|$), as no energy transfer occurs ($\Delta E = 0$). The kinetic energy of neutrons is quantified with the reduced Planck constant $\hbar$ and neutron mass m_n by

$$E = \frac{\hbar^2 k^2}{2m_n}, \tag{2.20}$$

using

$$k = \frac{2\pi}{\lambda}. \tag{2.21}$$

According to de Broglie [109], the magnitude of the scattering vector under elastic scattering conditions is then equal to the Bragg condition [110]

$$Q_{elastic} = \frac{4\pi}{\lambda} \sin(\theta). \tag{2.22}$$

Inelastic scattering is accompanied by energy exchange, e.g. due to atomic motion, i.e. $\Delta E = E_f - E_i$, where E_f and E_i are the final and incident neutron energies, respectively. According to the Planck-Einstein relation [111], ΔE can be described as a wave frequency ω as

$$\Delta E = \hbar\omega. \tag{2.23}$$

The relation between momentum transfer and inelastic scattering is then described by

$$Q_{inelastic} = \left(\frac{1}{2m\hbar^2} \left\{ 2E_i + \hbar\omega - 2\left[E_i\left(E_i + \hbar\omega\right)\right]^{\frac{1}{2}} \cos(\theta) \right\} \right)^{\frac{1}{2}}. \tag{2.24}$$

2.2.4 Coherent and incoherent scattering

Coherent scattering occurs when there is a phase relationship between the scattered neutrons. This is measured when the empirical scattering length b from equation 2.18 is equal between nuclei in the scattering system. In practice, the scattering length has some random variability due to the presence of different isotopes or nuclear spin states (or both!). So, for a certain part of the scattered wave amplitudes there is no phase relationship between the scattered neutron waves. The intensity of that is called incoherent. Usually, in a neutron scattering experiment the sum of coherent and incoherent scattering contribution is measured.

If the scattering system consists of a large number of nuclei, the measured double differential cross-section according to equation 2.13 can be expressed by the distribution average

$$\left(\frac{d^2\sigma}{d\Omega dE'}\right)_{coh} = \frac{\sigma_{coh}}{4\pi}\frac{k'}{k}\frac{1}{2\pi\hbar}\sum_{jj'}\int_{-\infty}^{\infty}\left\{\exp\left(-i\vec{Q}\vec{R}_{j'}(0)\right)\exp\left(-i\vec{Q}\vec{R}_{j}(t)\right)\right\}\exp\left(-i\omega t\right)\mathrm{d}t \tag{2.25}$$

$$\left(\frac{d^2\sigma}{d\Omega dE'}\right)_{inc} = \frac{\sigma_{inc}}{4\pi}\frac{k'}{k}\frac{1}{2\pi\hbar}\sum_{j}\int_{-\infty}^{\infty}\left\{\exp\left(-i\vec{Q}\vec{R}_{j}(0)\right)\exp\left(-i\vec{Q}\vec{R}_{j}(t)\right)\right\}\exp\left(-i\omega t\right)\mathrm{d}t, \tag{2.26}$$

where $\vec{R}_j$ is the position of the j_{th} scattering nuclei (with $j = 1, ..., n$) with respect to the origin [48].

Here the scattering cross-section from equation 2.18 is separated as follows:

$$\sigma_{coh} = 4\pi\overline{b}^2 \tag{2.27}$$

$$\sigma_{inc} = 4\pi(\overline{b^2} - \overline{b}^2) \tag{2.28}$$

The mean scattering area (squared scattering length) is defined with the relative frequency p_j as

$$\overline{b_j b_{j'}} = \overline{b}^2 = \left(\sum_j p_j b_j\right)^2 \tag{2.29}$$

$$\overline{b_j b_j} = \overline{b^2} = \sum_j p_j {b_j}^2. \tag{2.30}$$

Coherent scattering gives information about inter-atomic correlations, which correspond to static structural information in the elastic case and to information about collective motion (e.g. phonons, magnons) in the inelastic case.

Incoherent scattering gives information about the self-correlation. In the elastic case, this relates atomic positions (which appear in a scattering experiment except for the Debye-Waller factor as a flat background in the Q-space) and, in the inelastic this is described by single atom motion (e.g. diffusive motion and atomic or molecular vibrations).

Beside scattering, there is a certain, isotope-specific possibility that incident neutrons perform nuclear reactions, i.e. are considered as absorbed. This is described by the absorption cross-section σ_{abs}, which is proportional to the neutron wavelength λ. Elements with a comparatively high absorption cross-sections are e.g. Boron ($\sigma_{abs}(B) = 767$ barn), Cadmium ($\sigma_{abs}(Cd) = 2520$ barn), Gadolinium ($\sigma_{abs}(Gd) = 49700$ barn), Helium-3 ($\sigma_{abs}(^3He) = 5333$ barn) and Mercury ($\sigma_{abs}(Hg) = 372.3$ barn) (all at a neutron wave length of $\lambda = 1.798$ Å [112]) can be used as neutron absorbers for shielding applications or the detection of thermal neutrons.

The total cross-section quantifies the sum of coherent scattering, incoherent scattering and neutron absorption during the scattering process.

$$\sigma_{tot} = \sigma_{coh} + \sigma_{inc} + \sigma_{abs} \tag{2.31}$$

The respective characteristic parameters can be measured [112].

2.2.5 Correlation function

Correlation functions allow a description of nuclei motion by relating the spatial time dependent distances to the respective parts in the cross-section. The measured total double differential cross-section is thus made up of equation 2.25 and equation 2.26 and can be written together as

$$\frac{d^2\sigma}{d\Omega dE'} = \frac{N}{4\pi}\frac{k'}{k}\left(\sigma_{coh}S_{coh}\left(\vec{Q},\omega\right) + \sigma_{inc}S_{inc}\left(\vec{Q},\omega\right)\right), \tag{2.32}$$

where $S(\vec{Q},\omega)$ is the scattering function (also called dynamic structure factor). Here, N is the number of particles in the system.

$$S_{coh}\left(\vec{Q},\omega\right) = \frac{1}{2\pi N\hbar}\sum_{jj'}\int_{-\infty}^{\infty}\left\{\exp\left(-i\vec{Q}\vec{R}_{j'}(0)\right)\exp\left(-i\vec{Q}\vec{R}_j(t)\right)\right\}\exp\left(-i\omega t\right)\mathrm{d}t \tag{2.33}$$

$$S_{inc}\left(\vec{Q},\omega\right) = \frac{1}{2\pi N\hbar}\sum_{j}\int_{-\infty}^{\infty}\left\{\exp\left(-i\vec{Q}\vec{R}_{j}(0)\right)\exp\left(-i\vec{Q}\vec{R}_j(t)\right)\right\}\exp\left(-i\omega t\right)\mathrm{d}t \tag{2.34}$$

$S(\vec{Q},\omega)$ can be expressed as the temporal Fourier transform of the dimensionless intermediate scattering function $I(\vec{Q},t)$.

$$S_{coh/inc}\left(\vec{Q},\omega\right) = \frac{1}{2\pi\hbar}\int I_{coh/inc}\left(\vec{Q},t\right)\exp\left(-i\omega t\right)\mathrm{d}t \tag{2.35}$$

Similar to $S(\vec{Q},\omega)$, $I(\vec{Q},t)$ also exists in two versions, considering pairs of particles (coherent) or only one particle (incoherent). The incoherent part is also referred to as the self-intermediate scattering function.

$$I_{coh}\left(\vec{Q},t\right) = \frac{1}{N}\sum_{jj'}\left\{\exp\left(-i\vec{Q}\vec{R}_{j'}(0)\right)\exp\left(-i\vec{Q}\vec{R}_{j}(t)\right)\right\} \tag{2.36}$$

$$I_{inc}\left(\vec{Q},t\right) = \frac{1}{N}\sum_{j}\left\{\exp\left(-i\vec{Q}\vec{R}_{j}(0)\right)\exp\left(-i\vec{Q}\vec{R}_{j}(t)\right)\right\} \tag{2.37}$$

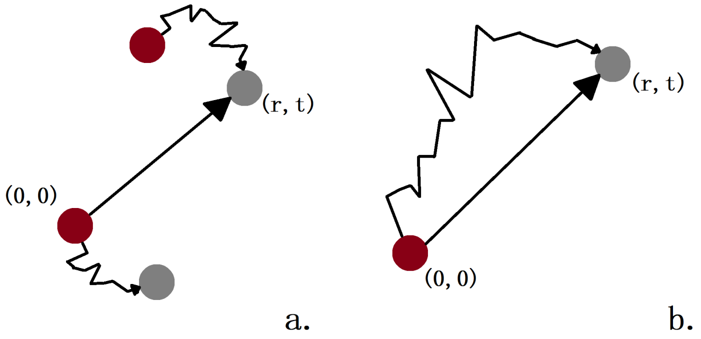

Figure 2.3: a. Pair correlation, where a particle j is at time t in position $\vec{r}$ and a particle j' has been in the origin $\vec{r}=0$ at time $t=0$; b. self correlation, where one and the same particle is at time t when it has been in the origin $\vec{r}=0$ at time $t=0$.

Furthermore, an additional Fourier back transform from reciprocal space to space yields the time-dependent Van Hove correlation function $G(\vec{r},t)$ [113] with dimension of an inverse volume. The coherent part of $G(\vec{r},t)$ relates to the pair correlation function $G_{pair}(\vec{r},t)$, which is the probability to find an atom j at time t at the place $\vec{r}$, if j or another atom j' was at time $t=0$ in the origin $\vec{r}=0$. This is sketched in Fig. 2.3.a.. The signal emanating from incoherent scattering relates to the self-correlation function $G_{self}(\vec{r},t)$, which gives the probability to find one atom at time t at place $\vec{r}$, if this atom was at time $t=0$ in the origin $\vec{r}=0$ (2.3.b.).

$$G_{pair}\left(\vec{r},t\right) = \frac{\hbar}{(2\pi)^3}\int\int S_{coh}\left(\vec{Q},\omega\right)\exp\left(-i\left(\vec{Q}\vec{r}-\omega t\right)\right)\mathrm{d}\vec{Q}\mathrm{d}\omega \tag{2.38}$$

$$G_{self}\left(\vec{r},t\right)=\frac{\hbar}{(2\pi)^3}\int\int S_{inc}\left(\vec{Q},\omega\right)\exp\left(-i\left(\vec{Q}\vec{r}-\omega t\right)\right)\mathrm{d}\vec{Q}\mathrm{d}\omega. \tag{2.39}$$

The van Hove correlation function $G(\vec{r},t)$ is therefore the inverse Fourier transform in time and space of the measured scattering function $S(\vec{Q},\omega)$. Thus, $S(Q,\omega)$ contains, in theory, all relevant physical information about the atomic positions and motions of the scattering system.

2.2.6 Scattering from diffusive processes

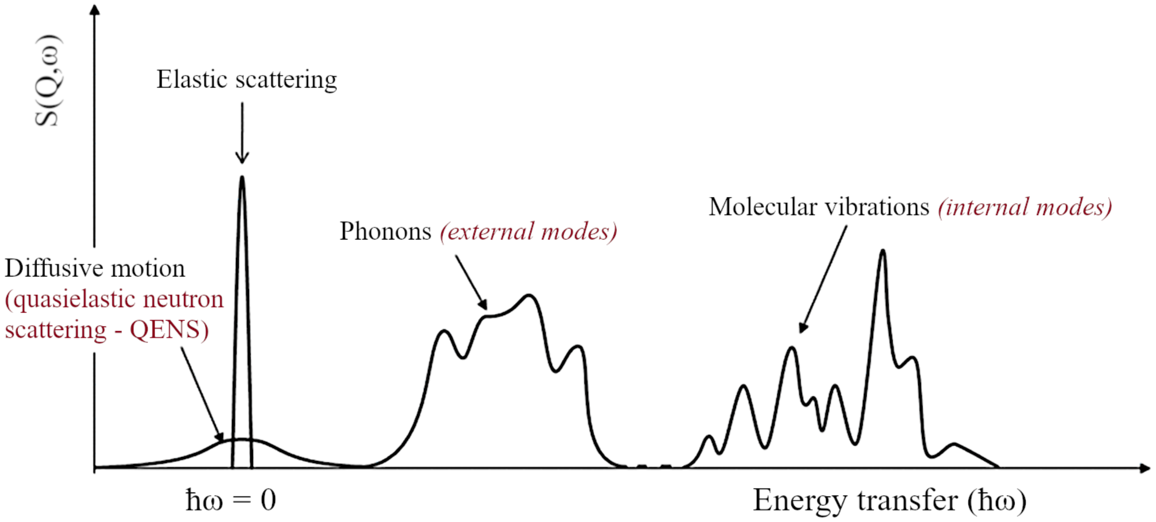

Figure 2.4: Schematic of different excitation modes and their resulting scattering contributions in the dynamic structure factor $S(Q,\omega)$ [114]

In Fig. 2.4 $S(Q,\omega)$ is depicted for different dynamical modes. The elastic line is located at zero energy transfer ($\omega=0$). In a neutron scattering experiment it is the delta function of the elastic scattering convoluted by the instrumental energy resolution. In the inelastic case, scattering is proportional to the density of states. Without going into the details; this refers on a 10^{-12} s to 10^{-13} s time scale to phonons and to molecular vibrations on a 10^{-14} s to 10^{-15} s time scale [115–117].

Quasielastic neutron scattering (QENS) refers to small energy transfers statistically distributed around zero energy transfer. Typically, QENS spectra show energy distributions from a few meV to infinite small energy. In the time domain this corresponds to 10^{-14} s and much lower times. Whereby the smallest energy and longest time is given by the energy / time resolution of the respective QENS instrument [45]. The QENS intensity consists of both coherent and incoherent scattering information.

In case of metallic melts in the hydrodynamic limit, i.e. in the limit of small wavenumbers Q and low frequencies ω the coherent inelastic scattering is described by a Lorentzian shaped line, emerging from thermal diffusivity due to temperature fluctuation and two Lorentzian shaped Brillouin lines, emerging from collective atom motion due to density fluctuations [118]. However, the Brillouin lines lie outside the relevant energy range of quasielastic neutron scattering. Moreover, the Rayleigh line appears in this energy range as a flat background [50].

For incoherent quasielastic scattering, the self-correlation function $G_{self}(\vec{r},t)$ is equal to the probability described in 2.1. In the following, only the case of an isotropic medium (e.g. liquids) is considered, where only the magnitude of the wave vector $\vec{Q}$ is necessary. Fick's second law according to equation 2.7 can then be rewritten

$$\frac{d}{dt}G_{self}\left(\vec{r},t\right) = D\nabla^2 G_{self}\left(\vec{r},t\right). \tag{2.40}$$

For diffusive motion, the probability density function according to equation 2.11 can be expressed as a solution of the differential equation 2.40, given the boundary condition of a delta function in the probability distribution for $\vec{r} = 0$, $t = 0$ in three dimensions by

$$G_{self}\left(\vec{r},t\right) = \frac{1}{\left[4\pi Dt\right]^{\frac{3}{2}}} \exp\left(-\frac{r^2}{4Dt}\right), \tag{2.41}$$

which gives a direct relation to the diffusive motion. Inserting equation 2.41 into equation 2.39 and equation 2.35 gives [118]

$$I_s\left(Q,t\right) = \exp\left(-Q^2 Dt\right) \tag{2.42}$$

$$S_{inc}\left(Q,\omega\right) = \frac{1}{\pi}\frac{DQ^2}{\omega^2 + \left(DQ^2\right)^2}. \tag{2.43}$$

Equation 2.43 has the form of a Lorentzian, with a half width at half maximum Γ of [119]

$$\Gamma(Q) = \hbar DQ^2. \tag{2.44}$$

Plotting the different Γ values divided by $\hbar$ as a function of Q^2 allows then a direct determination the self-diffusion coefficient by extracting the linear slope.

$I(Q,t)$ gives access to the structural relaxation of atoms in the time domain. At short times in the liquid (≤ 1 ps), fast atomic motion within transient cages formed by nearest-neighbors (see 2.1) result in a rapid decay of atomic correlations. At later times, escape from these cages eventually occurs with a relaxation time τ. For dense liquids, which can form glasses during rapid cooling, the shape of $I(Q,t)$ can be modeled using a phenomenological stretched exponential decay described by the Kohlrausch-Williams-Watts function [120].

$$I_s\left(Q,t\right) = f_q \exp\left[-\left(\frac{t}{\tau}\right)^{\beta}\right] \tag{2.45}$$

where f_q gives the amplitude of the atomic vibrations. The parameter $\beta < 1$ specifies the stretching of the relaxation process, resulting in a distribution of τ. In general, however, the microscopic dynamics of non-glass-forming liquids can be described with a simple exponential decay as in e.g. equation 2.42, corresponding to a value of $\beta = 1$ in equation 2.45. Equating equation 2.42 with equation 2.45 and $\beta = 1$ gives the diffusion coefficient as a function of τ determined from $I(Q,t)$; namely,

$$D = \frac{1}{\tau Q^2}. \tag{2.46}$$

Similar to equation 2.44, the diffusion coefficient D can be obtained through the linear slope of $1/\tau$ as a function of Q^2.

2.2.7 Structural analysis of binary alloys

A time independent averades expression of the structure is given by the static structure factor, which can be directly determined (following equation 2.14) by integrating the dynamical structure factor $S(Q,\omega)$ over the inelastic signal ω.

$$S(Q) = \int_{-\infty}^{\infty} S\left(Q,\omega\right) \mathrm{d}\left(\hbar\omega\right) \tag{2.47}$$

In case of binary mixtures the total structure factor $S(Q)$ consists of three partial structure factors, which origin from the specific atomic correlation of the alloyed components A and B: S_{AA}, S_{BB} and S_{AB}. According to Faber-Ziman's formalism those partial structure factors are related to the measured differential cross-section with the respective concentration c and coherent scattering length b [121].

$$\left(\frac{\delta\sigma}{\delta\Omega}\right)_{coh} = \frac{c_A^2\overline{b_A}^2}{\overline{b^2}} S_{AA}(Q) + \frac{c_B^2\overline{b_B}^2}{\overline{b^2}} S_{BB}(Q) + \frac{2c_A c_B\overline{b_A b_B}}{\overline{b^2}} S_{AB}(Q) + \frac{\overline{b^2} - \overline{b}^2}{\overline{b^2}} \tag{2.48}$$

Here the mean scattering length is given by:

$$\bar{b} = c_A \overline{b_A} + c_B \overline{b_B} \tag{2.49}$$

$$\overline{b^2} = c_A \overline{b_A^2} + c_B \overline{b_B^2} \tag{2.50}$$

This formalism can be rewritten in terms of the topological and chemical short-range order. Following Bathia-Thornton's formalism [122] the partial structure factors S_{NN}, S_{CC} and S_{NC} can be related to the measured differential cross-section by

$$\left(\frac{\delta\sigma}{\delta\Omega}\right)_{coh} = \frac{\bar{b}^2}{\overline{b^2}} S_{NN}(Q) + \frac{c_A c_B \left(\overline{b_A} - \overline{b_B}\right)^2}{\overline{b^2}} S_{CC}(Q) + \frac{2\left(\overline{b_A} - \overline{b_B}\right)\bar{b}}{\overline{b^2}} S_{NC}(Q). \tag{2.51}$$

Here S_{NN} refers to the topological short-range order, S_{CC} to the chemical short-range order and S_{NC} to a correlation of particle density and chemical composition.

The partial structure factors S_{AA}, S_{BB} and S_{AB} and accordingly S_{NN}, S_{CC} and S_{NC} can be directly determined by solving a system of linear equations. Therefore, measurements of three independent total structure factors $S(Q)$ with different scattering contrast are needed. This can be achieved by employing different scattering methods, e.g. neutron scattering and x-ray diffraction. Additionally, neutron scattering offers the possibility to detect total structure factors with varying scattering contrast by using elemental isotopes with different coherent scattering lengths b_{coh}.

In Fig. 2.5 the neutron scattering lengths of elements are depicted. As can be seen, five elements - namely Hydrogen ($b_{coh}(H) = -3.74$ fm), Lithium ($b_{coh}(Li) = -1.90$ fm), Titanium ($b_{coh}(Ti) = -3.438$ fm), Vanadium ($b_{coh}(V) = -0.38$ fm) and Manganese ($b_{coh}(Mn) = -3.73$ fm) - own a negative coherent scattering length (total values for all elements and isotopes can be found in [112]). In binary mixtures containing one of those elements an alloy composition can be found which mean scattering length equals zero according to equation 2.49. In case of this zero scattering composition the partial contribution of S_{NN} and S_{NC} in equation 2.51 vanish. A neutron diffraction experiment investigates then the chemical short-range order characterized by S_{CC} directly.

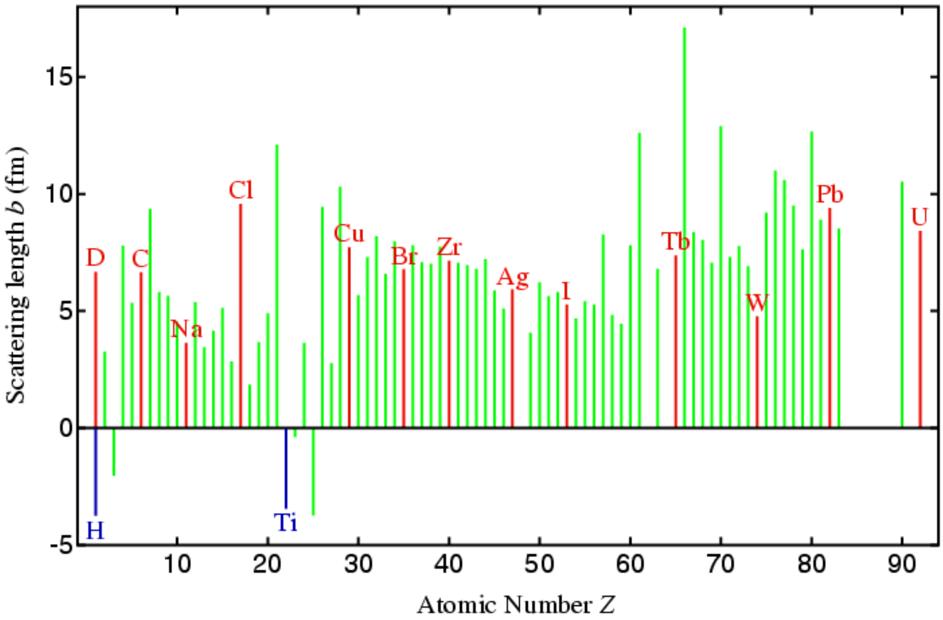

Figure 2.5: Scattering length b in fm as a function of the atomic number Z of elements [123]. Some elements are labeled. Here, the red lines refer to elements with positive scattering length and the blue lines to elements with negative scattering length. Unmarked elements are referred by green lines.

2.3 Short-range order in metallic melts

Decades of research show interest in the short-range order of atoms in metallic melts. Already in 1952 Frank postulated an icosaedral short-range of monoatomic melts [124] as explanation for Turnball's investigation on the supercooling of metallic liquids [125]. A melt with icosaedral structure has a coordination number of $Z = 12$, which is equivalent to 12 nearest neighbors. It is densely packed and has a symmetry, which is incompatible with the translation invariance of crystals. Therefore it is impossible to assemble solid crystals out of icosaeda. The resulting rather high differences in surface energy between the liquid and solid phases yield a high energy barrier ΔG for nucleation, which leads to a good undercoolability of melts.

In monoatomic metallic melts - namely the early transition metal group 4 elements Ti and Zr as well as for late transition metals like Fe or Ni - an icosaedral short-range order was found by neutron diffraction experiments combined with simulations of the structure factor [65, 66].

For metallic alloys it is rather complicated - and for multi-component systems even impossible - to investigate the atomic short-range order of single alloy components, since partial structure factors can just be obtained indirectly employing independent measurements with different scattering contrasts. In some metallic alloys with strong chemical interactions icosaedral short-range order was found [72, 126]. Detailed research was focused to obtain the partial structure factors in binary metallic melts. For Ni-Nb [127], Ni-Si [128], Zr-Ni [64, 129] and Hf-Ni [63] the short-range order was investigated. The preferred nearest neighbors and the coordination numbers could be obtained, indicating no dominance of icosaedral short-range order for these alloys.

Sometimes, only total structure factors are obtained and the total pair-correlation function is discussed [83, 130, 131]. However, the total pair-correlation function is not suitable for a detailed investigation of the atomic short-range order. In contrast, partial structure factors defined by ab initio MD simulations are available for Al-Ni [132], Li-Bi [133], Ag-Ge [134], Zr-Ni [135] and Al-Cu [136].

In all referred reports the interplay between the short-range order and the dynamical properties of the respective components are discussed. Many suggest an influence of the chemical short-range order on the dynamical properties of the melt. However, the detailed mechanisms remain still largely unknown, which requires detailed investigations of short-range order in combination with the atomic dynamics to explain melt properties.

2.4 Packing fraction

The effect of packing has a huge impact on the microscopic and macroscopic dynamics in metallic melts [58]. Normally, a higher packing fraction of melts correlates with lower melt dynamics.

The packing fraction can be calculated based on the melt density. Therefore, at first the mean atomic volume $\overline{V_{at}}$ needs to be defined, using the mean molar mass $\overline{M}$ of the respective alloy components, the measured density ρ and the Avogadro constant N_A.

$$\overline{V_{at}} = \frac{\overline{M}}{\rho N_A} \tag{2.52}$$

Furthermore, the calculated atomic volume is needed:

$$V_A = \frac{4}{3}\pi\overline{r}^3 \tag{2.53}$$

Here $\overline{r}$ is the mean of the alloy components radii. Here one can consider either covalent radii [67] or Goldschmidt radii, which correspond to atomic distances in the solid [137]. However, due to the disordered nature of liquids like metallic melts it is rather difficult to depict the atomic radii. This topic is comprehensively discussed in the first results section of this work. Nevertheless, in case of metallic melts the absolute scale of the packing fraction is less important than the actual discrepancies in packing between different systems [127]. Therefore, a consistent set of radii needs to be considered, what is in any case topic of discussion [138]. The packing fraction ϕ is then given by

$$\phi = \frac{V_A}{\overline{V_{at}}}. \tag{2.54}$$

2.5 Mode-coupling theory

The mode-coupling theory (MCT) of the glass transition provides a direct link between the dense liquid's structure and its dynamics [68]. MCT takes as input the equilibrium partial static structure factor of the liquid and is able to predict the dynamical behavior, e.g. self- and inter-diffusion coefficients [139–143]. At the critical temperature T_c MCT predicts an ideal glass transition, where the diffusion coefficient converges to zero [144].

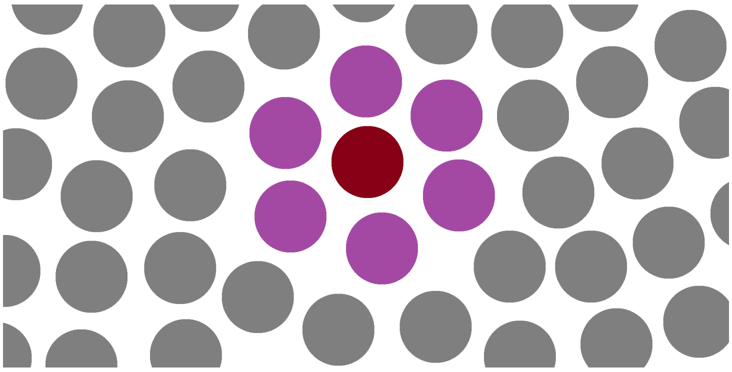

Figure 2.6: Schematic 2D model of a monoatomic melt to visualize the "cage effect" in MCT. The red sphere depicts the center atom, which is surrounded by the cage formed by the violet atoms.

In liquids atoms are surrounded by a dynamic cage of nearest neighbors. This "cage model" is an intuitive picture of MCT [145]. The motion of atoms in densely packed liquids are highly correlated. A self-diffusion process of the central atom can take place by structural relaxation if the collective dynamics cause an opening of the cage. This refers to the relaxation described in 2.2.6. Hence, atomic motion of a tagged particle is described by a density correlator $\phi^s_Q(t)$, which is the equilibrium average of the density fluctuations:

$$\phi^s_Q(t) = \left\langle \varrho^*_{\vec{Q}}(t)\varrho_{\vec{Q}}(0) \right\rangle \tag{2.55}$$

Here, $\varrho_{\vec{Q}}$ is the Fourier-transformed tracer particle density $\varrho\left(\vec{r}\right) = \delta\left(\vec{r} - \vec{r}^s\right)$. With increasing temperature (and lower packing) the microscopic density correlations decay faster, what is equivalent to smaller relaxation time and greater diffusion coefficient. By lowering the temperature down to T_c (or increasing the packing fraction ϕ_c) density correlations mark a finite value, the relaxation time diverges $\tau = \infty$ and the diffusion coefficient equals $D = 0$. The liquid passed the glass transition and composed a solid glassy structure [144].

The equations of motion are similar to that of a time-dependent harmonic oscillator

$$\ddot{\phi}^s_Q(t) + \Omega^2_Q \phi^s_Q(t) + \Omega^2_Q \int_0^t m^s_Q\left(t - t'\right) \dot{\phi}^s_Q\left(t'\right) \mathrm{d}t' = 0, \tag{2.56}$$

with $\Omega^2_Q = v^2 Q^2$. Here v is the thermal velocity. An essential element is here the memory kernel $m^s_Q\left(t - t'\right)$ which is a force-force correlation function describing the cage dynamics from the density fluctuations. Particles in motion can interact at time t with the density wave they induced by density fluctuations at time t'. $m^s_Q(t)$ is expressed by

$$m^s_Q(t) = F\left[\phi^s_Q\left(t\right), \phi^{\alpha\beta}_Q\left(t\right)\right] = \sum_{k,\alpha\beta} V_{Q,kp} \phi^s_k(t) \phi^{\alpha\beta}_p(t) \tag{2.57}$$

with $p = \left|\vec{Q} - \vec{k}\right|$. Here, $\phi^{\alpha\beta}_Q\left(t\right)$ is the density-correlation function of the bulk, where α and β represent the respective components of the mixture. $\phi^{\alpha\beta}_p(t)$ is expressed by a matrix, which can be derived similar to equation 2.56 and 2.57 [143]. The coupling vertices $V_{Q,kp}$ include the static structure factor S_Q, which can be measured in diffraction experiments (e.g. using neutrons or synchrotron x-rays). Following, MCT predicts transport coefficients such as the self-diffusion of atoms or inter-diffusion coefficients.

MCT can be used to analyze different diffusive regions and investigate the effect of packing [143]. In addition, it considers the influence of the chemical short-range order on mass transport. Recently, a decoupling of diffusion coefficients as seen by quasielastic neutron scattering could be explained by MCT [63]. In conclusion, MCT is a useful tool to understand the dynamics of glass-forming liquids and the corresponding transport mechanism.

2.6 Viscosity

Another important thermophysical property of the melt is the viscosity, which describes - in contrast to the atomic motion (diffusion) - the macroscopic dynamics. Its inverse value is the fluidity. It can be described by the shearing of layers within the liquid.

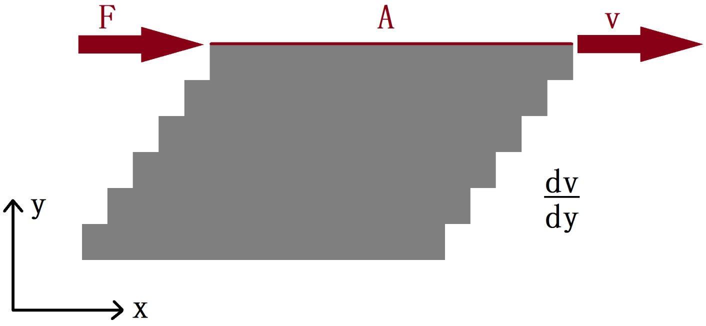

Figure 2.7: Schematic model of viscosity η. A is the surface layer of the liquid, where the force F causes a displacement with the velocity profile $\frac{dv}{dy}$

In Fig. 2.7 different layers along the surface A are arranged in y-direction. If the topmost layer gets displaced in x-direction by a certain force F and velocity v, a velocity profile in y-direction $\frac{dv}{dy}$ results, which is proportional to the force F.

$$F = \eta A \frac{dv}{dy} \tag{2.58}$$

Here η is the viscosity. Hence, the viscosity describes the friction between the different liquid layers. In case of a Newtonian fluid, the viscosity is independent from the shear velocity [146]. Metallic melts can be considered as Newtonian fluids.

2.7 Stokes-Einstein relation

One of the empirical relation between both dynamical quantities, the macroscopic viscosity and the microscopic diffusion of atoms, is given by the empirical Stokes-Einstein relation. It is derived in order to describe the motion of spherical particles within a homogeneous liquid [6, 147] and supposes the validity of Stoke's law of friction [148] for spherical particles of the radius r within a homogeneous liquid of the viscosity η.

$$F_R = 6\pi v\eta r \tag{2.59}$$

Here v is the velocity of the spherical particles, which are affected by the force of friction F_R. In the work on the theory of Brownian motion Albert Einstein related in 1905 the diffusion coefficient D of spherical particles to the viscosity η of the liquid at a given temperature T [6].

$$D\eta = \frac{k_B T}{6\pi r_H} \tag{2.60}$$

Here k_B is the Boltzmann constant and r_H is the hydrodynamic radius.

Although the Stokes-Einstein relation was found to be valid in liquids like e.g. Benzene and Tetramethylsilan [149], a breakdown was reported in a variety of metallic melts [80, 82, 150–156]. This is due to several reasons. For example, in multi-component systems a dynamical heterogeneity is found, which can cause deviations of several orders of magnitudes [157]. However, a major problem is, that the hydrodynamic radius a_{hyd} is an arbitrary quantity, which just gets estimated and often deviates from actual atomic radii. This applies also in case of single component melts. Here, a detailed investigation of the relation between hydrodynamic radius and atomic radii is discussed in the first part of this work on the basic example of Mercury. In addition, Stoke's law of friction (see equation 2.59) scales macroscopic particles, which are orders of magnitudes larger than the atomic dimension in metallic melts.

To analyze the Stokes-Einstein relation in metallic melts a high quality of diffusion and viscosity data is required. Precise diffusion coefficients can be measured by quasielastic neutron scattering. Viscosity data, which are rather complicated to determine due to the high applied temperatures and reactive nature of metallic melts, can be reliably determined using the oscillating droplet method in levitation. The combination of these methods enables an accurate investigation of the validity of the Stokes-Einstein relation in metallic melts, for which reason the breakdown predominantly got reported within the recent decade and still is subject of research.

3 Experimental methods and instruments

3.1 Levitation

The widely-used levitation techniques for container-less processing of liquid metallic samples are aerodynamic levitation (ADL) [158, 159], electrostatic levitation (ESL) [160, 161] and electromagnetic levitation (EML) [70, 162]. In ADL the samples are blown by a gas jet nozzle, in ESL samples are levitated by an electrostatic field and in EML using electromagnetic forces.

In this work, electrostatic and electromagnetic levitation was used to study the physical properties of liquid metals. The specific characteristics and benefits of both techniques in the laboratory setup and in combination with scattering experiments (e.g. neutron diffraction, quasielastic neutron scattering and x-ray diffraction) are specified below. A detailed overview of the different levitation techniques when combined with neutron scattering can be found in reference [163].

3.1.1 Electrostatic levitation (ESL)

Electrostatic levitation (ESL) is one of the most powerful and promising ways of accurately studying reactive metallic melts over a broad temperature range, and thus allows to explore the deeply undercooled liquid and to form new metastable and glassy phases [164]. By avoiding 1. heterogeneous nucleation at the container wall, 2. chemical reactions of the melt and the container materials and 3. melt contamination from e.g. the atmosphere, dirt or adsorbate at the container, this state-of-the-art technique enables highly accurate measurements of important thermophysical melt properties. In the stationary laboratory setup melt properties like density [165–171], viscosity [82, 85, 170–174], ratio of specific heat capacity to total hemispherical emissivity [166, 175, 176], undercoolabilty and nucleation behaviour [177–179] as well as crystal growth velocity [13, 14, 180–183] can be investigated.

Mobile ESL setups can be installed at neutron and synchrotron scattering beam lines for highly accurate measurements of the atomic dynamics [50, 59, 63, 80, 184–186], as well as in-situ structural studies [130, 165, 184, 187–189].

In Fig. 3.1 a schematic sketch of an ESL is depicted. To levitate the sample in vertical direction samples are positioned in an electrostatic field between the top and bottom electrode, which is created by a high-voltage. The sample levitates if the Coulomb force on a charged sample is greater than gravity. The sample position is stabilized by two pairs of horizontally arranged side electrodes with polar voltages. To minimize any flashovers the samples are processed under ultra high vacuum ($\approx 10^{-7}$ mbar). According to Earshaw's theorem no potential minimum exists in electrostatic fields [190]. Therefore, active controlling of both the vertical and the horizontal position is necessary [161, 191].

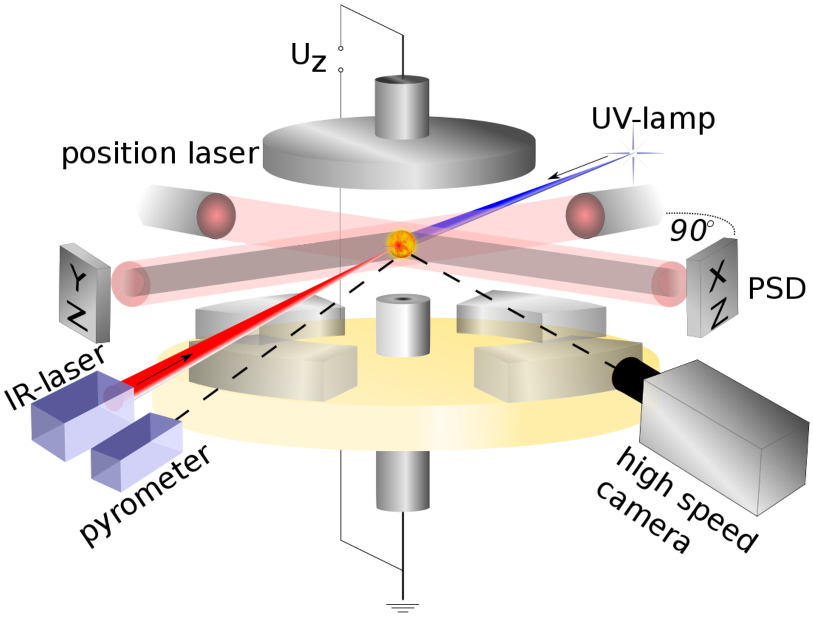

Figure 3.1: Schematic sketch of a sample processed in electrostatic levitation (ESL). The sample is levitated between the top and bottom electrode. The four surrounding electrodes control the horizontal sample position. [192]

The sample position is logged by two perpendicularly oriented position sensitive detector (PSD), which record the sample shadow induced by the position lasers. In case of a shadow movement the electrode voltage gets adjusted actively. Heating and melting of the sample is conducted by a 75 W infrared laser ($\lambda = 808$ nm). Any charge loss during heating, which might be induced by evaporation of impurities dissolved in or adsorbed on the sample, is compensated using a UV-lamp, which charges the sample positively due to the photoelectric effect. This charging by illumination with UV-light is essential at temperatures below ca. 1000 K. At higher temperatures thermionic emission is sufficiently strong.

As depicted in Fig. 3.2 only the sample appears in the levitation plane, leading to an excellent signal-to-noise ratio in scattering experiments. In addition, essentially no secondary scattering from the experimental setup affects the measurement. This is an issue for electromagnetic levitation, which requires a careful shielding of the levitation coil during scattering experiments.

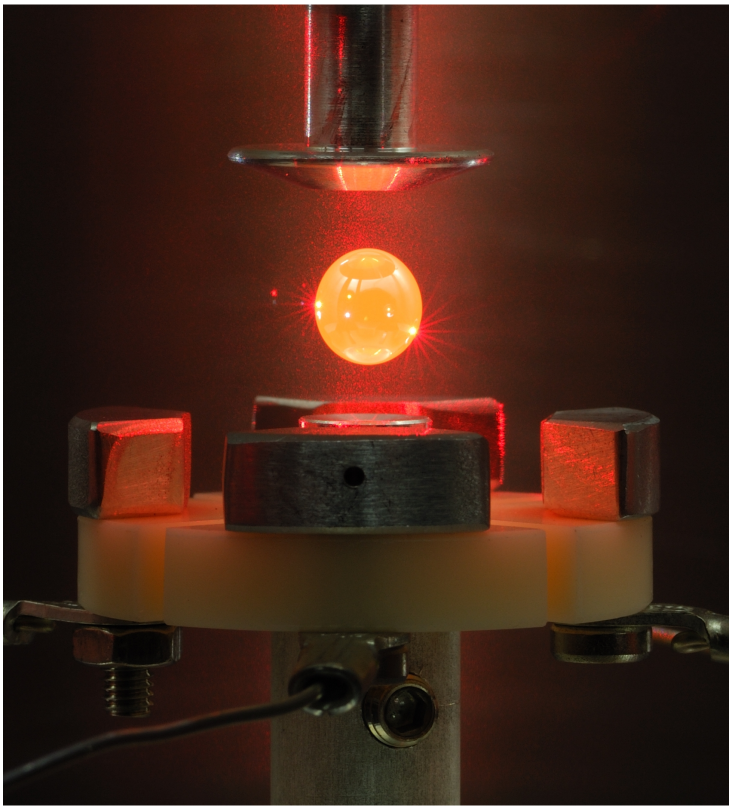

Figure 3.2: A molten metallic sample in electrostatic levitation (ESL). Image by courtesy of DLR-MP.

3.1.2 Electromagnetic levitation (EML)

Another method to process metallic melts is elctro-magnetic levitation (EML), which first was introduced in 1954 by Westinghouse [69]. Samples get both levitated and heated by a radio frequency electromagnetic field due to Lorenz force in a specially winded copper coil.

$$\vec{F_G} = m * g = \vec{F_L} = -\frac{\nabla \vec{B}^2}{2\mu_0}\frac{2\pi}{3}r_d^3 Q(q) \tag{3.1}$$

Here μ_0 is the magnetic permeability, r_d the sample radius, q a dimensionless parameter with $q = r_d/\delta$, $\delta = \sqrt{\frac{2\rho_e}{\mu_0}}$ the skin depth of a magnetic field $\vec{B}$ with frequency ω, the efficiency ratio $Q(q)$ and the electrical resistivity ρ_e. The magnetic field induces eddy currents within the sample, which heat it. The respective heating power P_H is

$$P_H = \frac{\vec{B}^2\omega}{2\mu_0} V H(q) \tag{3.2}$$

with the sample volume V and efficiency ratio of power absorption $H(q)$ [146].

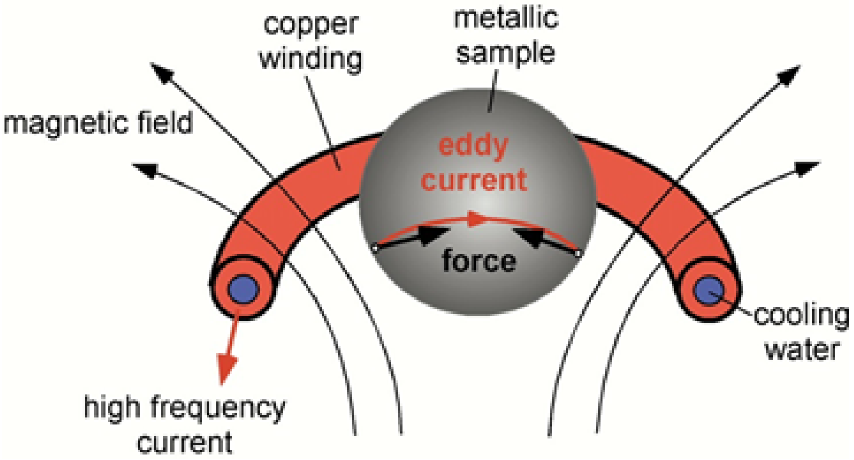

Figure 3.3: Sketch of the occurring Lorenz force in electromagnetic levitation (EML). Drawing by courtesy of DLR-MP.

For EML the heating and levitation process are coupled. Since $\vec{B}$ includes the mass the heating can only be modified by the levitated sample dimension. A certain minimum of the field is required to levitate the sample, which induce a certain temperature (heating). In addition, an active gas cooling (see nozzle in Fig. 3.4) is applied to further enlarge the accessible temperature range, especially towards lower temperatures. Processing takes place under inert gas atmosphere. Therefore, the sample chamber gets first evacuated to ultra high vacuum ($\approx 10^{-7}$ mbar) and is afterwards flooded by ultra purity gas.

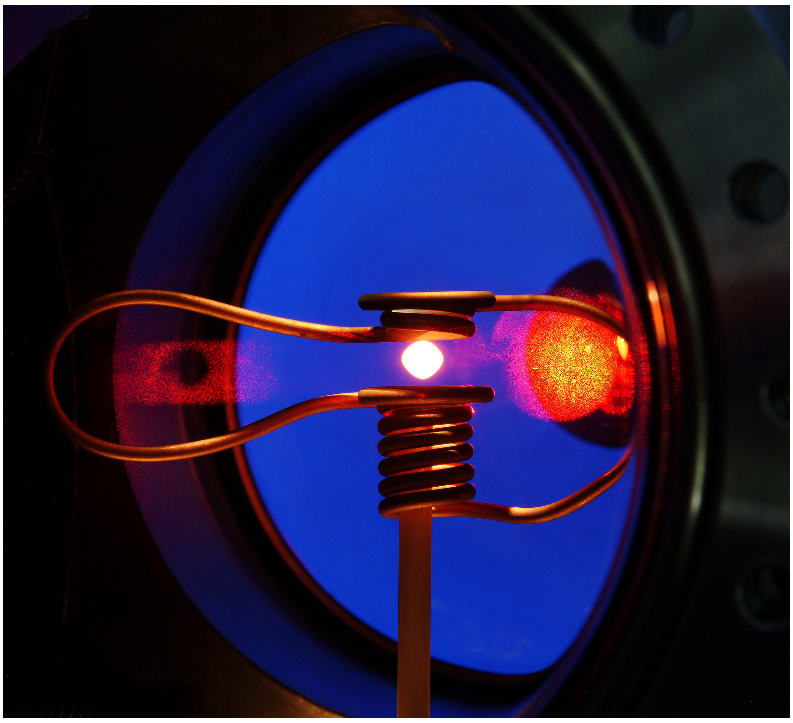

Figure 3.4: A molten metallic sample in electromagnetic levitation (EML). The sample is levitated and heated by the coil system. Gas cooling can be applied through the bottom nozzle. Image by courtesy of DLR-MP.

Whereas in EML only conductive samples can be processed (according to Lorenz force) ESL also allows the levitation of non-conductive materials. Another major difference is marked by the processing under gas-atmosphere. This allows the measurement of materials with high vapor pressure, which would tend to evaporate in the ESL vacuum. On the other hand impurities within the gas atmosphere may lead to sample contamination. With laboratory setups experiments like density measurements [146, 193–195] and surface tension investigations [146, 193, 196] are feasible by use of EML. Additionally, mobile EML setups have been developed for use at large scale facilities, which can be utilized for instance to investigate the melt dynamics [57, 60, 73, 197–199] and structure [65, 66, 70–72, 129, 200, 201].

Since the induced Lorenz force points from the coil towards the sample position (see 3.3) different from ESL the samples are levitated under stable conditions. However, these forces deform the melt as well (as one can see in 3.4). Therefore, viscosity measurements are impossible in ground-based EML.

With the TEMPUS facility a microgravity EML setup for parabolic flights was developed to enable viscosity investigations [85, 146, 202–204]. Additionally, an EML setup aboard the Columbus module of the International Space Station (ISS) exists [205]. Due to the small required forces of the levitation process a completely different coil design is applied in microgravity. The heating process and levitation are decoupled from each other and generated by different coil systems. This allows detailed measurements of the thermophysical properties and investigations of the undercooling and force-free solidification behavior of metallic melts [12, 206].

3.1.3 Temperature measurement

One technique to contact free determination of the sample temperature is to measure the intensity of the thermal radiation emitted from the sample using a pyrometer [207]. It relates the spectral radiance I at a wavelength λ with the surface temperature T emitted by a black body in thermal equilibrium according to Planck's law [208, 209]:

$$\epsilon\left(\lambda,T\right)I\left(\lambda,T\right)=\frac{2hc^2}{\lambda^5}\left[\exp\left(\frac{hc}{\lambda k_BT}\right)-1\right]^{-1} \tag{3.3}$$

Here $\epsilon\left(\lambda,T\right)$ is the emissivity indicating the ratio between emitted power of physical and black body. In case of a black body $\epsilon\left(\lambda,T\right)=1$. The emissivity depends on the wavelength λ, temperature T and the sample surface texture. However, for the study here the emissivity is assumed to be temperature independent as long as no phase transitions occur [210]. Therefore, $\epsilon\approx const.$ at constant wavelength. To convert the temperature T^{pyro} measured with the pyrometer to the real temperature T^{real} the Wien approximation for small wavelengths is used [211].

$$\epsilon\left(\lambda,T\right)I\left(\lambda,T\right)=\frac{2hc^2}{\lambda^5}\exp\left(-\frac{hc}{\lambda k_BT}\right) \tag{3.4}$$

If the measured spectral sample radiance remains unchanged the relation $\epsilon_1I_1\left(\lambda,T_1\right)=\epsilon_2I_2\left(\lambda,T_2\right)$ is given. The product of $\epsilon_{1,2}$ and $I_{1,2}$ is then dependent on the temperature $T_{1,2}$ and it can be followed

$$\frac{1}{T_2}-\frac{1}{T_1}=\frac{\lambda k_B}{hc}ln\left(\frac{\epsilon_2}{\epsilon_1}\right) \tag{3.5}$$

This equation applies for T^{real} and T^{pyro} with respective ϵ_{real} and ϵ_{pyro} as well as for the literature value of the liquidus temperature T_L^{lit} and the measured value T_L^{pyro} with respective ϵ_L^{lit} and ϵ_{pyro}. Considering the assumption for liquid metals the relation $\epsilon_{real}=\epsilon_L^{lit}$ is found. Therefore, the real temperature values can be converted from the pyrometer data as follows

$$\frac{1}{T^{real}}-\frac{1}{T^{pyro}}=\frac{1}{T_L^{lit}}-\frac{1}{T_L^{pyro}} \tag{3.6}$$

Deviation in the temperature data may result from the uncertainty in the determination of T_L^{pyro} and from the inaccuracy of the pyrometer $\Delta T/T\approx 0.1-0.3\%$. This sums up in an absolute error of $\Delta T=\pm5$ K. The maximum sampling rate of the applied pyrometer is 10 kHz, equivalent to a measurement time of 0.1 ms and the accessible temperature range is 300°C to 2500°C [212]. In this work a sampling rate of $\Delta t=0.01$ s was applied.

3.2 Scattering experiments

3.2.1 Quasielastic neutron scatting (QENS)

QENS probes the distribution of energy transfers by atomic motion, which appear as a broadening of the elastically scattered spectrum. Since the incoherent QENS signal emanates from single-particle dynamics, it is particularly suited to study process such as self-diffusion. In principle, inter-diffusion coefficients can also be measured using QENS; for that purpose, partial scattering functions must be obtained with sufficient accuracy.

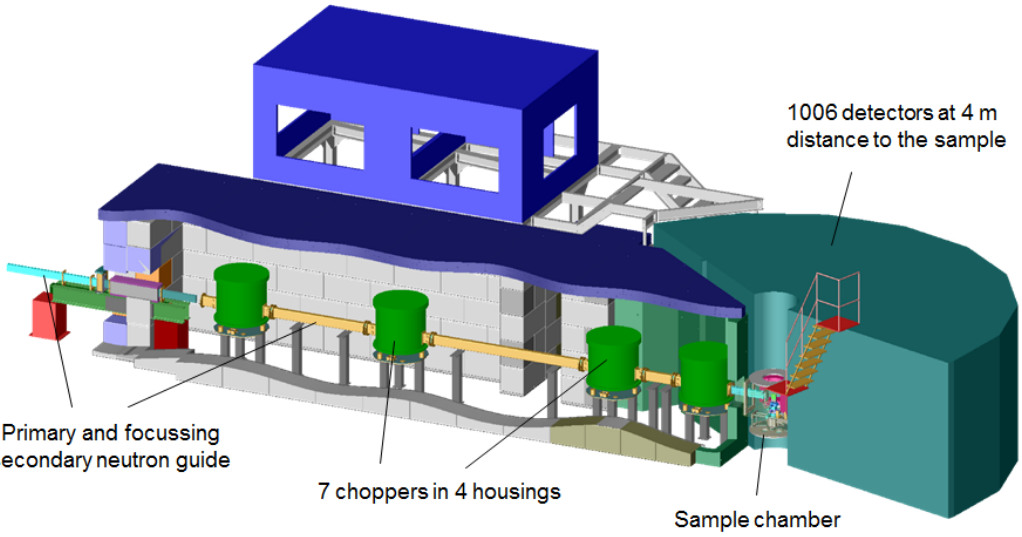

Figure 3.5: Detailed sketch of the multi-disc chopper time-of-flight spectrometer TOFTOF at the Heinz Maier Leibnitz Zentrum (MLZ) in Munich. Drawing by courtesy of TUM-MLZ.

For the study here QENS measurements were carried out at the multi-disc chopper time-of-flight spectrometer TOFTOF at the Heinz Maier-Leibnitz Zentrum (MLZ) in Munich (see Fig. 3.5) [213, 214]. The cold source – a moderator of liquid deuterium D_2 at a temperature 25 K – provides TOFTOF with an integral white beam neutron flux of ca. 10^{10} n cm^2 s^{-1}, which gets pulsed and monochromatized by seven choppers before the sample position. 1006 detectors provide a measurement of both, the angular information and the energy transfer, which is detected by the change of the time-of-flight (or velocity) of the neutron before and after the scattering process.

The neutron guide system of TOFTOF is divided in two parts: the primary s-shaped guide and the secondary linear focusing guide in the chopper systems.

The s-shaped curved neutron guide works as a velocity filter with a cutting edge wavelength 1.38 Å, which can be calculated with the radius of the curvatures of $r_c = 2km$ and the width of the guide of 44 mm. Furthermore a direct sight to the cold source is avoided, which suppresses γ-radiation. Due to the s-shaped curvature over 46 m in the neutron guide hall the resulting neutron beam profile is well symmetrically over the area of the neutron guide.

In the secondary 12.2 m long linear focusing guide, the neutron beam cross-section is compressed from 100×44 mm^2 to 44.8×23 mm^2. The guide system ends 20 cm in front of the sample.

Due to the reflectivity of the guide system and the spectrum of the cold source, the upper wavelength limit for usable neutrons is ca. 12 Å. Manipulation of the chopper system allows for the incident neutron wavelength to be selected in a broad range from 1.38 Å to 12 Å.

Before interacting with the sample, the neutron beam passes through the primary spectrometer, which consists of seven choppers, actively controlled by magnetic bearings arranged in four housings. The chopper discs are made from a neutron absorbing ^{10}B-coated carbon-fiber-reinforced polymer with a diameter of 60 cm and a mass of 5.9 kg. The chopper discs can be rotated with a frequency of up to 22000 rpm.

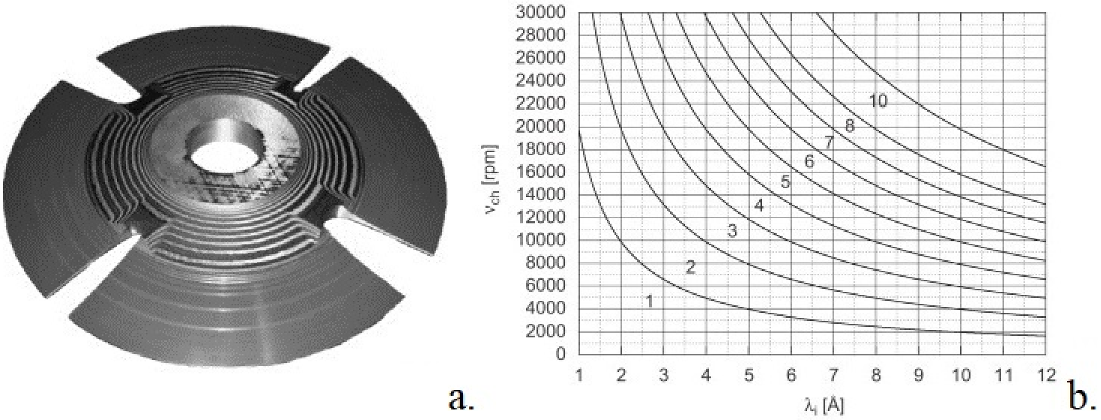

Figure 3.6: (a) Picture of a chopper disc; (b) illustration of the chopper rotation frequency according to equation 3.7. Figure and graph by courtesy of TUM-MLZ.

The seven choppers are arranged into three chopper pairs and one individual chopper, and are contained within four separate chopper housings. The function of the different choppers is as follows:

1. Housing (Chopper 1 and 2): A pair of counter rotating choppers cut the white neutron beam in polychromatic neutron pulses

2. Housing (Chopper 3): Elimination of higher order wavelengths

3. Housing (Chopper 4): Elimination of higher order wavelengths; (Chopper 5): Preventing frame overlap by blocking out several pulses

4. Housing (Chopper 6 and 7): A pair of counter rotating choppers cut out a small wavelength range to monochromatize the neutron pulses

All choppers rotate with the same frequency, except for the frame overlap chopper 5, which frequency (in rpm) can be calculated with respect to the present geometries and allowing neutrons with a wavelength larger than 1.5 times the mean wavelength of the incident neutrons λ_i (in Å) to overlap to [213]

$$v_{ch} = 1.978 \times 10^4 \frac{n}{\lambda_i}. \tag{3.7}$$

Here, n is the frame overlap ratio.

Between the primary spectrometer and the sample, a monitor (efficiency approximately 10^{-5}) is located, which records the intensity of the incident neutrons by triggering a detectable nuclear fission in fissile ^{235}U.

After impinging on the sample, most of the neutrons pass directly through without interacting and end up in the beam stop, which is located 16 cm behind the sample. Typically the sample thickness is chosen such that 10 % of the monochromatic incident beam is scattered by the sample. This compared to the incident beam small ratio of scattering serves to keep multiple scattering events in sample small [215]. After passing through a radial Gd_2O_3 collimator, the scattered neutrons enter the flight chamber, where 1006 ^{3}He-detectors are located tangential to the intersection lines of the Debye-Scherrer-cones 4 m away from the center of the sample. The detectable scattering angle 2θ covers the regions $-15°$ to $-7°$ and $7°$ to $140°$.

The flight chamber, as well as the sample chamber, is filled with Argon gas to avoid air scattering. Shielding of the detectors by polyethylene and B_4C eliminates parasitic neutrons. Both measures bring TOFTOF to an unsurpassed suppression of background.

Each of the 1006 detector tubes has an active area of 40×3 cm^2 and a mean thickness of 14.5 mm. The tubes are filled with 97 % ^{3}He and 3 % CF_4 at a total pressure of 10 bar, which react with the neutrons into charged tritium and protium

$$n +^3 He \rightarrow^3 H +^1 H + 0.764\ MeV. \tag{3.8}$$

The area between the detectors and the back wall of the flight chamber is shielded with cadmium to avoid re-scattering already detected neutrons.

The instrumental energy resolution as well as the incident flux onto the sample depend upon both the chopper rotation frame and the neutron wave length.

In Fig. 3.7.a. the calculated elastic line widths are depicted as a function of the incident neutron wave length λ_i for different chopper frequencies. The resolution functions for TOFTOF exhibit a Gaussian line shape.

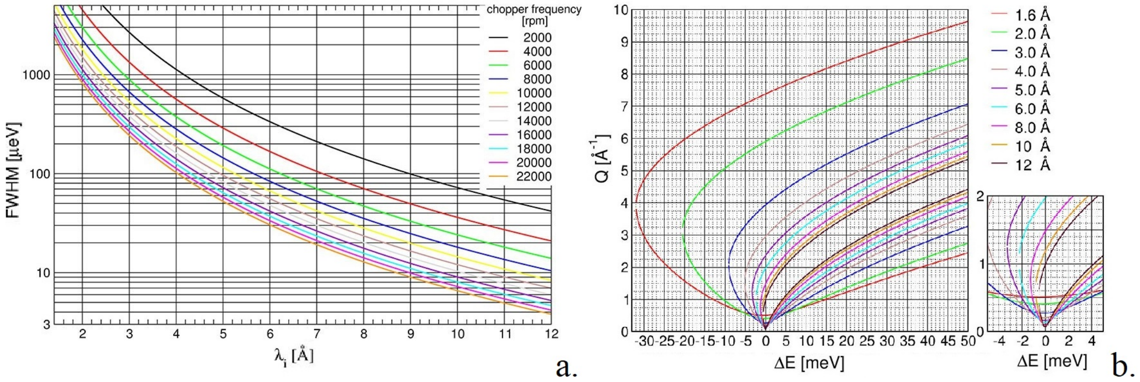

Figure 3.7: (a) Calculated elastic line widths for different chopper frequency; (b) accessible dynamic range with respect to the incident neutron wavelength. Graphs by courtesy of TUM-MLZ.

With changes of the incident neutron wavelength also the accessible dynamic range varies, as shown in Fig. 3.7.b.. However, this representation does not consider any effects due to frame overlaps.

Due to the position far away from the reactor core and the effective shielding of the respective parts, which results in a dark count rate of under 1 count/min, TOFTOF exhibits a typical signal-to-background ratio of up to $\times 10^5$.

The data reduction and evaluation is done using the program FRIDA ("Fast reliable interactive data analysis"), which is designed for the analysis of spectral data, in particular from quasielastic neutron scattering [215, 216]. Amongst other things, FRIDA corrects the background and the detector's efficiencies. Furthermore, isotropic scattering deviations in terms of the Debye-Waller-factor are corrected.

FRIDA contains highly specialized routines handle (e.g. reorganizing, binning, sorting, and cloning data or mathematical operations), fit (e.g. by user-defined functions) and to visualize (e.g. PostScript graphics) tabular data from various formats.

The background was subtracted using the method of Paalman and Pings [217].

$$I^S\left(2\theta,\omega\right) = \frac{1}{A_{S,S+C}} I^{S+C}\left(2\theta,\omega\right) - \frac{A_{rel}}{A_{S,S+C}} I^C\left(2\theta,\omega\right) \tag{3.9}$$

Here $I^{S+C}\left(2\theta,\omega\right)$ is the measured intensity. It reflects the angular and energy dependent scattering of the sample and the sample environment. $I^S\left(2\theta,\omega\right)$ is the intensity of the sample only and $I^C\left(2\theta,\omega\right)$ of the background. $A_{S,S+C}$ corrects neutrons, which get absorbed in the sample environment or the sample after being scattered on the sample. A_{rel} corrects the scattering and absorption of neutron scattered on the sample environment. It can be split up in the quotient $A_{rel} = A_{C,S+C}/A_{C,C}$, where $A_{C,S+C}$ refers to neutrons absorbed in the sample or the sample environment, which got scattered on the sample environment, and $A_{C,C}$, which corrects the overall absorption of the sample environment.

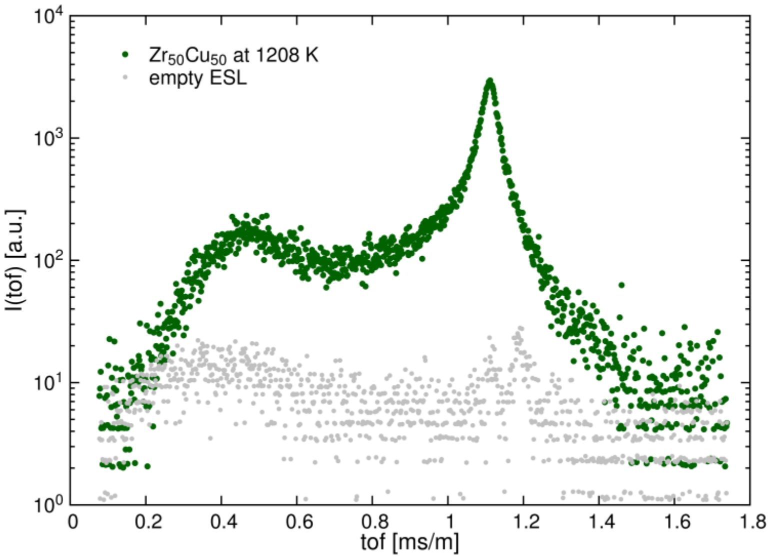

Figure 3.8: Measured time-of-flight spectra of a $Zr_{50}Cu_{50}$ at 1208 K (green) when compared to the empty ESL furnace (grey). The quasielastic broadening of the elastic line of the liquid sample is depicted, which shows a two orders of magnitude larger intensity then the background.

When processing metallic melts in levitation $A_{rel} = 1$ is a good approximation due to the excellent signal-to-noise ratio of EML and ESL. As depicted in Fig. 3.8, the scattering contribution of the sample is two orders of magnitude larger in the quasielastic region than that of the the empty furnace. In this case, the correction can be simplified to

$$I^{S}\left(2\theta,\omega\right)=\frac{1}{A_{S,SC}}\left[I^{SC}\left(2\theta,\omega\right)-I^{C}\left(2\theta,\omega\right)\right]. \tag{3.10}$$

However, an accurate measurement of the empty cell is absolutely essential for levitation experiments. This applies especially in case of the strong absorbing Mercury sample, which got measured using a crucible in reflection geometry. The appropriate background correction is discussed in the first results section of this work.

3.2.2 Neutron diffraction

The diffraction experiments to investigate the atomic structure of melts were carried out at the high intensity 2-axis diffractometer D20 at the Institute-Laue Langevin (ILL) in Grenoble, France. Incident neutrons with a flux of up to 10^8 $\mathrm{s}^{-1}\mathrm{cm}^{-2}$ can be detected after scattering up to a maximum angle of $2\theta = 154°$ [218], which is equivalent to a scattering vector of 10-12 Å^{-1} (at $\lambda = 0.94$ Å) according to the definition of the scattering vector $\vec{Q}$ for elastic scattering.

$$|\vec{Q}| = \frac{4\pi}{\lambda} \sin(\theta) \tag{3.11}$$

To ensure an ideal resolution (compromise between flux, Q range and resolution) the wavelength λ should be of the size of inter atomic distances. Therefore, the white beam originating from the reactor is monochromatized to $\lambda = 0.94$ Å. The width of the neutron beam can be adjusted using slits made of Cd. In addition a B_4C-cover is installed inside the levitator directly in front of the sample in order to minimize irradiation of parts located behind the sample position. Behind the sample a Cd-beam stop is located to suppress the background and to reduce the scattering at the Al-window. This results in an overall Q-range of 0.7 Å^{-1} to 12 Å^{-1}.

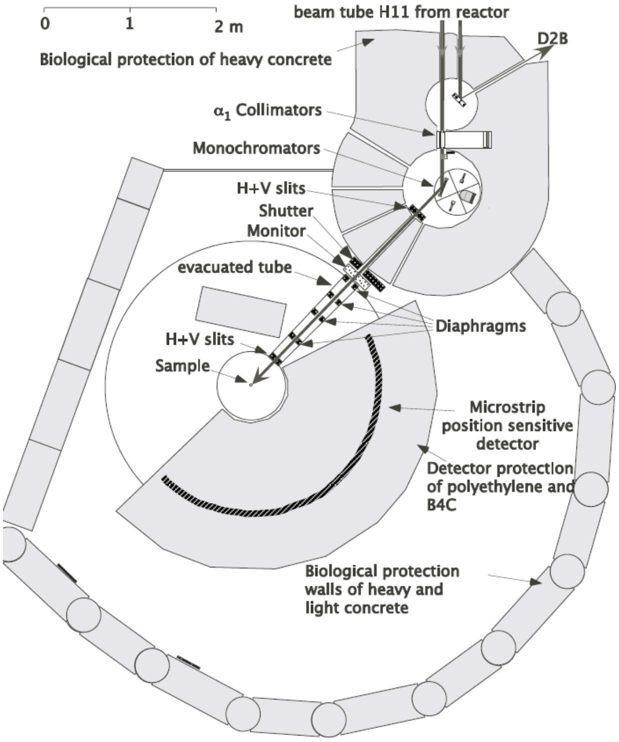
0
1
2 m
beam tube H11 from reactor
D2B
Biological protection of heavy concrete
α1 Collimators
Monochromators
H+V slits
Shutter
Monitor
evacuated tube
Diaphragms
H+V slits
Sample
Microstrip position sensitive detector
Detector protection of polyethylene and B4C
Biological protection walls of heavy and light concrete

Figure 3.9: Schematic view of the high intensity 2-axis diffractometer D20 at the Institute-Laue Langevin (ILL) in Grenoble, France [218]

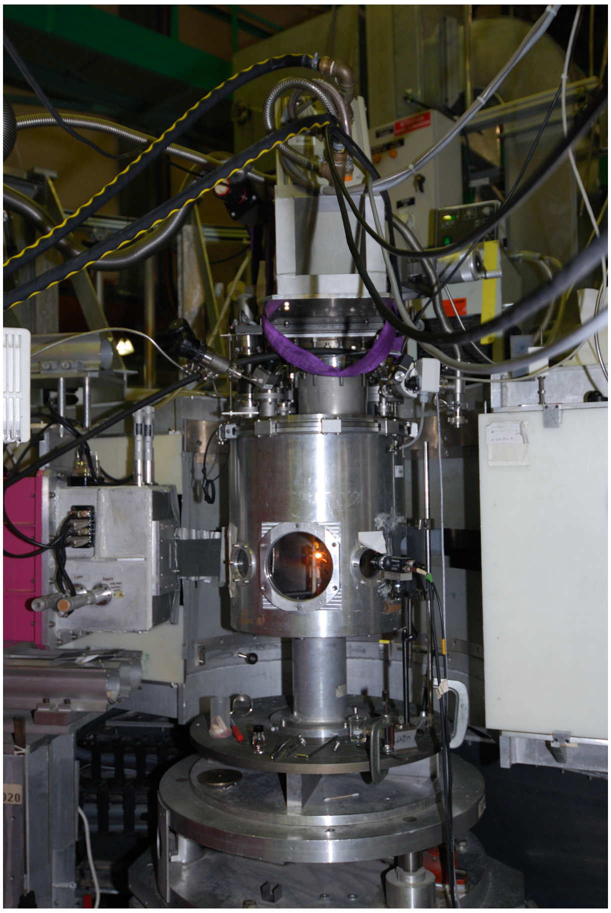

Figure 3.10: Electromagnetic levitator (EML) installed at the instrument D20. Photo by courtesy of DLR-MP.

The background correction follows a similar routine as for the QENS-measurements. To correct the absorption of the sample the intensity of empty can I_{empty} needs to be measured as well as the one of a strong absorber (here a Cd sample) I_{Cd}. Both intensity are summed up to the background intensity I_C according to Beer-Lambert law [219].

$$I_C = I_{Cd}\left(1 - e^{-\mu d}\right) + I_{empty}e^{-\mu d} \tag{3.12}$$

Here μ is the absorption coefficient, which is estimated according to the empty and the Cd measurement, and d the sample thickness. After correcting the self-adsorption [217], the Placzek correction [220] was used to correct the detector count rate of the measured neutrons [221]. All geometrical artifacts emerging from the apparatus or the angular detector efficiency are corrected with a vanadium measurement. To consider multiple scattering effects the correction method of Blech and Averbach was used [222].

3.2.3 X-ray diffraction

Diffraction experiments using x-rays generated by sychrotron radiation were carried out at the materials science beamline ID11 at the European Synchrotron Radiation Facility (ESRF) in Grenoble, France [223]. The underlying scattering law is similar to that described in the previous chapter. In contrast to neutrons, due to different scattering interactions (neutrons scatter on the atom core; x-rays at the atom shell), x-rays exhibit both a Z dependent and angular dependent form factor.

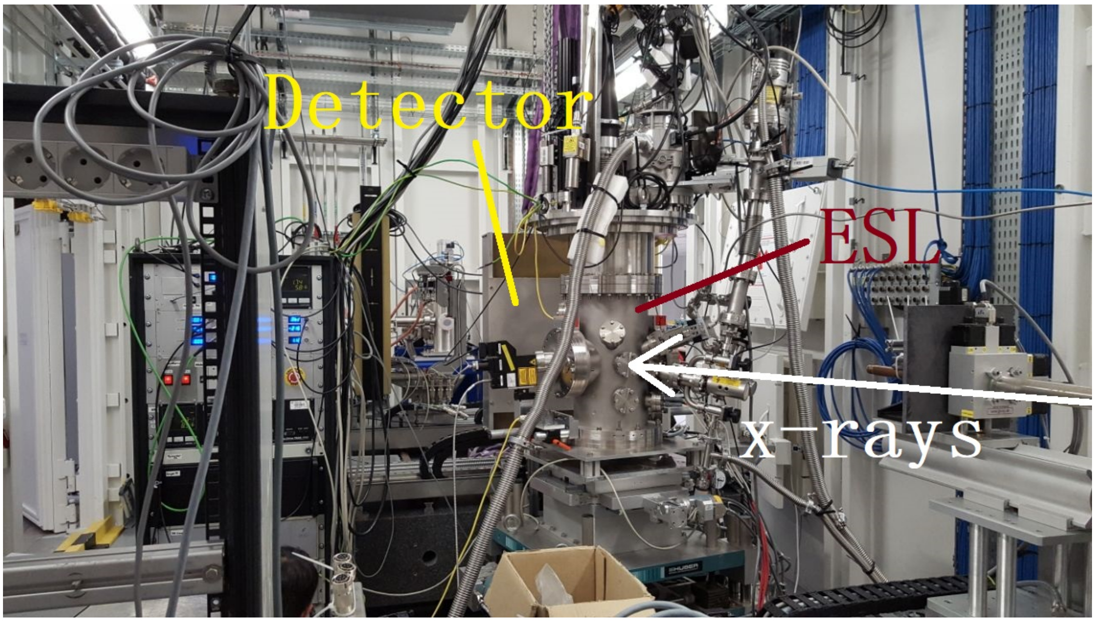

Figure 3.11: Electrostatic levitator (ESL) installed at the materials science beamline ID11 at the European Synchrotron Radiation Facility (ESRF) in Grenoble, France

To detect the scattered x-rays a FRELON camera [224] was placed behind the electrostatic levitator. The distance variable was adjusted to record a quarter of the Debye-Scherrer rings at a maximum scattering vector of $Q = 13$ Å^{-1}. The monochromized x-ray intensity was 100 keV and the detector frame rate was set to 0.5 s. Due to the high intensity of ESRF's sychrotron radiation rather low exposure times are possible to obtain total $S(Q)$, which enables investigations on all appearing structures and phases upon cooling, nucleation and solidification (phase selection). As a comparison: Common isothermal holds at neutron diffraction instruments are on the order of hours to ensure suitable detected statistics.

A CeO_2 powder sample was measured to calibrate the recorded signal. CeO_2 has a quite complex crystal structure exhibiting many known Bragg reflexes, which can be used to calibrate the detector distance to the scattering angle and the wavelength. The recorded Debye-Scherrer ring sections got integrated to $I(Q)$ using the azimuthal integration Python library pyFAI [225] at a wavelength of 0.12437 $Å^{-1}$, which equals to an intensity of 100 keV.

Compared to neutrons the incoherent contributions are insignificant. Whereas neutrons are highly sensitive to different isotopes, the scattering from the respective electron shells of one and the same element in case of x-rays is identical. Only diffusive effects like Compton scattering are present, which must be corrected [226]. Background measurement is also necessary to correct the background as well. The data correction and visualization software PDFGetX2 [227] was used to refine the collected diffraction patterns with the implemented routines of sample self-absorption [217], multiple scattering [222], x-ray polarization [228] and Compton scattering.

3.3 Density measurements

In electrostatic levitation (ESL) the density ρ of metallic melts can be determined containerlessly. Therefore, the shadow of the sample is projected by a cold light source to a camera. Assuming the sample to be rotational symmetric, the temperature T dependent volume V of the sample with the mass m can be calculated from the shadow size. The density is then given by

$$\rho(T) = \frac{m}{V(T)}. \tag{3.13}$$

The edge detection algorithm employed to determine the shadow size was extensively explained by Brillo et al. [162]. For measuring the size of the sample shadow, a camera with a frame rate of 500 fps was used. The recording started triggered with the switch-off of the heating laser. In the following free cooling phase the temperature is measured using a pyrometer and the sample shadow is recorded.

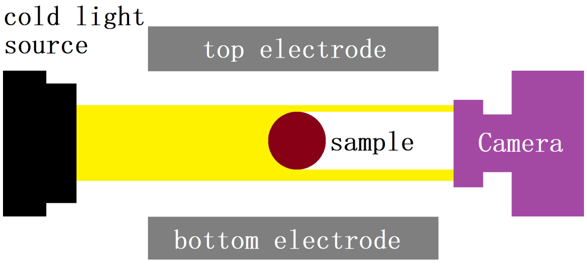

Figure 3.12: Sketch of the density measurement setup in electrostatic levitation (ESL)

During the analysis the volume is then determined by the pixel size averaged over 50 recorded images to minimize any effect of sample vibration. Afterwards the volume is synchronized with the sample temperature measured with a pyrometer. To convert the volume from pixel size px^3 to cm^3 a calibration measurement on steel spheres with known diameter ($d = 2$ mm, 2.381 mm and 2.5 mm) is required under the same ESL configuration than the one of the sample. The cm^3 to px^3 ratio of the calibration measurement can then be adopted to the sample measurement. The given equation for the volume allows then a calculation of the density according to equation 3.13 together with the measured sample mass m.

The stable levitation conditions in ESL lead to nearly rotation symmetric shapes, minimizing the experimental error. The mass loss during the measurement is normally below $\Delta m/m < 0.1\%$. The calibration measurement inaccuracy and the camera resolution result in an overall measurement error of about $\Delta\rho/\rho \approx 1.5\%$.

3.4 Viscosity measurements

The temperature dependent measurement of viscosity in liquids has a great tradition in literature [229, 230]. Many different methods have been developed throughout the decades, which are mostly carried out in contact with a crucible. The most common is rheology, where the liquid is sheared between two independently rotating crucibles and the resulting torque is detected [231]. Using different crucible shapes (e.g. cylinder, cone, plate etc.) different viscosity ranges can be accessed.

Since highly reactive melts are investigated in this work and the respective temperatures are rather high the contact-free oscillating droplet method is used in order to avoid any reactions of the melt with the crucible [82, 85, 232, 233].

Using a frequency generator that modulates the levitation voltage surface oscillation are induced on a levitating sample in the ESL. Here at first the sample's resonance frequency and a reasonable amplitude needs to be defined. After switching off the frequency generator the time dependent damping of the oscillation of the droplet is recorded by a high-speed camera. Using the image processing software TeVi the samples radius in x- and y-direction is analyzed and the damping can be determined [234]. According to reference [173] the time dependent sample radius $r_{x,y}$ is given by

$$r_{x,y}(t) = r_{0\ x,y} + A_{x,y} \sin\left(\omega_{x,y} t + \Phi_{x,y}\right) \exp\left(-\frac{t}{\tau_{x,y}}\right) \tag{3.14}$$

Here $r_{0\ x,y}$ is the mean sample radius, $A_{x,y}$ the amplitude of the oscillation in x- and y-direction with frequency $\omega_{x,y}$ and $\Phi_{x,y}$ is the phase shift. $\tau_{x,y}$ marks the relaxation time of the damping.

To determine the surface tension σ and the viscosity η the values of τ_x and τ_y and respectively σ_x and σ_y need to be averaged.

The surface tension σ is given by the mean oscillation frequency ω_n at mode n and the density ρ [235]:

$$\omega_n^2 = n(n-1)(n+2)\frac{\sigma}{\rho r_0^3}. \tag{3.15}$$

The mean relaxation time τ at mode n is correlated to the viscosity η:

$$\frac{1}{\tau_n} = (n-1)(2n+1)\frac{\eta}{\rho r_0^2}. \tag{3.16}$$

The applied frequency generator excites the sample in the ESL in the vertical direction (via the levitation voltage) equivalent to the mode $n = 2$, which gives:

$$\omega_2^2 = \frac{8\sigma}{\rho r_0^3} \tag{3.17}$$

and

$$\frac{1}{\tau_2} = \frac{5\eta}{\rho r_0^2} \tag{3.18}$$

These equations are valid if the the experimental setup fulfills the following conditions [236]: 1. only lamillar flow within the sample, 2. an force-free levitation, 3. a spherical sample shape. As shown in reference [237] all of this is valid for the small samples and the viscosity range accessed in electrostatic levitation.

The TeVi software was used to verify the correct resonance frequency. The oscillation can be disturbed if the sample is rotating [85]. If this is the case, the amplitude and frequency needs to be changed. To depict reliable viscosity values the difference in radii ratio should be less than 2 % ($\frac{r_{0\ x}}{r_{0\ y}} < 1.02$) (spherical sample), one oscillation mode should be applied and the amplitude of the oscillation should be five times larger than the random noise [233].

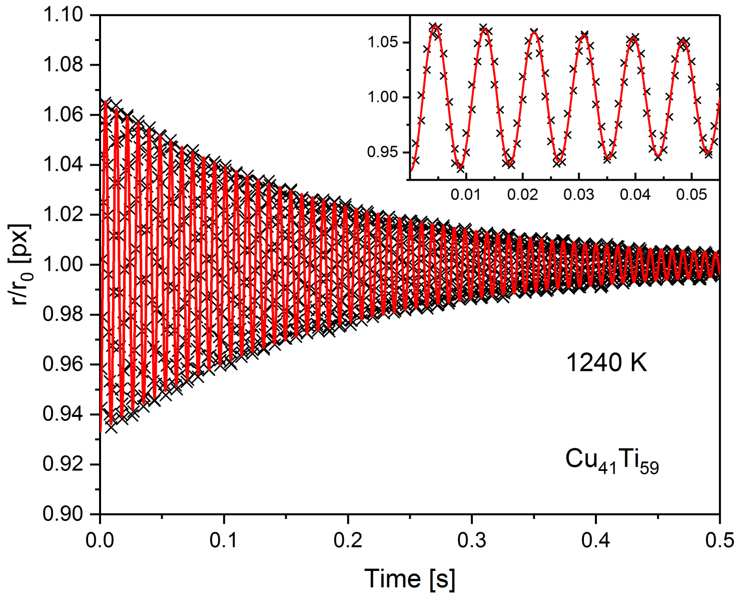

Figure 3.13: Damped oscillations of a $Cu_{41}Ti_{59}$ alloy at 1240 K as ivestigated in electrostatic levitation (ESL). The insert shows an detailed view of the change in sample radius in the time range between 0 and 0.05 seconds.

3.5 Sample preparation

The raw materials were cut and weighted in a lab scale with an accuracy of ±0.1 wt.%. Alloying took place in an arc melting device under inert gas atmosphere. The working chamber was evacuated to 10^{-7} mbar and afterwards flooded with ultrahigh purity Ar-gas (6N, 99.9999 %). The arc is ignited between a Tungsten tip and a water cooled Cu-plate, on which the sample material is placed.

A Ti piece is melted prior ro melting of the samples in order to avoid contamination from residual gases (e.g. Oxygen, Nitrogen, Hydrogen etc.). Ti has an excellent gas-gettering ability (especially for oxidation) to purify the atmosphere [238]. This step is very important, since Ti is also one component of the investigated alloy systems in this work.

The weight loss during alloying is below 0.1 mg indicating no significant change in composition. The processed sample mass depends on the respective experiments and varies for viscosity and density measurements between 40 mg and 100 mg. For the scattering experiments (depending on the different interaction cross-sections and scattering techniques) the sample mass is between 150 mg and 700 mg, respectively.

4 Results

4.1 Self-diffusion in Mercury investigated with quasielastic neutron scattering

Diffusion in liquids describes transport of mass via (random) walk powered by the heat bath. It is a fundamental property with high importance to many aspects in physics and materials science. Examples are chemical reactions in liquid and solid states, solidification and crystal growth from melts, or permeation of gas trough membranes [7].

In the case of crystalline solids the diffusion mechanisms are well known, e.g.: via either interstitial, interstitialcy or vacancy mechanisms [7, 27–32]. In gases and liquids, such mechanisms are missing due to the disordered nature of the medium. Particularly for liquids, it is to large extend unclear which physical parameters or properties determine the motion and the activation energy of the mass transport [239].

Metallic liquids are composed of atoms which exhibit no internal degrees of freedom, making them relative simple systems for understanding the transport mechanism. Single component liquid metals can be taken as a closest analogy to a hard sphere model system, due to the short-range, repulsive nature of the metallic bonding. Thus, a number of models describing the mass transport in metallic liquids are based on a transport mechanism of random, uncorrelated binary collisions, similar to a (dense) gas, which end up in semi-empirical terms with thermodynamic parameters of the melt [33–38].

The experimental determination of diffusion coefficients of metallic melts is rather challenging, mainly hampered by convective effects [54]. Moreover, if the involved temperature is high, chemical reactions with container materials can induce additional artefacts [55]. Since decades, a lot of research efforts have been put in measuring and understanding the diffusion in liquid metals. This includes even several space missions, in order to achieve well defined, purely diffusive experimental conditions without convective effects [240]. However, the availability of reliable experimental data is still rather rare.

In this respect, liquid Mercury offers particular advantages because it melts already below ambient temperature ($T_m = 234.3$ K). Hence, the relevant temperature is rather low and can be easily achieved. Furthermore, Mercury is also chemically not very reactive. The large density of $13.5\,\mathrm{g/cm^3}$ of Mercury makes it interesting to investigate how the diffusion in liquids in general depends on atomic mass and packing [241]. In literature several data sets of self-diffusion exist for liquid Mercury. Hoffman [242], Meyer [243] and Brown et al. [244] used respectively slightly different capillary-based techniques; Nachtrieb et al. [245] obtained their data from a shear cell experiment [44]. Part of these experiments were performed employing in-situ techniques. Nevertheless, since in these experiments no stable density layering exist, the results may still be affected by convection resulting to systematic deviations.

4.1.1 Experimental

Inelastic neutron scattering experiments of liquid Mercury have been carried out previously, at ambient temperatures [246–248]. However, both studies were focused on incoherent inelastic scattering outside the hydrodynamic regime. Diffusion coefficients of $1.57 \times 10^{-9}\,\mathrm{m^2s^{-1}}$ and $1.43 \times 10^{-9}\,\mathrm{m^2s^{-1}}$ were derived indirectly only. In addition, neither data close to the melting point of Hg are available, nor was the temperature dependence of self-diffusion studied.

Incoherent quasielastic neutron scattering (QENS) measures diffusion steps on atomistic scale and pico- to nanosecond time scale. Thus, it allows reliable and precise in-situ observations of atomic transport processes on an absolute scale without the influence of convection [45]. Here, we present QENS measurements on Mercury, carried out at the multi-disc chopper time-of-flight spectrometer TOFTOF at the Heinz Maier-Leibnitz Zentrum (MLZ) at Garching [214]. The very low instrumental background combined with high neutron flux and the appropriate energy (time) resolution make TOFTOF the ideal instrument for an accurate study of the self-diffusion in liquid Mercury.

An incident neutron wavelength λ of 10 Å at a chopper-speed of 3000 rpm was used, giving an accessible wave-number range from $Q = 0.1$ Å^{-1} to $Q = 1.2$ Å^{-1} at zero energy transfer. This results in an instrumental energy resolution (fwhm) of 60 μeV [213]. At small Q-values well below 1.2 Å^{-1} the coherent contribution and the corresponding Rayleigh line appear as a flat background, which is associated with the thermal diffusivity in Mercury some two orders of magnitudes faster than the self-diffusion [50, 249]. Therefore, the QENS spectra at low Q are dominated by the incoherent scattering cross section of σ_{inc} = 6.6 barn [112].

However, the neutron absorption cross section σ_{abs} of Mercury is 2068.3 barn at $\lambda = 10$ Å [112]. Therefore, measurements were carried out in reflection geometry. As illustrated in Fig. 4.1, the angle between the flat sample cell and the incoming neutron beam was 37° to ensure the best compromise between measured sample area (of 8.5 cm^2) and detectable Q-space (of 0.1 to 1.2 Å^{-1}).

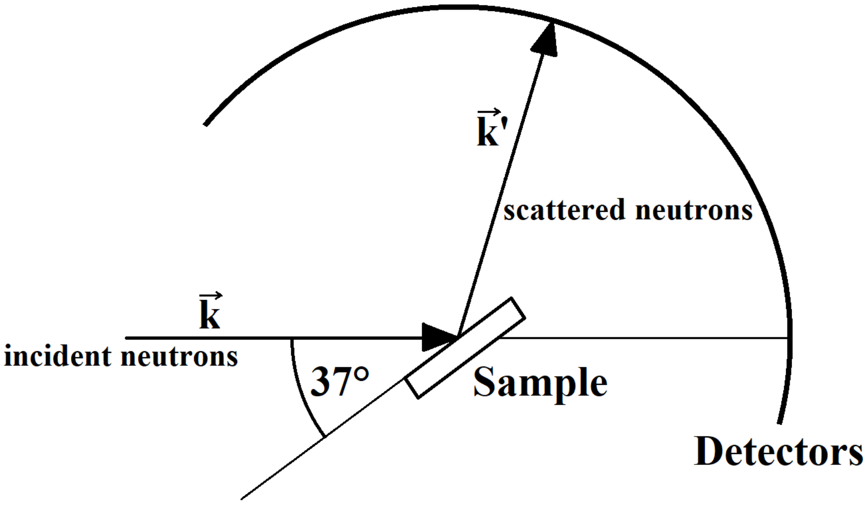

Figure 4.1: Schematic view of the assembly of the sample cell at TOFTOF to measure scattered neutrons in reflection geometry.

4.1.2 Sample holder

Fig. 4.2 shows an explosion sketch of the flat sample cell, which has been designed to carry out this experiment. It is made out of Polytetrafluorethylene (Teflon) to prevent any amalgamation at the relevant temperatures. It was designed to fit into a closed-cycle cryostat. In addition, it should last the Hg pressure difference within the vacuum atmosphere surrounding the sample holder. Fig. 4.3 shows the thermal analysis of the sample cell, showing a nearly isothermal distribution of the temperature. The heating was conduct by the mounting stick. The sample cell was sealed with a 2 mm thick Niobium lid. The provided Hg sample surface was 50 mm x 28 mm (according to the inner geometry of the cryostat). A sample thickness of 4.5 mm was feasible. The scattering contribution of the sample holder was determined at every measurement temperature. Here the sample holder was filled with a Cadmium sheet, whose thickness was matched to the absorption strength of the Hg sample. A temperature sensor was placed on the sample holder to ensure a correct temperature recording.

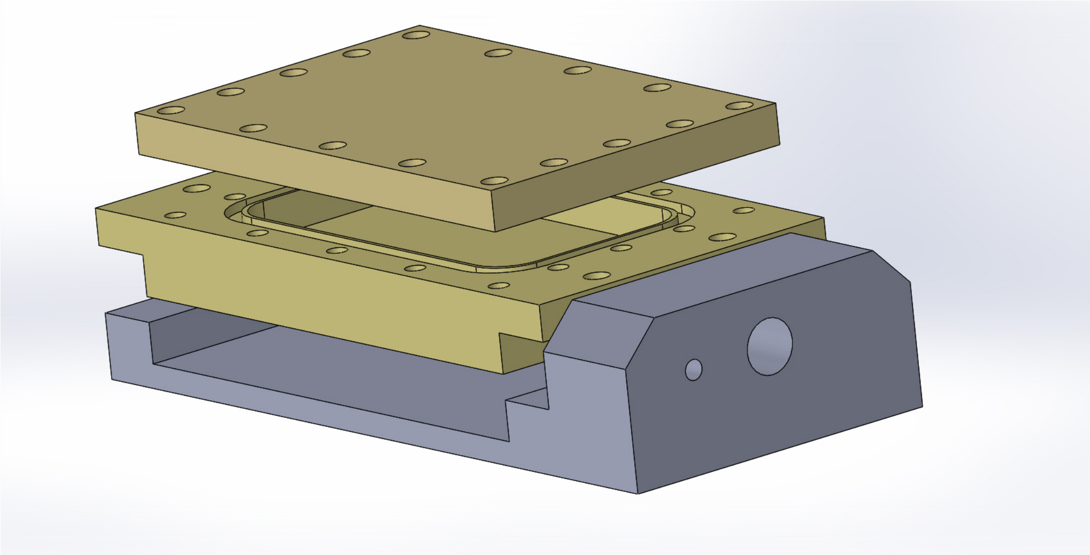

Figure 4.2: Explosion sketch of the constructed sample cell for the mercury measurement made out of Polytetrafluorethylene (Teflon) (brown). The mount (grey) is made out of Aluminum.

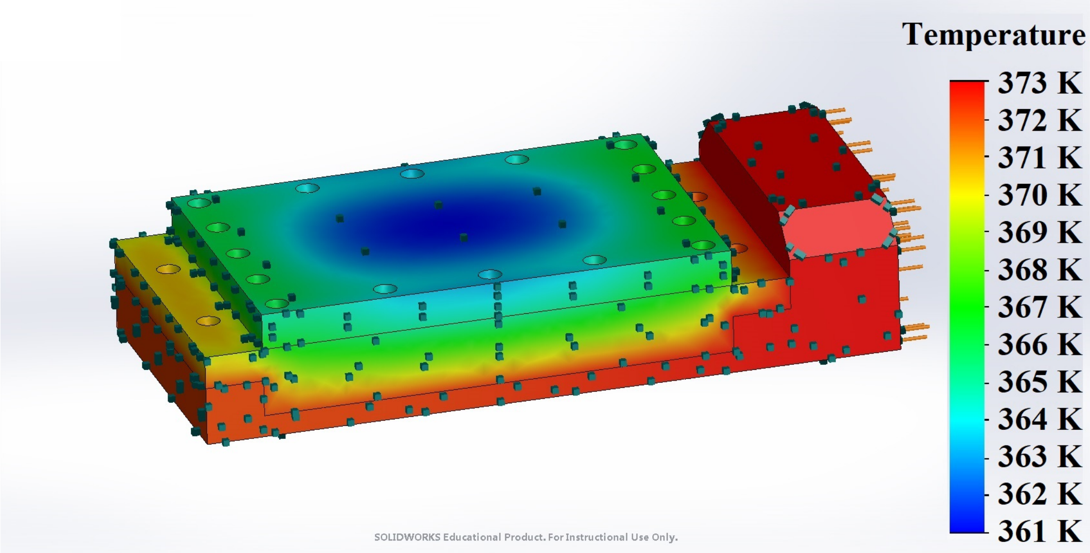
Temperature
373 K
372 K
371 K
370 K
369 K
368 K
367 K
366 K
365 K
364 K
363 K
362 K
361 K
SOLIDWORKS Educational Product. For Instructional Use Only.

Figure 4.3: Thermal analysis of the sample cell for the mercury measurement heated by the sample stick. In the sample position an isothermal temperature distribution is noticeable.

4.1.3 Data reduction

The QENS spectra presented here were obtained at a temperature range from 240 K to 350 K. The total detector counts varied less than 1 % during each isothermal hold, indicating no noticeable changes in the scattering strength. Since the mass remained unchanged during the measurement it can be deduced that no evaporation occurred. The collected intensities as a function of angle and flight time were normalized to a vanadium standard measured at room temperature. The data reduction and the derivation of the dynamic structure factor $S(Q,\omega)$ were done using the FRIDA [216] software package, including a subtraction of the empty cell contribution, angular correction for self- and container absorption, converting from the neutron time-of-flight to energy transfer, and an interpolation to constant momentum transfers Q.

Assuming a random walk motion, $S(Q,\omega)$ was fitted with a single Lorentzian function

$$L(Q,\omega) = \frac{1}{\pi}\frac{\Gamma(Q)}{\Gamma(Q)^2 + (\hbar\omega)^2}, \tag{4.1}$$

convoluted with the instrumental resolution $R(Q,\omega)$ as

$$S(Q,\omega) = bg(Q) + R(Q,\omega) \circledast (A(Q)L(Q,\omega)), \tag{4.2}$$

where $\Gamma(Q)$ is the half-width at half-maximum (HWHM), $bg(Q)$ is a slightly Q-dependent background and $A(Q)$ is the quasielastic intensity.

In Fig. 4.4 the dynamic structure factors $S(Q,\omega)$ at the two temperatures 240 K and 350 K and at a Q-value of 1 Å^{-1} are shown. For all investigated temperatures the quasielastic spectra are found to be distinctly broader than the instrumental resolution and they show a broadening for higher Q-values. The obtained $\Gamma(Q)$ of the Lorentzian line is depicted as a function of Q^2 in the insert of Fig. 4.4. It can be seen that in the low Q range, $\Gamma(Q)$ is proportional to Q^2, and its slope gives direct access to the self-diffusion coefficient via $D = \Gamma(Q)/\hbar Q^2$ [119].

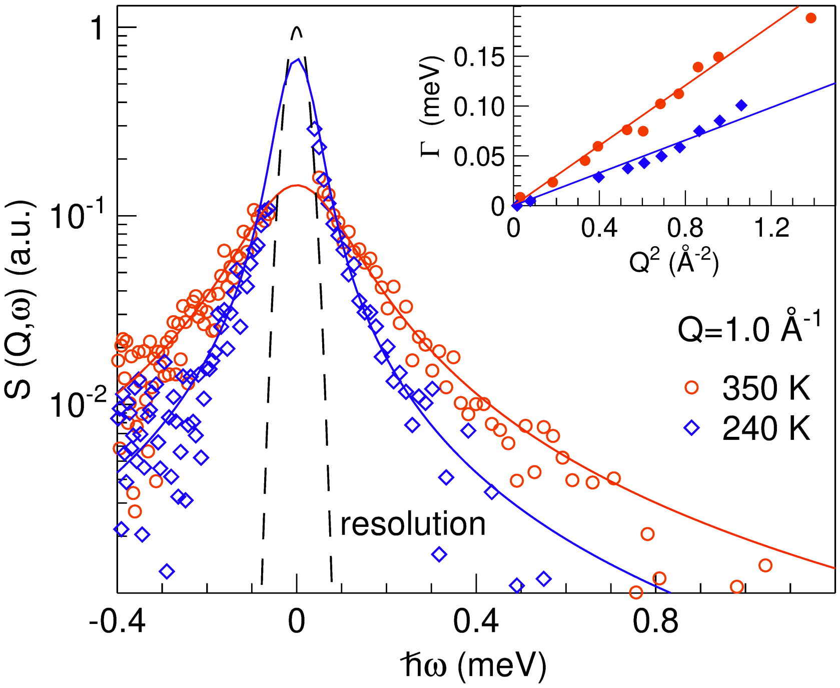

Figure 4.4: Dynamic structure factor $S(Q, \omega)$ of Hg at two temperatures 240 K (blue) and 350 K (red) and a Q-value of 1 $Å^{-1}$. The spectra are fitted with a Lorentzian function convoluted with the instrumental resolution function (black dashed line). In the insert the resulting HWHMs as a function of Q^2 are shown for both temperatures. Due to the reflection scattering geometry the elastic contribution is dominated by the Nb-lid of the sample cell and is excluded from the evaluation.

4.1.4 Results of QENS

The measured Mercury self-diffusion coefficients are shown in Fig. 4.5 as a function of temperature. The data obtained using QENS are compared to those available in the literature. Considering systematic and statistical errors the uncertainty of the self-diffusion coefficients is of about 4 % to 6 %. The temperature dependence of the self-diffusion coefficients can be described by an Arrhenius relation

$$D = D_0 \exp(-\frac{E_A}{k_B T}), \tag{4.3}$$

where E_A is the activation energy and k_B the Boltzmann constant. The fitted Arrhenius relation as depicted in Fig. 4.5 gives an activation energy E_A of $41.8 \pm 1.4\,\mathrm{meV}$ and a pre-exponential factor D_0 of $9.2 \pm 0.5 \times 10^{-9}\,\mathrm{m}^2\mathrm{s}^{-1}$.

Comparing the self-diffusion data obtained in this work with the previous measurements, the self-diffusion coefficient determined by QENS agrees at best with the one reported by Hoffman et al., using a long capillary technique [242]. Other data sets, reported by Meyer et al. and by Brown and Tuck, both measured with a capillary technique, show a distinguishable offset of some 15 % [243, 244]. Diffusion data investigated with a shear cell by Nachtrieb and Petit show the largest deviation [245], i.e. about 25 % smaller.

The overall deviation between measurements done with macroscopic samples and by QENS is considerably smaller compared to the case of other metallic melts like Ni or Fe [54, 55]. There the difference in the obtained self-diffusion coefficients can be up to a few hundred percents. This can be attributed to various factors: the temperature is rather low, which allows both good temperature homogeneity and stability during the experiment to be achieved; the sample is quite inert and chemical reactions with container walls at these applied temperatures are negligible. This improved considerably the precision of the measurements compared to *post mortem* techniques as solidification might introduce additional artefacts.

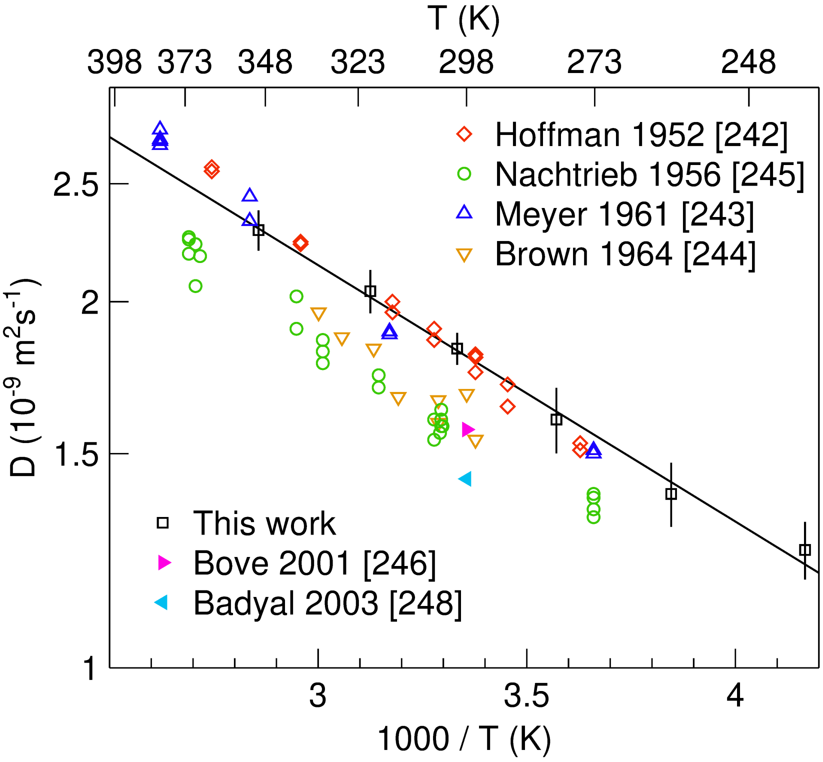

Figure 4.5: Self-diffusion coefficients of Mercury measured with QENS compared to previous measurements available in the literature [242–246, 248] as a function of inverse temperature.

4.1.5 Semi-empirical diffusion theory of binary collisions

The recent semi-empirical model for describing the self-diffusion coefficient of pure liquid metals based on an uncorrelated binary collision mechanism and Stokes-Einstein relation [35, 36] was developed by Kaptay [38]. Close to the liquidus temperature, it predicts the self-diffusion coefficient of the melt to be

$$D_m(T_m) = \text{const.}\frac{V_{m,M}^{\frac{1}{3}} T_m^{\frac{1}{2}}}{M_m^{\frac{1}{2}}}, \tag{4.4}$$

where $V_{m,M}$ is the molar volume, T_m is the melting point, and M_m is the molar mass. The packing fraction of the liquid is assumed to be 0.45, and the deviation from a hard-sphere like liquid can be captured by an effective radius [36, 38]. The activation energy close to the melting point is predicted to be proportional to the melting temperature

$$E_A = Bk_B T_m, \tag{4.5}$$

assuming that the vibration energy of the atoms is similar between the crystalline solid and the liquid close to the melting point, originally proposed by Andrade [250] according to Lindeman's law [251]. Here, B is a constant factor and k_B the Boltzmann constant.

Fig. 4.6 shows the self-diffusion coefficients of a number of pure metals and water at their respective melting point according to the scaling law equation 4.4, as a function $V_{m,M}^{\frac{1}{3}} T_m^{\frac{1}{2}} M_m^{-\frac{1}{2}}$. Only diffusion measured by QENS are used, for Ge [56], Al [51, 53], alkali metals [52], Cu [54], Ni [57], Fe [55], and water [252]. The resulting constant of equation 4.4 is found to be $1.06 \pm 0.11 \times 10^{-9}\,\mathrm{m\,kg^{1/2}s^{-1}K^{-1/2}mol^{-1/6}}$. It is as well depicted in Fig. 4.6 and describes both the self-diffusion coefficients of the Hg and alkali metals at their melting point. The original Kapty model proposes a value of $1.04 \pm 0.41 \times 10^{-9}\,\mathrm{m\,kg^{1/2}s^{-1}K^{-1/2}mol^{-1/6}}$ for normal metals, which coincides with the value obtained here within the uncertainty.

Close to unity this scaling constant shows that the assumed hard-sphere radius using a packing fraction of 0.45 can indeed describe the dynamics of the melt close to the melting point. In the case of Mercury, the hard sphere radius is of about 1.37 Å. Similar behaviour can be observed for the melts of the alkali metals, where the derived scaling constant is very similar, as one can see by the fit in Fig. 4.6.

In contrast, water or Germanium exhibit considerable deviation in diffusivity, which are up to a factor of 4 from the prediction of equation 4.4. It has been already realised by

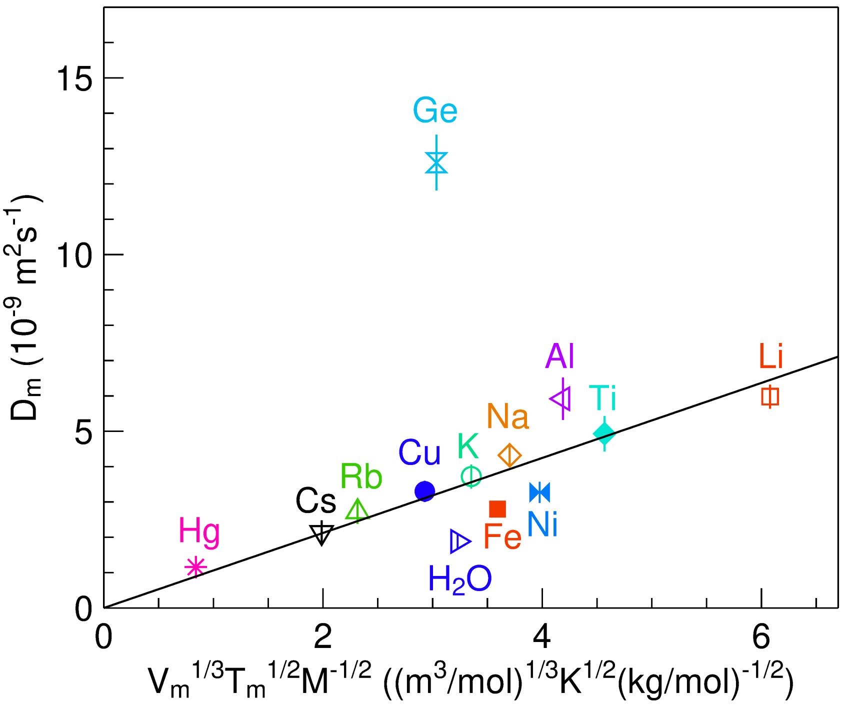

Figure 4.6: Self-diffusion coefficients of pure metals and water at their respective melting points [51–57, 252] as a function of $V_{m,M}^{\frac{1}{3}}T_m^{\frac{1}{2}}M_m^{-\frac{1}{2}}$. The line is a linear fit to the values according to equation 4.4.

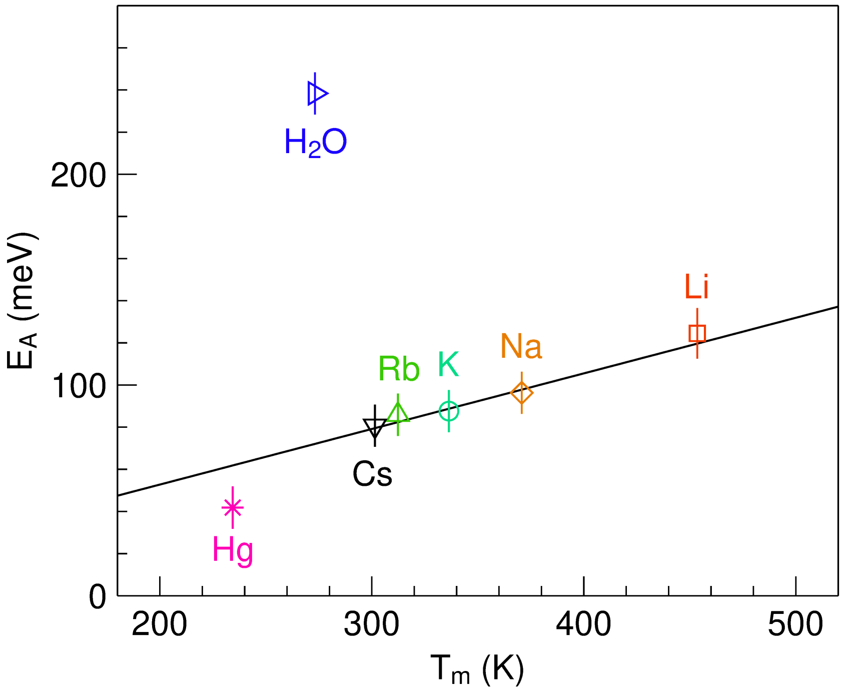

Figure 4.7: Activation energy of self-diffusion for pure alkali metals, Mercury and water as a function of the the melting temperature. The line is a linear fit to the values for the alkali metals according to equation 4.5 with $B = 3.11$.

Kaptay that non-metallic melts require a different constant of proportionality [38]. Also, the self-diffusion coefficient of Al, or that of the transition metals like Fe and Ni cannot be described by the scaling behaviour of alkali metals.

In Fig. 4.7 the activation energy is depicted as a function of T_m in a temperature range between 200 K and 500 K. In this temperature range, out of the previously considered metals only the alkali metals and Mercury exhibit their melting point. The scattering of the activation energies of elements appears to be larger than the prediction of the diffusion coefficients at the melting point. In addition, the molecular structure of Water yields a higher activation energy than in metallic melts. For the activation energy the Kaptay model proposes a linear temperature dependence according to equation 4.5. For the alkali metals melts a constant B of 3.11±0.04 is obtained, indicated by the fit in Fig. 4.7. In the case of Hg this constant would predict the activation energy to be (62.8±0.8) meV, which is of about 50 % higher than the value obtained in the QENS measurement ($E_A(Hg) = 41.8 \pm 1.4\,\text{meV}$). Apart from the fact that non-metallic melts exhibit considerable deviations, here it seems that also Hg does not follow exactly the same diffusive behaviour of the alkali metals.

4.1.6 Relation between self-diffusion and viscosity

In all of the above mentioned models it is assumed that the Sutherland-Einstein or Stokes-Einstein relation holds [253, 254], where the viscosity is proportional to the inverse of the self-diffusion coefficient. It assumes a hydrodynamics radius r_{H}, which represents the size of the diffusing particle, by

$$r_{\mathrm{H}} = \frac{k_B T}{A * D\eta}, \tag{4.6}$$

where k_B is the Boltzmann constant, A is a factor marking different boundary conditions. $A = 6\pi$ refers to a stick boundary condition, corresponding to the Stokes-Einstein relation, whereas $A = 4\pi$ is derived from a slip boundary surface, known as Sutherland-Einstein relation.

Viscosity of Mercury is well studied, with data sets in good agreement with each other [255]. Kasama et al. reported the one covering the highest available temperature range investigated using a capillary technique [256]. The values are depicted in Fig. 4.8, showing a rather low overall measurement error. Using the viscosity data of Kasama et al., $D\eta$ is calculated and shown in Fig. 4.9. Here, the measured melt viscosity values are multiplied by the diffusion coefficients obtained in the current study. For the best linear fit according to equation 4.6 a hydrodynamic radius of 0.81 Å is obtained, assuming the Stokes-Einstein relation is valid, and of 1.21 Å, if using the Sutherland-Einstein relation, where in both cases the prediction is accurate within ∼20 %.

Atom radii in the liquid, even for single component metallic melts, are not as well defined when compared to those in crystalline materials due to the disordered nature of the structure. As shown above for both describing the self-diffusion close to the liquidus temperature and for the Sutherland-Einstein relation, the effective hard sphere radius of Hg is below 1.4 Å. For comparison, the ion radius of the oxidation state of Mercury Hg^{2+} is equal to 1.16 Å and the covalent radius is 1.44 Å [67]. The interatomic distance of Mercury can be derived from the radial distribution function, which is a Fourier transform of the structure factor. In Fig. 4.10 the radial distribution function derived from the liquid structure factor as seen by x-ray diffraction of Mercury is depicted at temperatures of 173 K, 273 K and 473 K [257]. The observed interatomic distance is of about 3.07 Å ($r \approx 1.5$ Å). Thus, the repulsive part of the interatomic potential, which can be effectively mimicked by a hard-sphere system, plays a dominate role in the melt dynamics in the case of Mercury and alkali melts.

Among the substances which show a different proportionality, water and Germanium ex-

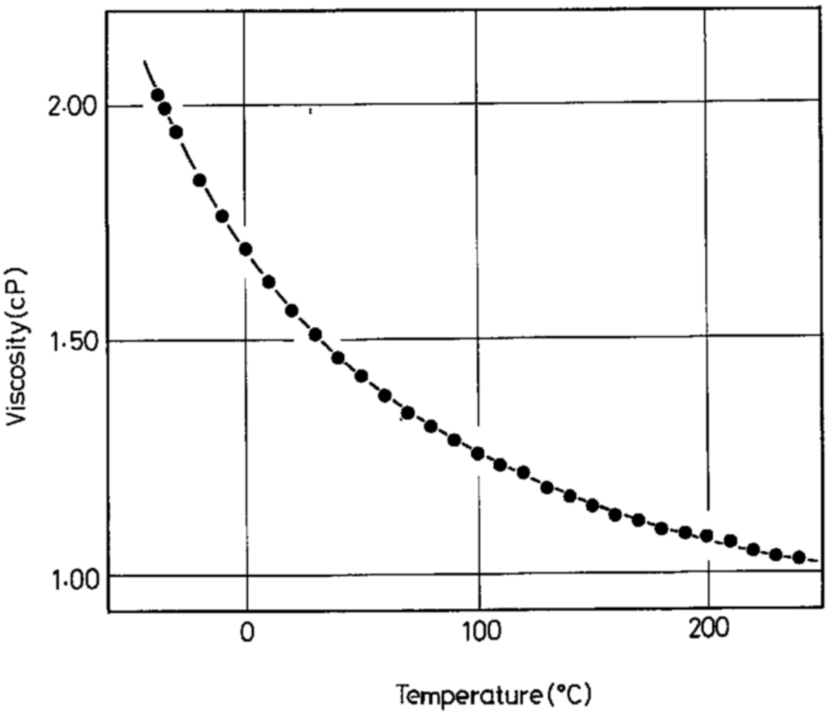

Figure 4.8: Temperature dependence of viscosity of Mercury. The measurement error is smaller than the size of the symbols and of about 0.2 %. Concrete values can be found in [256].

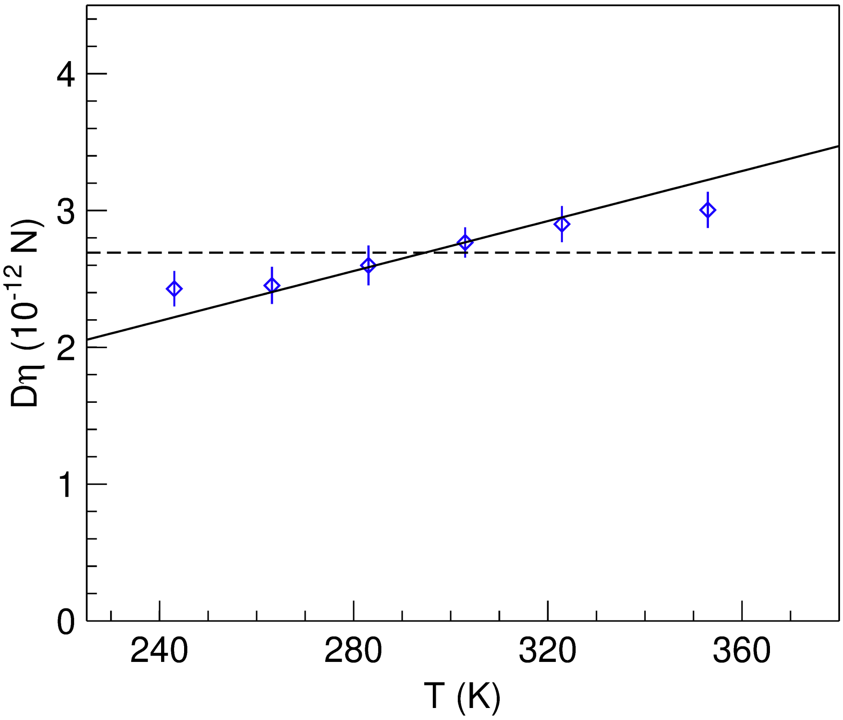

Figure 4.9: Temperature dependence of the diffusion-viscosity relation in Mercury when compared with the Stokes-(Sutherland-)Einstein relation (solid line). The dashed line would hold if $D\eta$ would be a temperature independent constant.

hibit a less-densely packed structure with a lower coordination number (e.g.: Germanium of 6.8 [258]) than Mercury, which has twelve nearest neighbors [257]. It is not surprising that different atomic packing or short-range order of the melt, also in the case of transition metals like Ni, will affect the effective hard-sphere radius. Although it is still possible to estimate the dynamics according to a hard-sphere like model, for these melts there appears to be no clear general trend how the proportionality or the effective radius are related to the properties of the melt, like ionic or covalent radii.

At higher packing fraction, like that in glass-forming metallic melts even the assumption of a transport mechanism of uncorrelated binary collisions may not be valid anymore. Here, instead of the Stokes-Einstein relation, $D\eta$ is observed to be constant [259]. Concerning the temperature dependence, for e.g.: Ni self-diffusion, a T^2 temperature dependence expected from a binary collision mechanism is not observed [57]. Here for Hg it can be seen that the deviation from the prediction of the Sutherland-Einstein increase for the smallest and highest measured temperatures. Potential deviations below 240 K and above 350 K may be expected. This is likely one of the origins why the temperature dependence of the self-diffusion is less well predicted as compared to that in the alkali melts. However, a $D\eta =$ constant, similar to the case of dense (glass-forming) metallic melt is not observed in the investigated temperature range either.

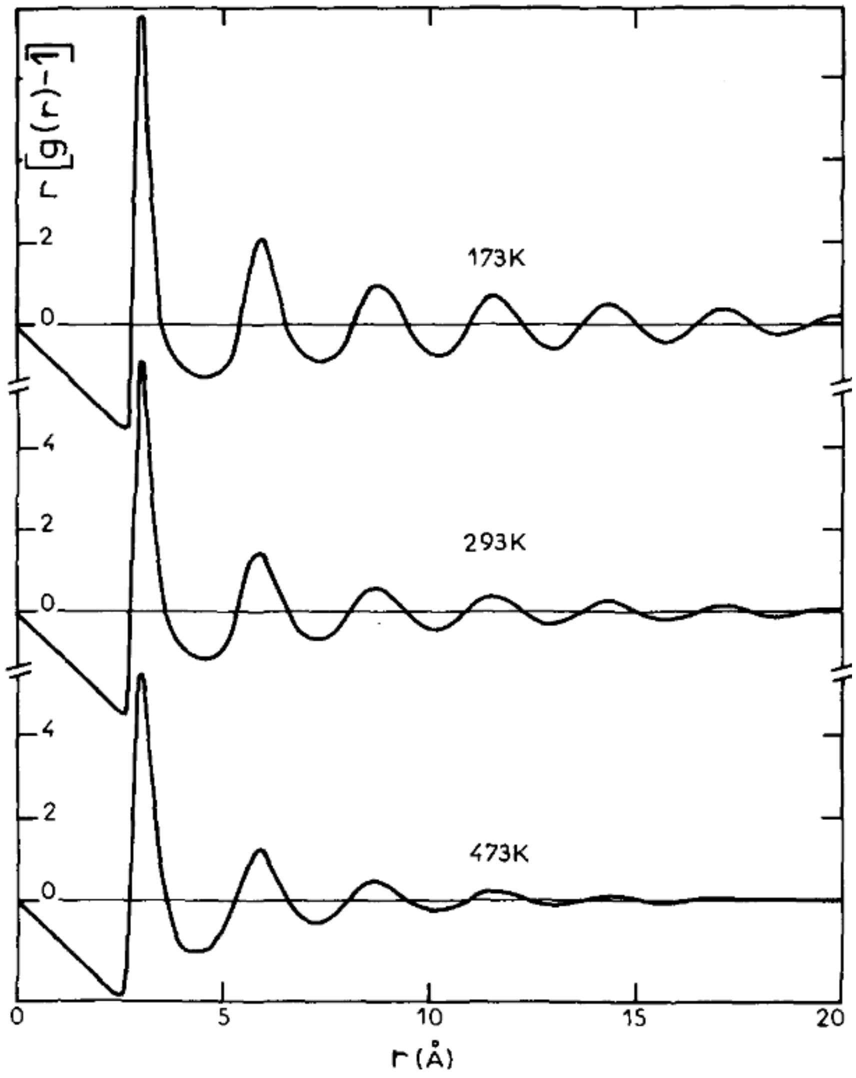

Figure 4.10: Radial distribution function of Mercury at temperatures of 173 K, 293 K, and 473 K; obtained from the Fourier transformed liquid structure factor investigated with x-ray diffraction [257].

4.1.7 Conclusion

In conclusion, we were able to measure the self-diffusion coefficients in liquid Mercury with quasielastic neutron scattering. Our results are in line with the predicted values of the diffusivity at the melting point with a semi-empirical approach for liquid diffusion based on a hard-sphere like model. Close to the melting point, liquid Mercury exhibits similar diffusive dynamics like these of the alkali metals, which can be described by an effective radius close to its covalent radius, indicating a dominant contribution of the repulsive part of the interatomic potential. However, the temperature dependence is less well predicted, where also deviations from the Sutherland-Einstein relation are found over a large temperature range.

4.2 Short-range order in binary Zr-Ti melts

In the periodic table in the early transition metal group 4 the element Zirconium (with atomic number 40) is placed directly under the element Titanium (with atomic number 22). Since they share the same orbital configuration, both elements show by nature similar chemical and structural properties. For example, both - Titanium and Zirconium - exhibit in the solid a phase transition from an α-hcp to a β-bcc phase with similar transition temperatures; $T_{trans,Ti} = 1155$ K in case of Titanium and $T_{trans,Zr} = 1136$ K for Zirconium, respectively. In addition, the difference in atomic radii and the overall mixing enthalpy are rather small. Titanium exhibits atomic radii of $r_{Ti} = 1.47$ Å and Zirconium respectively $r_{Zr} = 1.60$ Å [67], which yields a ratio of 0.92.

Alloyed they compose in a completely miscible system. In Fig. 4.11 the phase diagram of the Zr-Ti system is depicted, where the absence of any inter-metallic phases is noticeable. Only the α to β phase transition and the solid-liquid transition are observed in the shown temperature range.

In case of pure Titanium and Zirconium the difference in self-diffusivity is of several orders of magnitude between the α-hcp (10^{-18}-10^{-21} m^{2}s^{-1}) to β-bcc (10^{-12} m^{2}s^{-1}) phases. This was reported as the anomalous self-diffusion in β-bcc phases [260–262], which comprises additionally the aspect of a curved temperature dependence of the self-diffusivity in the Arrhenius plotting due to certain strongly temperature dependent phonons (co called "phonon assisted diffusion"). The respective self-diffusion coefficients are shown in Fig. 4.12. It is clearly apparent how large the impact of a changed short-range (structure) and phonon spectra on the atomic transport properties in crystalline solids can be, where the diffusion mechanism is strongly coupled to the structure via either interstitial, interstitialcy or vacancy jumps. Quasielastic and inelastic neutron scattering experiments using a backscattering spectrometer showed, that the reason for the anomalous fast self-diffusion in β-bcc Ti is due to a simple 1/2 [111] nearest-neighbor vacancy jump [27]. The other shown self-diffusion coefficients of α-Ti [263], α-Zr [264] and β-Zr [265] were obtained by tracer diffusion measurements, respectively. In addition, the self-diffusion coefficients of liquid Titanium are depicted [198], which are QENS-measurements carried out in electromagnetic levitation at TOFTOF. It can be seen, that the self-diffusion coefficients in the liquid are as well orders of magnitudes larger (10^{-9} m^{2}s^{-1}) than those in the crystalline solid β-bcc (10^{-12} m^{2}s^{-1}) phase due to the different diffusion mechanism in liquids. This topic was comprehensively discussed in the previous section of this work.

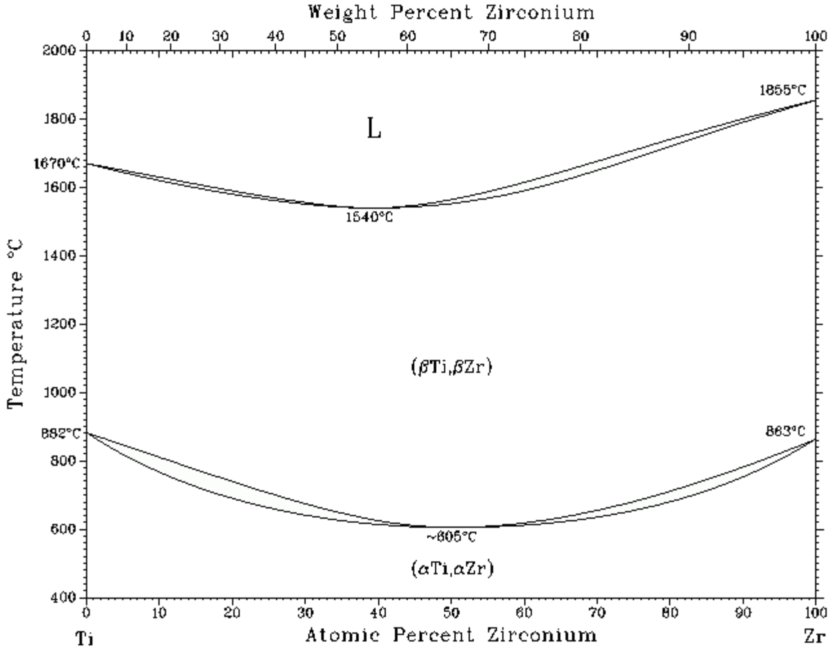

Figure 4.11: The phase diagram of the Zr-Ti system [266]. The left side refers to pure Titanium and the right side to pure Zirconium.

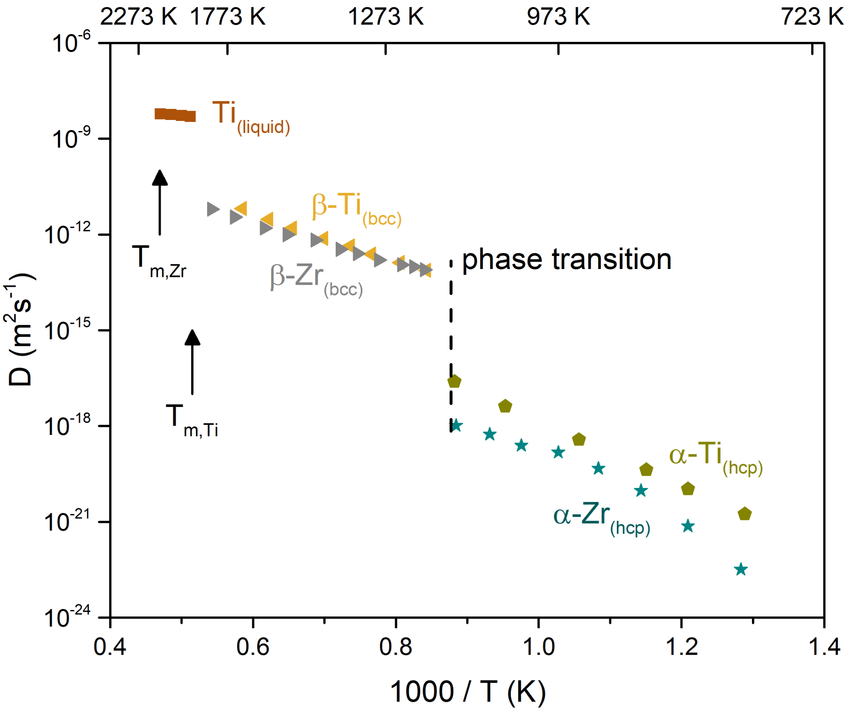

Figure 4.12: Comparison of self-diffusion coefficient in different phases of Zirconium and Titanium. All shown data can be found in literature: Liquid Ti [198], α-Ti [263], β-Ti [27], α-Zr [264], β-Zr [265].

Zr-Ti alloys are binary boundary systems of ternary Zr-Ti-Ni alloys forming stable quasicrystals [187, 267–269]. In addition, the Zr-Ti system is used as a basis for many bulk metallic glass-forming (BMG) alloys (e.g. Zr-Ti-Cu, Zr-Ti-Al, Zr-Ti-Nb, Zr-Ti-Cu-Ni, Zr-Ti-Cu-Ni-Be, ...). However, the detailed formation mechanisms of these special structures remain largely unknown and are often speculative. Here, accurate knowledge of melt properties such as the diffusivity and the melt structure is essential. For a comprehensive understanding of those multi-component systems it is first necessary to investigate the pure compounds and the binary boundary systems. In liquid Zirconium and Titanium structural investigations using neutron diffraction were carried out [65, 66]. In melts of both elements an icosahedral short-range order was found.

In the following the short-range order and atomic dynamics in binary Zr-Ti are discussed. Therefore neutron diffraction and quasielastic neutron scattering experiments were carried out. Melts were processed at the large scale facilities in electromagnetic levitation. Here, the evaporation (predominantly of Ti) under ultra-high vacuum at the elevated temperatures makes electrostatic levitation inapplicable for the rather long respective measurement times. However, complementary X-ray diffraction experiments using synchrotron radiation were possible to be executed in electrostatic levitation, because this kind of experiments typically run way faster (within seconds) than neutron scattering experiments (hours time scale).

4.2.1 Neutron diffraction of zero scattering composition

In a neutron diffraction experiment Titanium is one of the five elements owning a negative coherent scattering length of $b_{coh}(Ti) = -3.438$ fm [112]. In contrast, Zirconium has a coherent scattering length of $b_{coh}(Zr) = 7.16$ fm. Hence, in the binary alloy with the composition $Zr_{32.4}Ti_{67.6}$ the mean scattering length is zero. As described in the chapter on the structural analysis of binary alloys (section 2.2.7), the partial contribution of the partial structure factors S_{NN} and S_{NC}, that describes the topological short-range order and respectively the correlation of particle density and chemical composition, vanish for this alloy composition in Bathia-Thornton's formalism (see equation 2.51). A neutron diffraction experiment then measures directly the partial structure factor S_{CC} that describes the chemical short-range order.

Neutron diffraction experiments on $Zr_{32.4}Ti_{67.6}$ and Zr_2Ti melts processed in electromagnetic levitation were carried out at the high intensity 2-axis diffractometer D20 at the Institute-Laue-Langevin (ILL) in Grenoble, France. The data reduction routine is described in the section 3.2.2.

In Fig. 4.13 the measured total structure factors $S(Q)$ at a temperature of 1420 K are depicted. Here, the green points are the total structure factor $S(Q)$ of Zr_2Ti. The red points refer to the measured S_{CC} of $Zr_{32.4}Ti_{67.6}$. In this measurements initially some Copper Bragg peaks occurred, which emerge from secondary scattered neutron at the levitation coil and couldn't be corrected by the underground measurements. However, since they can be identified and clearly do not result from the sample, the receptive values have been cut out of the structure factor. Else than this the depicted S_{CC} of $Zr_{32.4}Ti_{67.6}$ is almost flat. This indicates that essentially no chemical short-range order is observed in this alloy and the liquid structure is mainly determined by topological ordering. In contrast, the measured liquid structure factor of Zr_2Ti shows a maximum at $Q = 2.47$ Å^{-1} and a second and third maxima, respectively.

Fig. 4.14 compares the measured S_{CC} of $Zr_{32.4}Ti_{67.6}$ as seen by neutron diffraction at 1420 K with the total $S(Q)$ of the same binary composition measured in diffraction using X-rays from synchrotron radiation. Due to the different scattering contrast characteristics of the respective elements in an X-ray experiment another total structure factor $S(Q)$ is observed. However, the liquid structure of $Zr_{32.4}Ti_{67.6}$ is mainly determined by topological ordering as seen by the flat S_{CC}. The total $S(Q)$ measured with X-rays shows a maximum at $Q = 2.55$ Å^{-1}. To compare this measurement to other Zr-Ti alloys, for instance Zr_2Ti, complementary diffraction experiments with X-rays are required.

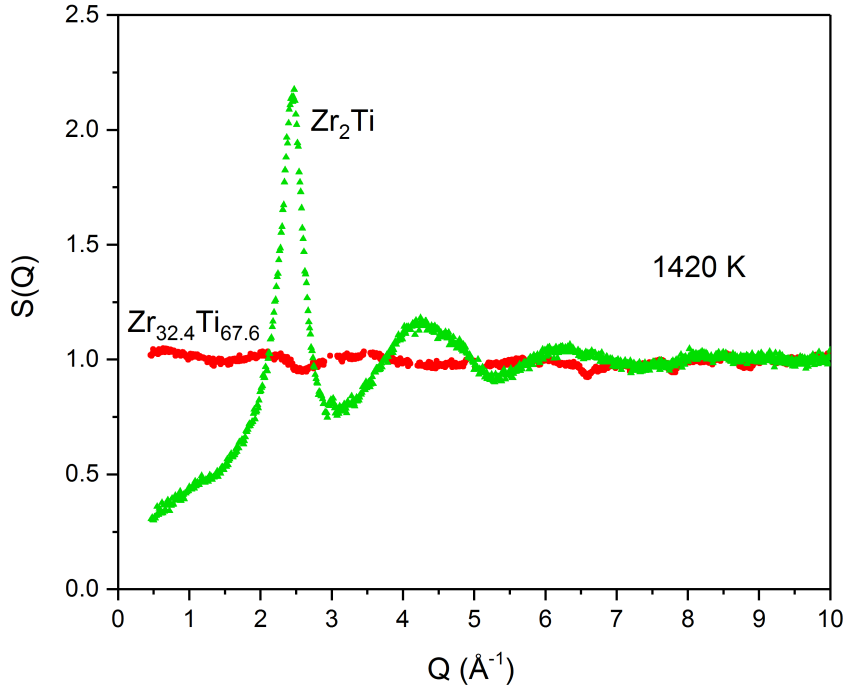

Figure 4.13: The liquid structure factor of melts of the zero scattering $Zr_{32.4}Ti_{67.6}$ composition (red) and Zr_2Ti composition (green) at a temperature of 1420 K investigated using neutron diffraction and processed by electromagnetic levitation.

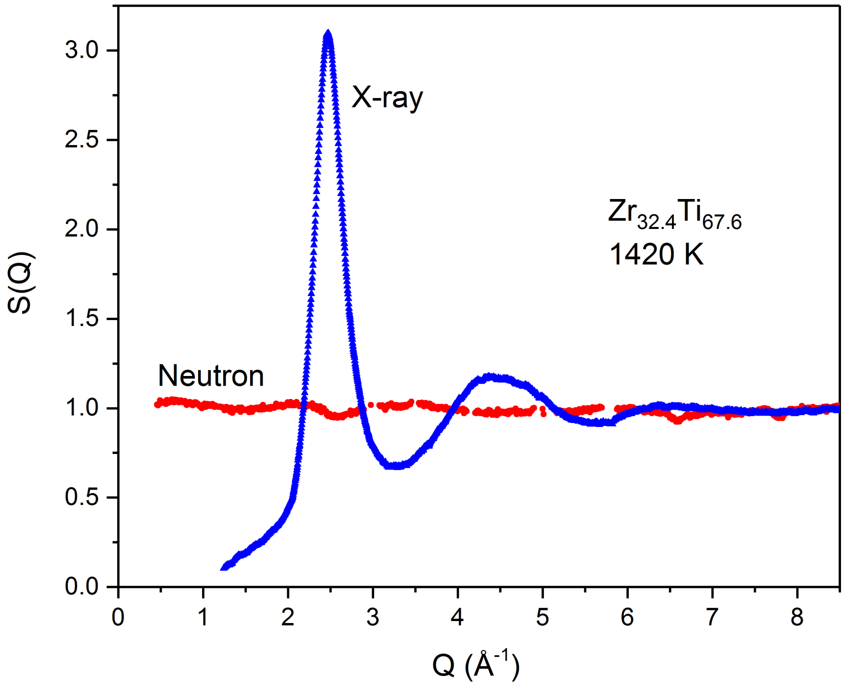

Figure 4.14: Comparison of the liquid structure factor of zero scattering $Zr_{32.4}Ti_{67.6}$ melt as seen by neutron diffraction (red) and x-ray diffraction (blue).

4.2.2 X-ray diffraction using synchrotron radiation

X-ray diffraction experiments on the binary Zr-Ti melts with composition $Zr_{15}Ti_{85}$, $Zr_{32.4}Ti_{67.6}$, $Zr_{50}Ti_{50}$ and Zr_2Ti were carried out at the materials science beamline ID11 at the European Synchrotron Radiation Facility (ESRF) in Grenoble, France. The melts were processed by electrostatic levitation.

Fig. 4.15 depicts the collected total structure factors $S(Q)$. For clarity, the curves are shifted in the vertical direction. The structure factors of the pure elements Titanium [66] and Zirconium [65] are also shown, which were processed by electromagnetic levitation and measured by neutron diffraction. All depicted structure factors were measured at a temperature of 1900 K.

The position of the structure factor maxima shifts with the Ti-concentration from Q = 2.42 Å^{-1} for "0 % Ti" in case of the pure Zirconium towards Q = 2.62 Å^{-1} for 100 % Titanium. Since the shape of the structure factor remain constant the topological structure does not change significantly. This reflects a variation of the atomic distances due to the different atomic radii of the elements. For instance, the Goldschmidt radius of Titanium is $r_{Ti} = 1.47$ Å and respectively of Zirconium $r_{Zr} = 1.60$ Å[67]. When combining both elements in binary mixtures a different atomic packing is possible. In consequence this can result (in theory) also in a variable molar volume whereas the structure (e.g. the coordination number) remains unchanged. Correspondent investigations are discussed in the next subsection.

The effect of different atomic radii can be suppress when the measured total structure factor is normalized over the position of the first maximum, what is shown in Fig. 4.16. Here, all measured Zr-Ti total x-ray structure factors $S(Q)$ essentially look the same and appear in a similar shape than the structure of the pure liquid elements Zr and Ti. Small aberration are distinguishable at the intensity of the third and slightly the second maxima, respectively. This might be due to different applied scattering techniques (neutrons instead of x-rays). In case of the pure liquid metals S_{NN} is measured. For the binary alloys only the total $S(Q)$ is available and the other partial structure factors are (except the zero scattering alloy) not known. However, the particular characteristics and the position of the shoulder in the second maxima appears to be very similar for all investigated samples.

For a specific distinction of the melt structure the measured structure factor can be compared with a simulation of different arrangements of nearest neighbors (e.g. icosahedron,

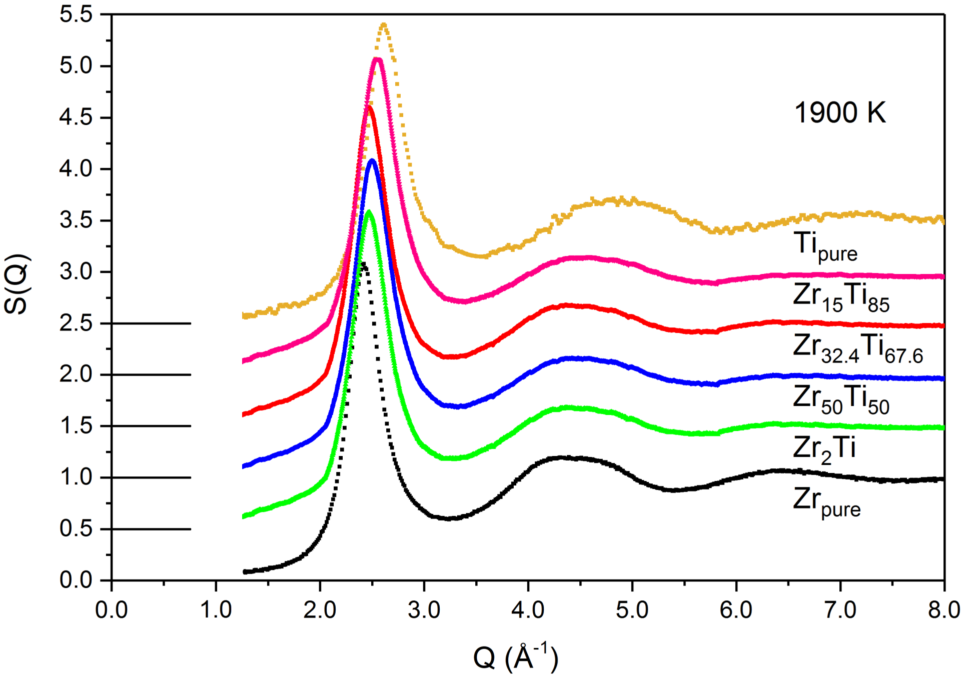

Figure 4.15: Comparison of the total structure factors of binary Zr-Ti melts with composition $Zr_{15}Ti_{85}$ (violet), $Zr_{32.4}Ti_{67.6}$ (red), $Zr_{50}Ti_{50}$ (blue) and Zr_2Ti (green), investigated using x-ray diffraction and compared to the liquid structure factors of pure Titanium (orange) [66] and pure Zirconium (black) [65] at $T = 1900$ K.

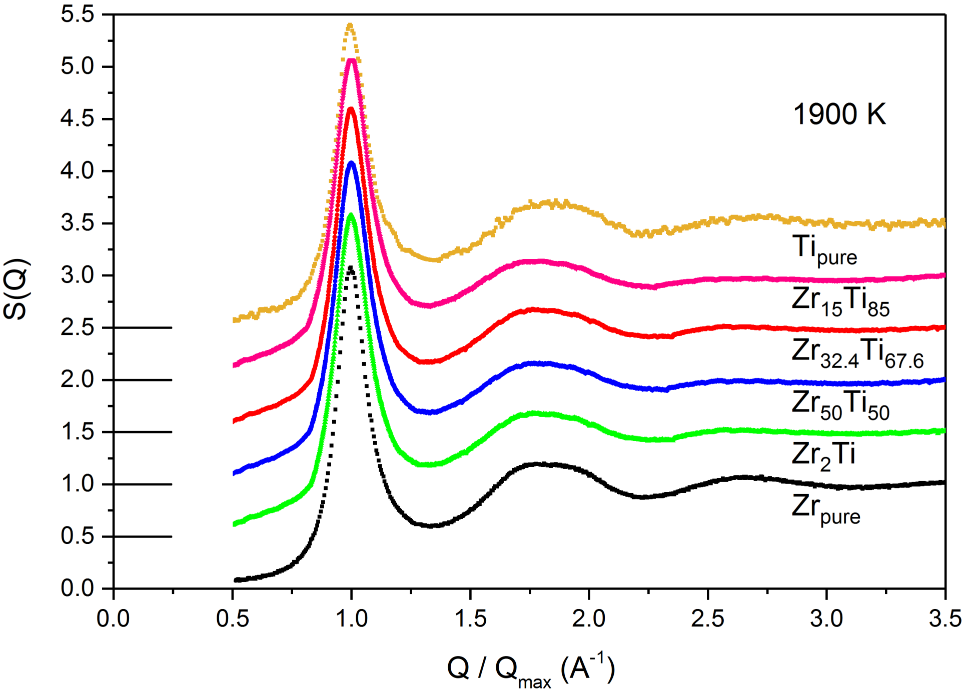

Figure 4.16: Comparison of the total x-ray structure factor of melts with different Zr-Ti compositions normalized over the structure factor maximum at $T = 1900$ K.

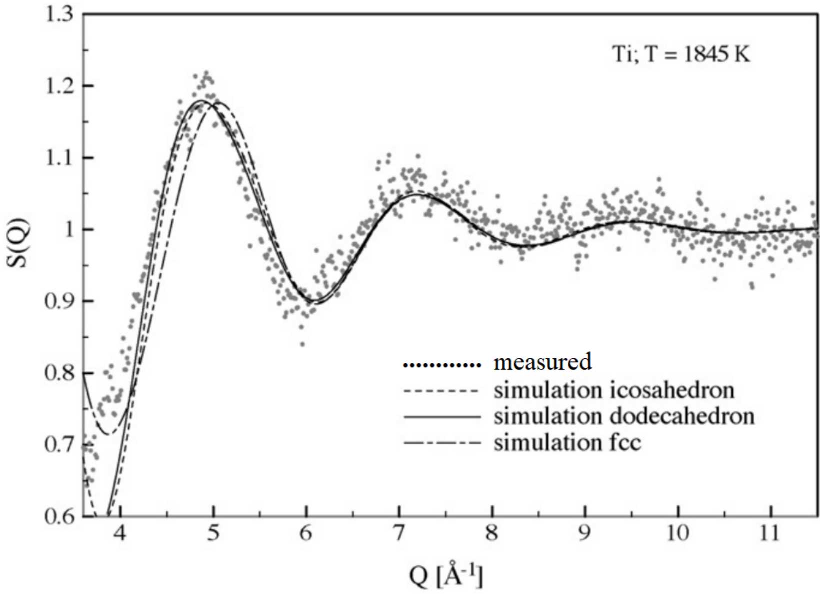

Figure 4.17: Fit of the liquid structure factor of raw Titanium at $T = 1845$ K assuming different short-range structures of icosahedral, dodecahedral or fcc type [66]. The short-range order of the measured melt is best described by an icosahedral one.

dodecahedron, fcc, etc.) [270]. This is already achieved for the pure elements Titanium and Zirconium. For both pure elements icosahedral short-range order prevails in the melt. In Fig. 4.17 the resulting structure factor of such simulated short-range orders are depicted and compared to a measurement of the structure factor of pure Titanium. The measured signal is best described assuming the short-range order to be of icosahedral type.

Referring back to Fig. 4.16 the structure factor measured for Zr-Ti melts are very similar to those of the pure elements. This leads to the conclusion, that also in those kind of melts the topological short-range order is formed by icosahedra. In addition, due to the similarity of all measured Zr-Ti melt structures the indication of an absent chemical short-range order in $Zr_{32.4}Ti_{67.6}$ is assumed for the other binary Zr-Ti melts. Following the liquid Zr-Ti system only shows topological ordering. However, nothing is known about the particular S_{NC}.

4.2.3 Density measurement and calculation of the molar volume

The densities of Titanium and Zirconium - in the solid and in the liquid phase - are rather different. This is not only due to the difference in atomic radii, but also due to the respective molar masses, which are $M(Ti) = 47.867$ g/mol for Titanium and $M(Zr) = 91.224$ g/mol.

Therefore, at ambient temperatures solid hexagonal α-Titanium has a density of $\rho_{hcp,Ti} = 4.506$ g/cm^{-3} [271] and α-Zirconium $\rho_{hcp,Zr} = 6.501$ g/cm^{-3} [272]. However, the values at other temperatures depend on the thermal volume expansion:

$$\frac{V(T) - V_0}{V_0} = \alpha_V \Delta T \tag{4.7}$$

Here V is the volume, ΔT the temperature difference and α_V the volume expansion coefficient.

In the liquid state the disordered structure leads to a looser packing of atoms and therefore lower densities. Recently, melt densities of various Zr-Ti compositions measured in electrostatic levitation were reported [273]. The results are shown in Fig. 4.18.

In all investigated compositions, the observed thermal expansion appears to be very similar. The averaged volume expansion coefficient is $\alpha_V = 4.60 \pm 0.15\ 10^{-5}$ K^{-1} at temperature of $T = 1850$ K (at this temperature in all investigated alloys measured data exists).

However, the melt density ρ still reflects the varying molar mass M. To reduce the density to the packing only, the molar volume V_m is determined, which can be calculated following the equation:

$$V_m = \frac{M}{\rho} \tag{4.8}$$

For $T = 1850$ K the molar volume of all investigated Zr-Ti melts and the pure elements is depicted in Fig. 4.19. V_m is plotted as a function of Titanium concentration, where the dotted line refers to an ideal mixture. The color code accords to the previous plotting of the structure factors and not to the reference data of the density.

The molar volume shows a linear concentration dependency for Zr-Ti melts, which also comply with the pure Zirconium and Titanium. Here, the excess volume $(V_m - V_m^{ideal})$ is between 0.26 % and 0.87 % of V_m, what is below the uncertainty of the density measurement of ca. 1 %. The insert of Fig. 4.19 shows the respective overall packing fraction of

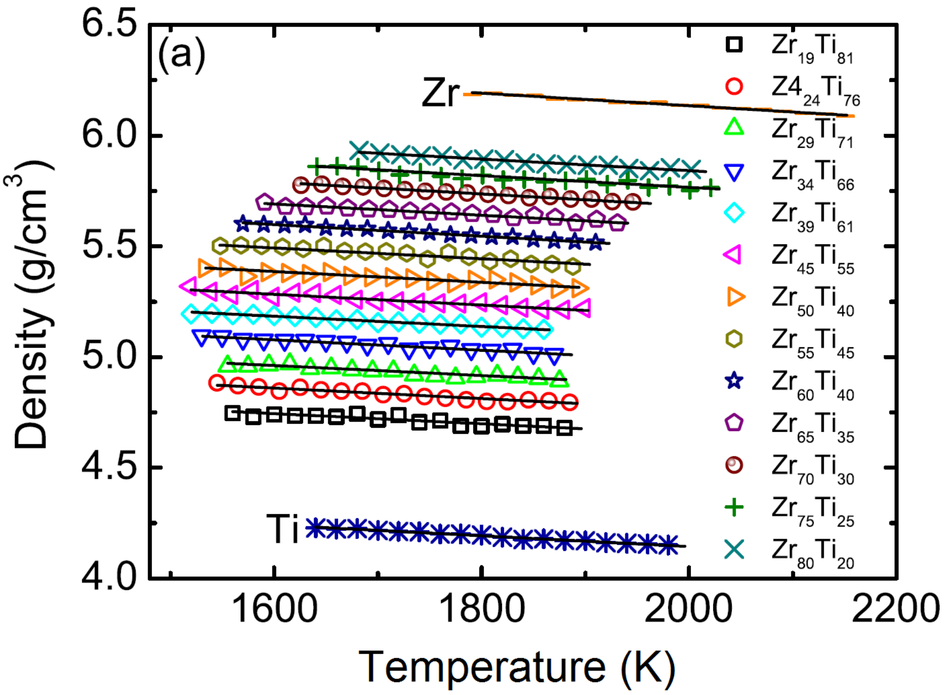

Figure 4.18: Concentration and temperature dependent density of Zr-Ti melts with various compositions measured in ESL [273]. The error is smaller than the size of the symbols.

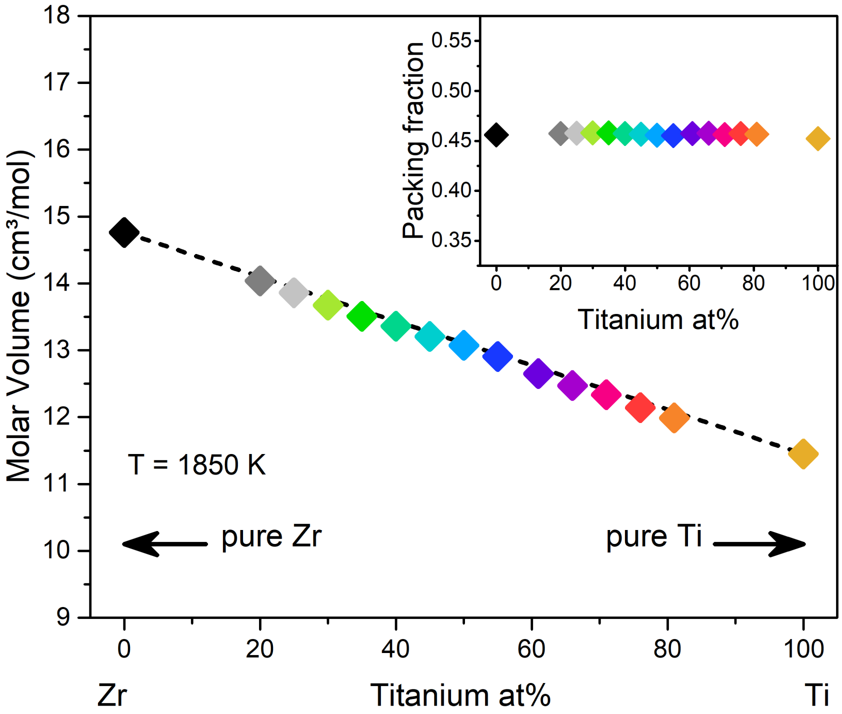

Figure 4.19: Concentration dependency of the molar volume and inserted respective packing fraction of Zr-Ti alloys as deduced from the density data at $T = 1850$ K. The color code is alike the other graphs in this work and unlike Fig. 4.18.

the investigated concentrations, which also remains in all measured concentrations similar at a value of 46 % using the Goldschmidt radii of $r_{Ti} = 1.47$ Å and $r_{Zr} = 1.60$ Å [67], indicating no significant concentration related changes. Following ideal mixing effects are observed, which cause a different packing other than the differences of the atomic radii.

4.2.4 Concentration-dependent atomic dynamics as seen by quasielastic neutron scattering

To investigate the self-dynamics in Zr-Ti melts quasielastic neutron scattering (QENS) experiments were carried out at the multi disc time-of-flight spectrometer TOFTOF at MLZ in Garching [213, 214]. An incident neutron wavelength of 7 Å and a chopper-speed of 6000 rpm were selected. The incoherent scattering cross-section of Titanium is $\sigma_{inc}(Ti) = 2.87$ barn at a neutron wave length of $\lambda = 1.798$ Å and $\sigma_{inc}(Zr) = 0.02$ barn in case of Zirconium [112]. The investigated compositions were the same as in the previously discussed x-ray scattering experiments: $Zr_{15}Ti_{85}$, $Zr_{32.4}Ti_{67.6}$, $Zr_{50}Ti_{50}$ and Zr_2Ti. The melts were processed by electromagnetic levitation. Due to the negligible scattering cross-section of Zirconium primary the dynamics of Ti-atoms are investigated in the binary Zr-Ti compositions.

In Fig. 4.20 the dynamic structure factor $S(Q,\omega)$ of $Zr_{50}Ti_{50}$ is depicted for the two temperatures 1870 K and 2000 K at a momentum transfer of $Q = 0.4$ Å^{-1}. The data reduction procedure followed the same routine as described in section 4.1.3. In addition, the dynamic structure factor $S(Q,\omega)$ of $Zr_{15}Ti_{85}$ is shown for the two temperatures 1870 K (blue) and 2000 K (red) at the momentum transfer of $Q = 0.4$ Å^{-1}. The higher Q-value results in higher energy transfers of neutrons within the scattering process and, therefore, a broadening of the quasielastic line width.

The self-diffusion coefficients of the investigated binary alloys are shown in Fig. 4.21 in a logarithmic scale versus the inverse temperature. In addition, the self-diffusion coefficients of pure Titanium are shown [198]. The instrumental error bars are only of the size of the symbols. Such a high accuracy is the result of combining the benefits of containerless levitation techniques with the high signal-to-noise ratio for QENS-experiments at TOFTOF and the high flux of MLZ. Therefore, even minor changes in the Ti-diffusivities in the respective compositions can be resolved.

Referring back to Fig. 4.12, where the self-diffusion constants of liquid Titanium is compared to the solid counterparts, all measured self-diffusion coefficients would overlie on the values of liquid Titanium and thus appear in the logarithmic scaling to be similar. The D-values of all investigated samples are on the order of 10^{-9} m^{1}s^{-1} and the overall differences within the self-diffusion coefficients are less than 20 %. For all compositions D is well described by an Arrhenius temperature dependence (fitted lines) in the investigated

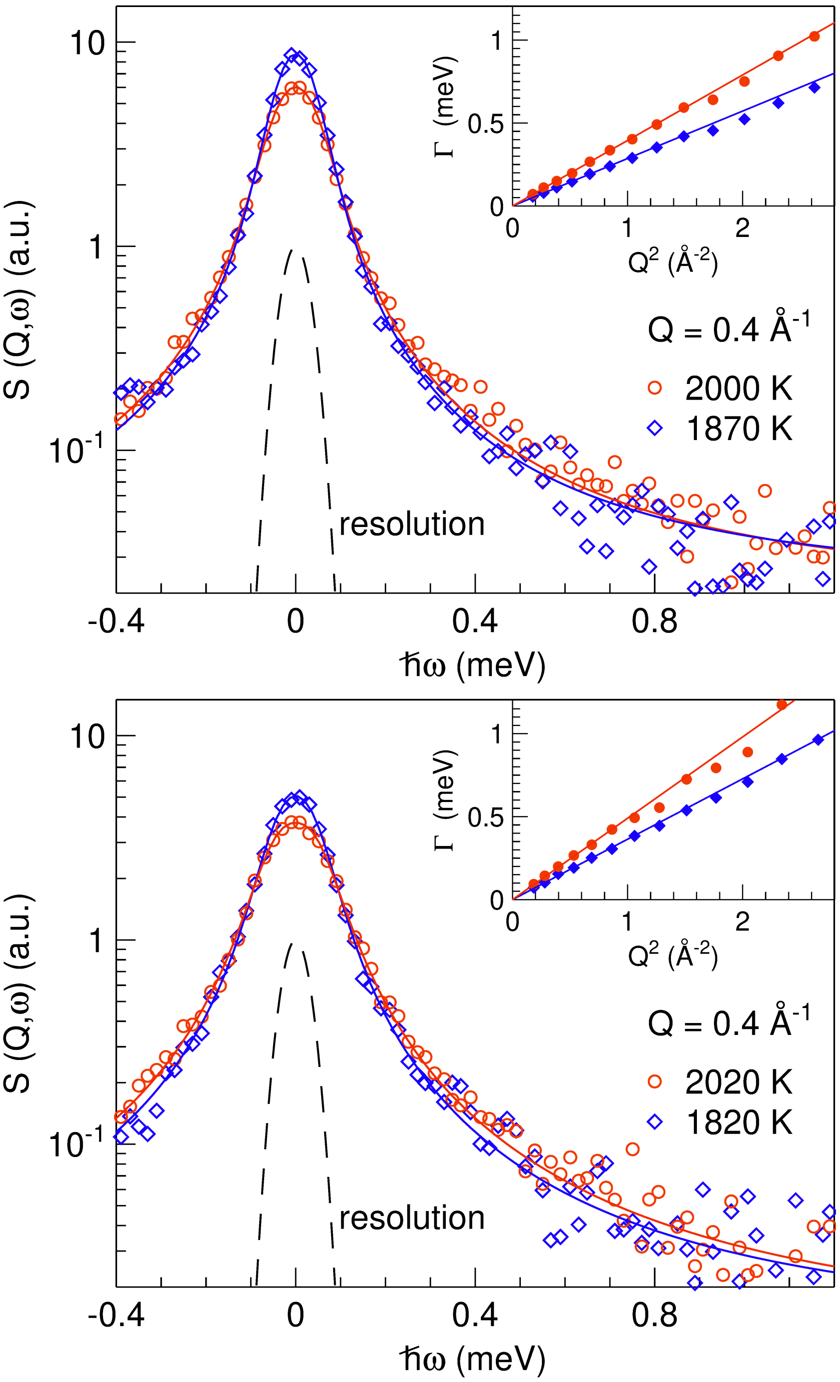

Figure 4.20: Dynamic structure factor $S(Q,\omega)$ at a Q-value of 0.4 Å^{-1} of $Zr_{50}Ti_{50}$ at two temperatures 1870 K (blue) and 2000 K (red) (top) and of $Zr_{15}Ti_{85}$ at two temperatures 1820 K (blue) and 2020 K (red) (bottom). The spectra are fitted with a Lorentzian function convoluted with the instrumental resolution function (black dashed line). In the inserts the resulting HWHMs as a function of Q^2 are shown for both respective temperatures.

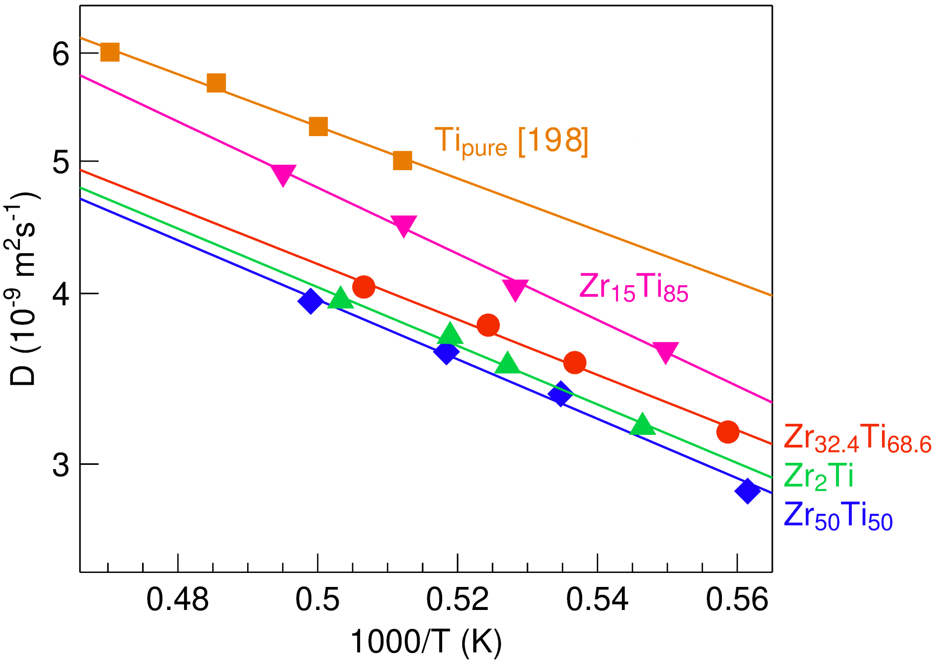

Figure 4.21: Temperature dependent self-diffusion coefficients of $Zr_{15}Ti_{85}$ (violet), $Zr_{32.4}Ti_{67.6}$ (red), $Zr_{50}Ti_{50}$ (blue) and Zr_2Ti (green) composition when compared to the self-diffusion coefficients of pure Titanium (orange) [198].

temperature range, which can be expressed by

$$D = D_0 \exp(-\frac{E_A}{k_B T}), \tag{4.9}$$

where D_0 is the diffusion coefficient at infinite temperature, E_A is the activation energy and k_B the Boltzmann constant.

In all investigated Zr-Ti melts the Ti-self-diffusivity is lower than in pure Titanium. Additionally, the atomic motion is concentration dependent and is slowest in $Zr_{50}Ti_{50}$ at a same temperature. Following, the Ti-self-diffusivity in liquid Titanium and Zr-Ti melts at a temperature of $T = 1973$ K is shown in Fig. 4.22 as a function of the Ti-concentration in the binary mixture. Since the measured data points spread in temperature, the fitted Arrhenius relations of all measured compositions are, therefore, extrapolated to a constant temperature value.

The atomic motions shows a decrease coming from pure Titanium towards the binary concentrations. However, this dependency can just be proven on the Ti-rich side. The weak incoherent scattering contribution of Zirconium results in low counting statistics on the Zr-rich side, where also the Ti-concentrations are too low to determine self-diffusion coefficients. As an example, the investigated dynamic structure factor of pure Zirconium

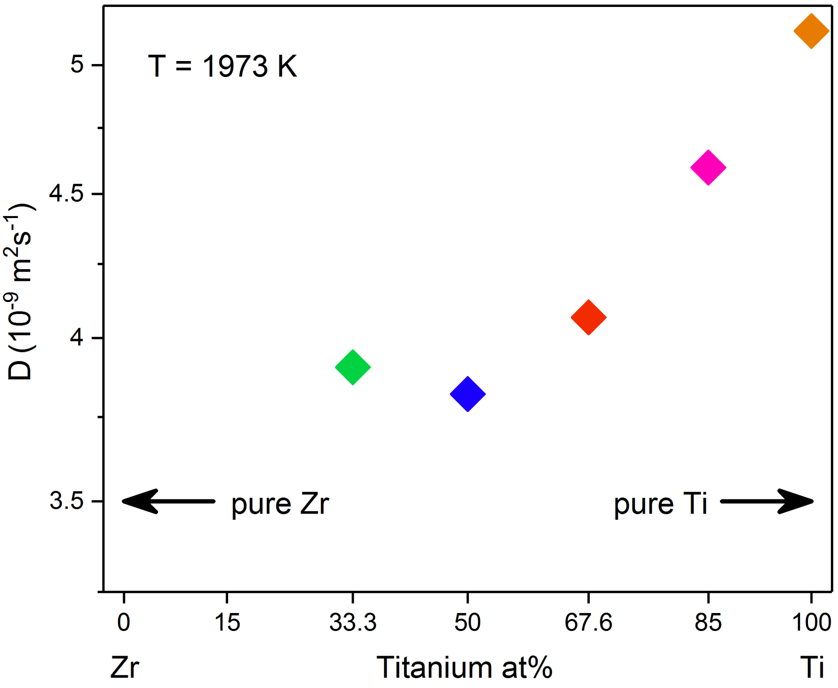

Figure 4.22: Self-diffusion coefficients of $Zr_{15}Ti_{85}$ (violet), $Zr_{32.4}Ti_{67.6}$ (red), $Zr_{50}Ti_{50}$ (blue) and Zr_2Ti (green) and pure Titanium (orange) [198] at $T = 1973$ K.

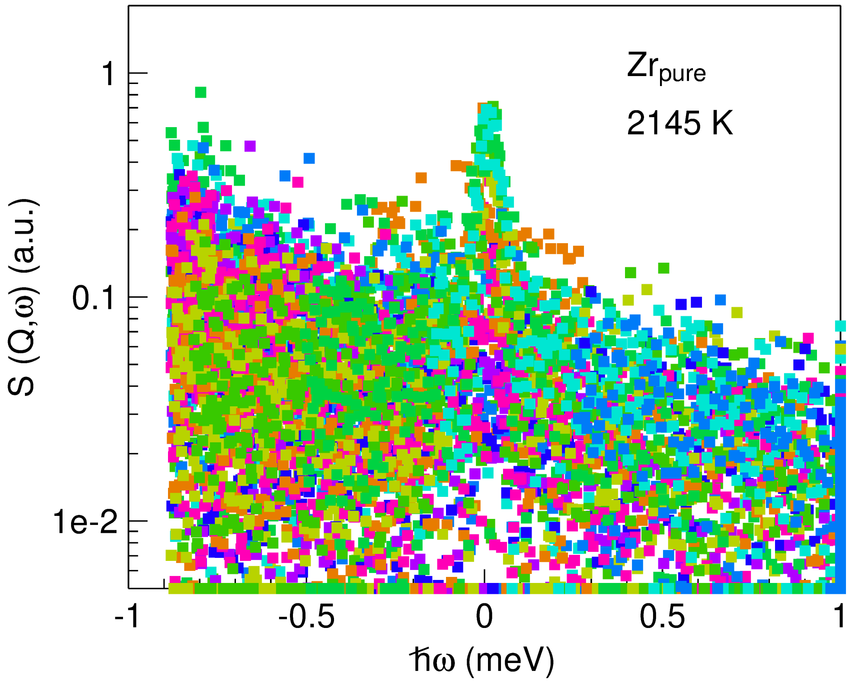

Figure 4.23: Dynamic structure factor $S(Q, \omega)$ of pure Zirconium processed by electromagnetic levitation at $T = 2123$ K, investigated for 1h at TOFTOF. The different colors refer to different momentum transfers.

is shown in Fig. 4.23.

Here, the different colors refer to different momentum transfers. The samples temperature is 2123 K and the melt was processed by electromagnetic levitation. Even though the measurement time was set to one hour, even the elastic line is barely distinguishable from the background. Consequently, any evaluation of momentum transfer, quasielastic broadening and therefore the Zr self-diffusion is impossible.

Considering the cage model a lower diffusivity occurs when the nearest-neighbor arrangement around a given atom results in a denser atomic packing, which thereby hinders atomic escape out of the cage. A theoretical explanation of the cage model is given by mode-coupling theory and is discussed in the subsequent subsection.

4.2.5 Calculated motion by mode-coupling theory using hard spheres

To investigate the relation between the structure and the dynamics in Zr-Ti melts (constant packing fraction and a minimum in diffusivity at $Zr_{50}Ti_{50}$), mode-coupling theory, which predicts the dynamics in dense fluids from the static structure factors, is used. MCT thus provides a direct link between these properties in metallic melts. In liquids, a self-diffusion process happens when an atom escapes from the cage, which is formed by the surrounding neighboring atoms. The self-diffusion process is therefore connected to a structural relaxation.

At the glass-transition temperature MCT predicts a diffusion coefficient of zero, since the memory kernel neglects certain relaxation processes. On the other hand, in the gas state the diffusion process underlays a complete different mechanism, where the dynamics are driven by binary collisions. MCT has shown to be a precise tool to explain the melt dynamics close to the glass-transition in the intermediate region between the glassy and the gaseous state, where melts are in a moderate viscous region, what is the case for Zr-Ti melts exhibiting diffusion coefficients on the order of 10^{-9} $\mathrm{m^2s^{-1}}$.

The input parameters of the MCT calculations are the number density n (which can be extracted from the molar volume $V_m = \frac{N_A}{n}$), the binary concentration, the respective atom radii and the partial static structure factor. In order to keep the modeling as simple as possible, the present structure was assumed to be only topologically ordered using a hard-sphere model approach. Respective structure factors were calculated by the Percus–Yevick approximation [274]. However, MCT is also able to predict the dynamics directly from measured partial structure factors if the full set of partial structure factors is available [63, 64].

MCT calculations overestimate the reduction of the dynamics at the glass-transition temperature. In addition, the absolute value of the critical temperature from MCT calculations was found to be different to experimentally obtained temperatures [142], resulting in a systematic error in absolute scale. Following, all predicted dynamics are always just of qualitative nature. However, since the temperature is incorporated in the number density n, the density can be reduced in order to receive diffusion coefficients on the same order than experimentally obtained values [142].

For all investigated binary alloys the calculations was done at a constant packing fraction. To simplify the experiment, the density used to derive the diffusion coefficient of the Zr_2Ti composition was reduced empirically until MCT predicted a similar value than the

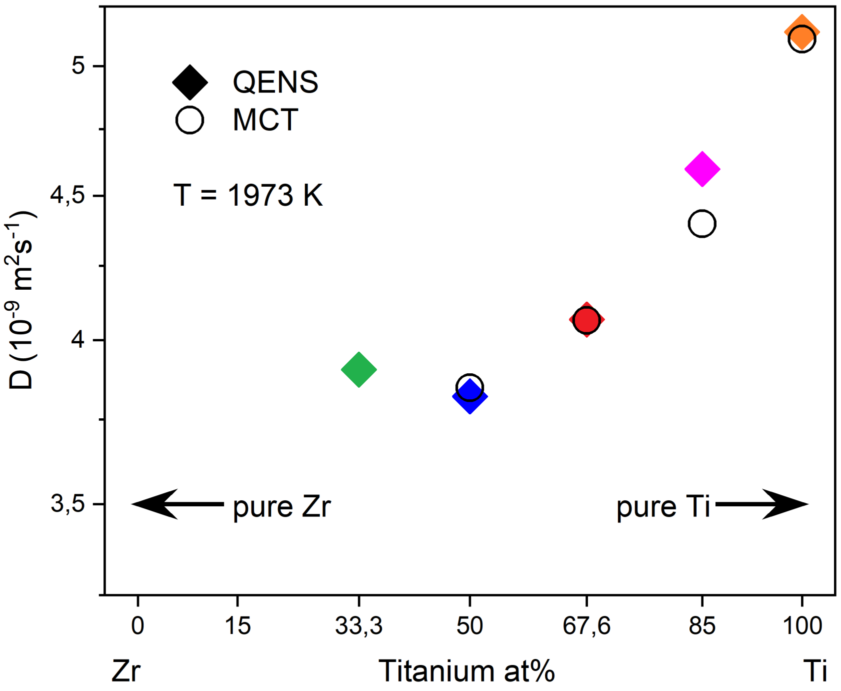

Figure 4.24: Comparison of MCT calculations with measured self-diffusion coefficients of $Zr_{15}Ti_{85}$ (violet), $Zr_{32.4}Ti_{67.6}$ (red), $Zr_{50}Ti_{50}$ (blue) and Zr_2Ti (green) compositions and pure Titanium (orange) [198] at $T = 1973$ K.

measured diffusion coefficient, revealing a reduction ratio of 0.87. This ratio was then resumed for the other investigated concentrations.

The results of the MCT calculations on Titanium self-diffusion in Zr-Ti and Titanium melts are shown in Fig. 4.24 (black points) in comparison to the measured self-diffusion constants from Fig. 4.22. In this case the predicted values of the Ti-motion in Zr-Ti binary mixtures by MCT calculations are in perfect agreement with the QENS measurements of the Titanium self-diffusion and displays the concentration dependency as well. It is obvious, that this just reflects the temperature of 1973 K. However, the obtained temperature dependencies in Fig. 4.5 are similar for the investigated concentrations, why related findings can be assumed also for other temperatures.

Using MCT calculations Götze and Voigtmann investigated composition changes on the dynamics in binary mixture based on a hard sphere approach without any chemical interactions [275]. For atomic radii ratios of 0.8 (in case of Zr-Ti melts the ratio is 0.92) a constant packing fraction was found. In contrast, at the liquid-glass transition their calculations showed an increase in relaxation time (what is according to equation 2.46 proportional to the inverse of the self-diffusion coefficient) of three orders of magnitude towards a minimum close to the 50 at.% composition. In case of the investigated Zr-Ti melts this increase is only about 20 %, but shows a qualitative similar compositional dependence at a constant packing fraction at a similar atomic size ratio. This is due to the fact, that the measured self-diffusion coefficients are far away from the respective glass-transition temperatures, since the Zr-Ti system exhibit rather weak glass-forming abilities [276].

This shows, that the self-dynamics in Zr-Ti melts can be explained by MCT using the topological considerations of a hard-sphere approach for which no assumptions on chemical interactions are made. Since the predicted and measured diffusion coefficients match with the use of the same reduced density ratio of 0.87, the constituent atoms in the liquid Zr-Ti system exhibit just differences in the atomic radii.

4.2.6 Conclusion

Binary compositions of the Zr-Ti system show very similar chemical and structural properties. Due to the negative coherent scattering length of Titanium a zero scatterer with composition $Zr_{32.4}Ti_{67.6}$ lead a direct measurement of the chemical structure factor using neutron diffraction. In this composition essentially no chemical short-range order is observed. When normalizing x-ray structure factors in Zr-Ti alloys to the position of the structure factor maximum, the observed total structure factors appear to be similar and alike those of the pure elements. The local structures contain an icosahedral short-range order. Density measurements reveal an ideal mixing behavior. An observed concentration dependent self-diffusivity was analyzed by MCT calculations using a hard-sphere approach at a constant packing fraction with a moderate size disparity for which no assumptions on chemical interactions were made, which were found to be in very good agreement with the measurements.

4.3 Structure and dynamics in bulk metallic glass forming liquids with minor additions

Bulk metallic glasses (BMGs) have considerable potential as advanced engineering materials [277] and are receiving much attention throughout the scientific community [278, 279]. Enhancing the glass-forming ability of alloys through the minor addition of specific elements is a technique currently at the forefront of BMG design [74–78]. Here, the addition of only 4 at.% Al or Ti to binary $Zr_{50}Cu_{50}$ increases its critical casting thickness from 2 mm to at least 5 mm [79]. How large this difference is can be seen in Fig. 4.25.

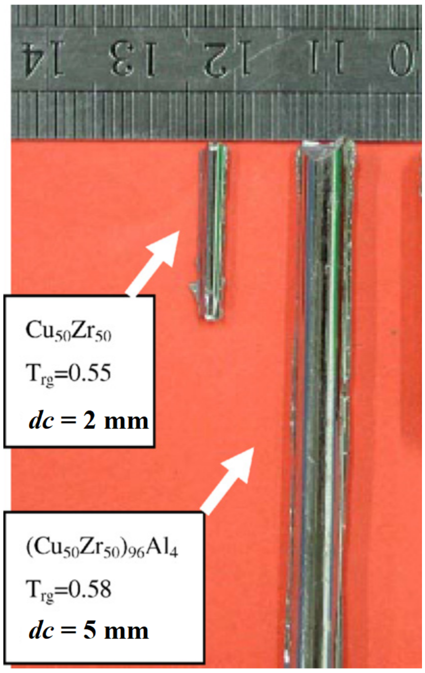

Figure 4.25: Improved glass-forming ability of Zr-Cu alloys with minor Aluminum and Titanium additions. Shown is the increase in critical casting thickness dc from 2 mm in case of the binary $Zr_{50}Cu_{50}$ to 5 mm in case of the ternary $(Zr_{50}Cu_{50})_{96}Al_4$ [77].

Other binary systems based on e.g. Zr-Ni [280], Ni-Nb [281] and Cu-Ti [282] show similar effects when alloyed with the suitable minor additions. Despite extensive review on this subject [77], the reasons for such a dramatic increase in glass-forming ability as a result of minor additions remain largely unknown and often speculative.

Many suggest that minor additions promote glass formation through increased atomic packing and local chemical short-range ordering [75, 283–286]. This may thermodynamically destabilize the formation of competing crystal phases [282, 287], as well as retard crystallization kinetics by lowering the mobility in the melt during cooling [288, 289]. Certain minor additions (e.g. Aluminum) might even help to avoid heterogeneous nucleation by scavenging harmful oxygen impurities [290]. However, very few studies are actually carried out in the melt to directly test these assumptions – especially at the atomic level. Understanding how minor additions impact the glass-forming ability of metallic melts is a key to predictive BMG design. In this respect, direct investigations of the atomic structure and dynamics of the melt are absolutely essential for identifying the important microscopic mechanisms underlying bulk glass formation.

4.3.1 Structural investigation and packing fraction

To investigate any structural role played by the minor addition high-energy synchrotron X-ray diffraction experiments were carried out at the ID11 beamline of the ESRF in Grenoble. Samples were processed using electrostatic levitation. Multiple heating and cooling cycles, in which the sample was progressively heated towards higher temperatures, in order to remove melt impurities and achieve deeper undercoolings, were employed. By means of this, measurements of total structure factors of the melt are possible.

In Fig. 4.26 the total structure factors $S(Q)$ of the binary $Zr_{50}Cu_{50}$ and the two ternary $(Zr_{50}Cu_{50})_{96}Al_4$ and $(Zr_{50}Cu_{50})_{96}Ti_4$ melts at a temperature of 1175 K are depicted. For clarity, the curves are shifted in the vertical direction. The data of the ternary $(Zr_{50}Cu_{50})_{96}(Ti, Al)_4$ melts reveal no significant changes of the total $S(Q)$ as compared with that of the binary $Zr_{50}Cu_{50}$ alloy. The position and shape of the respective maxima are almost identical. In this respect, only 4 at.% of another component appears to induce only weak changes. In addition, the total scattering cross-section is also only weakly affected by minor additions. Therefore, it is also unlikely that a significantly changed chemical short-range order could be observed even by varying the scattering cross-sections, for example by using isotopic substitution of Copper.

From the macroscopic density, which was measured in a stationary electrostatic levitation facility, an average atomic packing density can be determined as described in section 2.4. The respective results are depicted in Fig. 4.27. Densely packed melts can be a structural origin for a pronounced glass-forming ability, which can be achieved e.g. by a distribution in atomic radii [283, 291]. In $(Zr_{50}Cu_{50})_{96}(Ti, Al)_4$ this is the case, since Zirconium exhibits an atomic radius of $r_{Zr} = 1.60$ Å and Copper of $r_{Cu} = 1.28$ Å [67], while the atomic radii in Titanium and Aluminum are very similar and different to the binary components: $r_{Ti} = 1.47$ Å and $r_{Al} = 1.43$ Å [67]. However, the packing fraction of the three alloy melts are roughly equal within the experimental uncertainty of ca. 1 %, even though the Ti-bearing liquid exhibits a slightly denser packing.

On the other hand, this just reflects that no structural changes on the Zr-Cu-matrix occurred upon minor addition. Local changes around the Aluminum and Titanium atoms are not reflected due to the small concentrations. Moreover, the investigations of this work on the Zr-Ti system showed, that indeed the melt dynamics can be affected even when the structure factor and the packing fraction remains unchanged. It is therefore also necessary to examine how the minor addition affects the viscosity and the diffusivity on the atomic level in order to glean information on its role in enhancing glass formation.

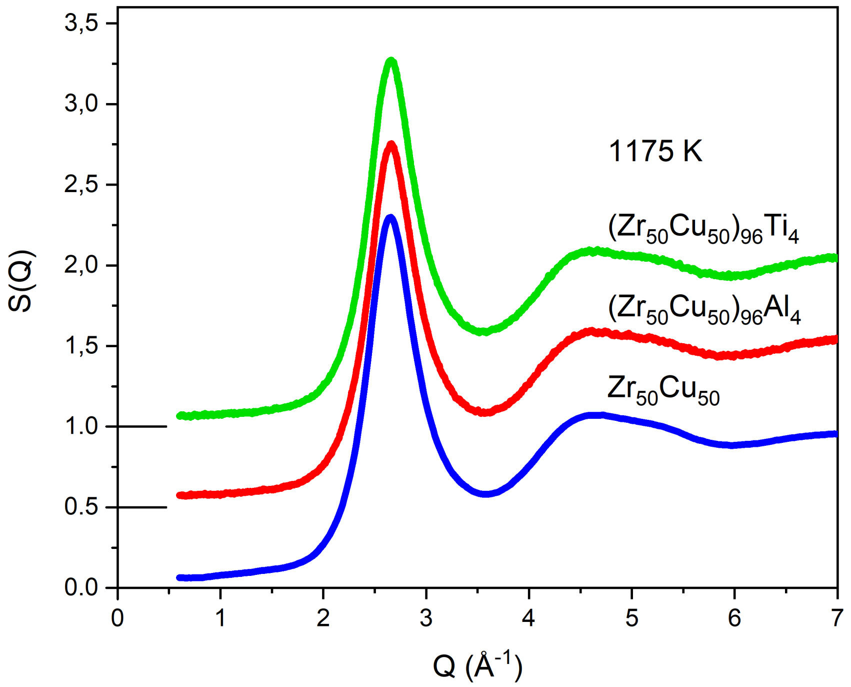

Figure 4.26: The liquid structure factor of $Zr_{50}Cu_{50}$ (blue), $(Zr_{50}Cu_{50})_{96}Al_4$ (red) and $(Zr_{50}Cu_{50})_{96}Ti_4$ (green) melts at 1175 K, measured by synchrotron X-ray diffraction.

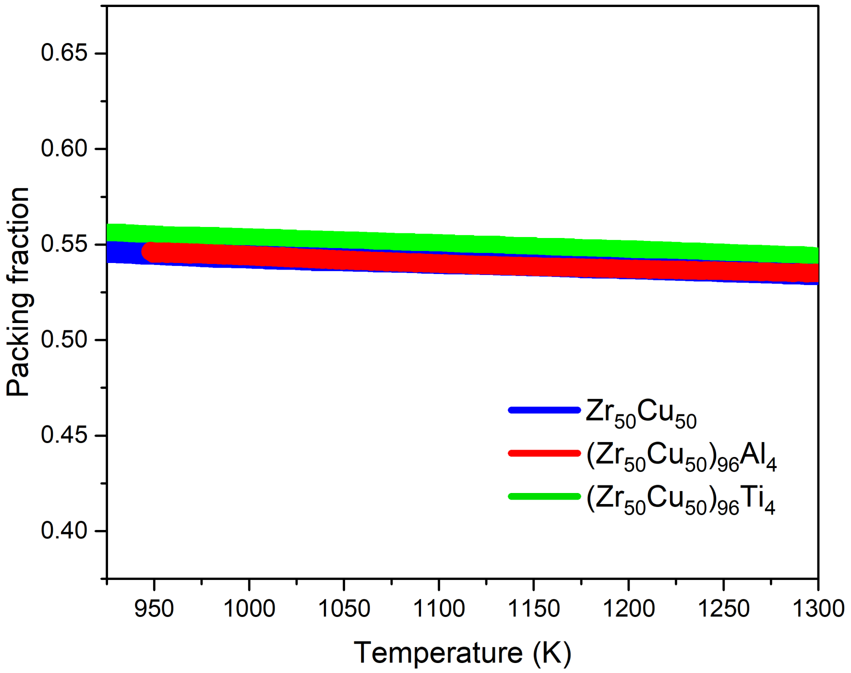

Figure 4.27: Temperature dependent packing fraction in $Zr_{50}Cu_{50}$ (blue), $(Zr_{50}Cu_{50})_{96}Al_4$ (red) and $(Zr_{50}Cu_{50})_{96}Ti_4$ (green) alloys as as calculated from the macroscopic density.

4.3.2 Viscosity

The melt viscosities of the binary $Zr_{50}Cu_{50}$ as well as ternary $(Zr_{50}Cu_{50})_{96}Al_4$ and $(Zr_{50}Cu_{50})_{96}Ti_4$ alloys were investigated using a stationary electrostatic levitation facility. The viscosity was determined at each temperature by measuring the decay of surface oscillations induced by a sinusoidal electric field. Through the decay time of the oscillation, the viscosity is calculated using the procedure described in section 3.4.

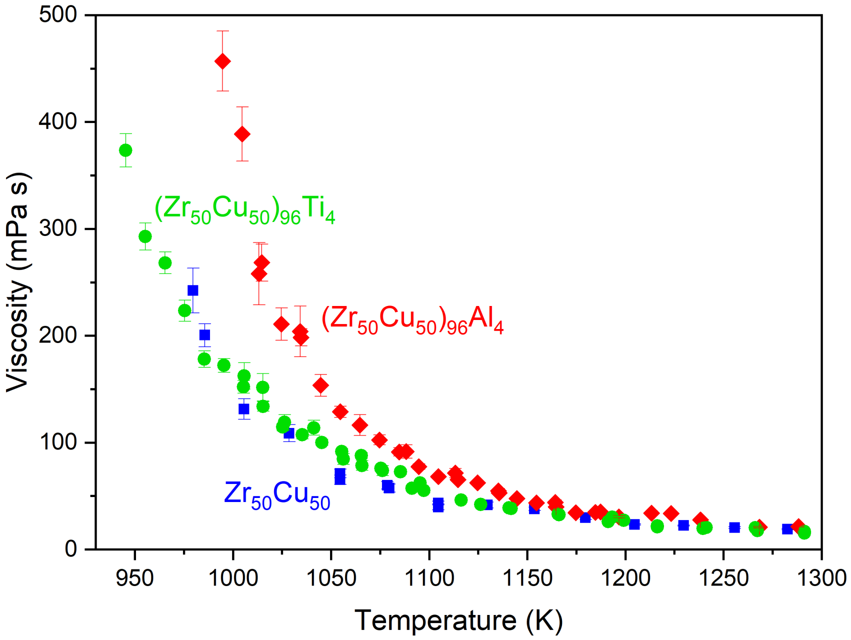

Figure 4.28: Temperature dependent viscosity in $Zr_{50}Cu_{50}$ (blue squares), $(Zr_{50}Cu_{50})_{96}Al_4$ (red diamonds) and $(Zr_{50}Cu_{50})_{96}Ti_4$ (green dots) alloys as determined by the oscillated droplet method in electrostatic levitation.

In Fig. 4.28 an overview of the measured melt viscosities of $Zr_{50}Cu_{50}$, $(Zr_{50}Cu_{50})_{96}Al_4$ and $(Zr_{50}Cu_{50})_{96}Ti_4$ is shown. Here, the blue squares refer to $Zr_{50}Cu_{50}$, the red diamonds to $(Zr_{50}Cu_{50})_{96}Al_4$ and green dots to $(Zr_{50}Cu_{50})_{96}Ti_4$.

From the shown data, it can be seen that the addition of only 4 at.% Aluminum causes a significant increase in the viscosity towards lower temperatures compared to that of binary $Zr_{50}Cu_{50}$. For example, the viscosity of $(Zr_{50}Cu_{50})_{96}Al_4$ at 1100 K is about 44 % higher than the one of $Zr_{50}Cu_{50}$ at the same temperature. Such an increase in viscosity is in line with an increased glass-forming ability [171, 259, 292], since slow melt dynamics facilitate glass-formation. In contrast, the addition of the same amount of Titanium has no discernible effect on the viscosity when compared to $Zr_{50}Cu_{50}$.

However, the viscosity reflects only the melt dynamics on a macroscopic level. To determine the atomic mobility, it is necessary to investigate the self-diffusion in the ternary $(Zr_{50}Cu_{50})_{96}(Ti, Al)_4$ melts.

4.3.3 Atomic dynamics as studied by quasielastic neutron scattering

Self-diffusion coefficients of $Zr_{50}Cu_{50}$, $(Zr_{50}Cu_{50})_{96}Al_4$ and $(Zr_{50}Cu_{50})_{96}Ti_4$ were measured using quasielastic neutron scattering on the time-of-flight spectrometer TOFTOF at the MLZ in Garching using an incident neutron wavelength of 7 Å at a chopper-speed of 6000 rpm. The melts were processed by electrostatic levitation. Due to the incoherent scattering cross-sections - $\sigma_{inc}(Zr) = 0.02$ barn, $\sigma_{inc}(Cu) = 0.55$ barn, $\sigma_{inc}(Al) = 0.0082$ barn and $\sigma_{inc}(Ti) = 2.87$ barn [112] - mainly the self-diffusion of Copper is reflected in the measurements of $Zr_{50}Cu_{50}$ and $(Zr_{50}Cu_{50})_{96}Al_4$. However, in case of $(Zr_{50}Cu_{50})_{96}Ti_4$ a concentration weighted average self-diffusion coefficient of Copper and Titanium is determined. However, the Cu self-diffusion is predominant with a ratio of $D_{Cu}/D_{Ti} = 2.3$.

The self-diffusion coefficients of the investigated alloys are depicted in Fig. 5.1 as a function of the inverse temperature. Here, the solid lines are fits to the Arrhenius relation

$$D = D_0 \exp(-\frac{E_A}{k_B T}), \tag{4.10}$$

where E_A is the activation energy for self-diffusion, D_0 is the diffusion coefficient at infinite temperature and k_B is the Boltzmann constant.

It is apparent from these data that the minor addition of both Aluminum and Titanium has a noticeable impact on the microscopic dynamics of these melts. In both ternary melts $(Zr_{50}Cu_{50})_{96}Al_4$ and $(Zr_{50}Cu_{50})_{96}Ti_4$ a reduction in the absolute values of the self-diffusion coefficients at each investigated temperature is observed when compared to binary $Zr_{50}Cu_{50}$.

This in line with an increased activation energy in those ternary alloys. E_A increases for Cu-self-diffusion from $E_{A,Zr_{50}Cu_{50}} = 0.51 \pm 0.03$ eV in $Zr_{50}Cu_{50}$ to $E_{A,(Zr_{50}Cu_{50})_{96}Al_4} = 0.78 \pm 0.05$ eV in $(Zr_{50}Cu_{50})_{96}Al_4$. In case of $(Zr_{50}Cu_{50})_{96}Ti_4$ the activation energy of the averaged Cu/Ti-self-diffusion is $E_{A,(Zr_{50}Cu_{50})_{96}Ti_4} = 0.65 \pm 0.08$ eV, which is also higher than the Cu-self-diffusion coefficient in $Zr_{50}Cu_{50}$.

Same as the melt viscosity, the dependence of the self-diffusion coefficients on the minor addition element clearly does not follow the trend as the packing density. But, a correlation between atomic diffusivity and glass-forming ability is observed in $(Zr_{50}Cu_{50})_{96}Al_4$ and $(Zr_{50}Cu_{50})_{96}Ti_4$. In the Al-bearing alloy the reduction in D appears to correlate with the overall increase in melt viscosity also quantitatively. Where $\eta_{Zr_{50}Cu_{50}}/\eta_{(Zr_{50}Cu_{50})_{96}Al_4}$ at 1100 K was found to be 0.56, $D_{(Zr_{50}Cu_{50})_{96}Al_4}/D_{Zr_{50}Cu_{50}}$ is 0.53 at the same temperature.

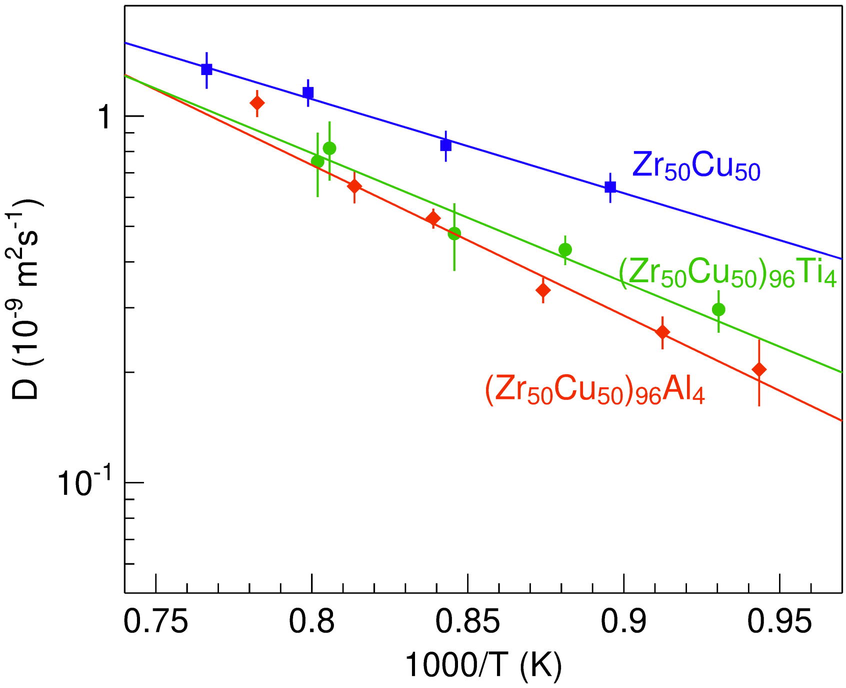

Figure 4.29: Self-diffusion coefficients of $Zr_{50}Cu_{50}$ (blue squares), $(Zr_{50}Cu_{50})_{96}Al_4$ (red diamonds) and $(Zr_{50}Cu_{50})_{96}Ti_4$ (green dots) melts, investigated with quasielastic neutron scattering. The lines refer to Arrhenius fits of the measured values.

For the Ti-bearing alloy it seems that the change in the diffusion coefficient compared to the binary $Zr_{50}Cu_{50}$ alloy is larger than the change in the melt viscosity upon Titanium addition. This might be correlated with the fact that in contrast to Aluminum, Titanium also contributes to the measured self-diffusion coefficient by QENS. This would indicate that there are certain differences of the dynamics between the components in the Ti-bearing melt.

Obviously, the effect of minor additions on the enhanced glass-forming ability in these systems is more complex than what is assumed from simple packing considerations. Instead of the packing fraction, contributions from chemical interactions are expected to play a much more important role in the liquid dynamics via chemical short-range order or possibly electronic effects [61, 62, 188, 293–297].

Compared to the Zr-Ti system, which itself exhibits rather weak chemical interactions, the observed changes in the melt dynamics are much more sensitive to composition in $(Zr_{50}Cu_{50})_{96}(Ti,Al)_4$ alloys upon minor additions than in Zr-Ti, where the overall decrease in diffusivity over the entire phase diagram was less than 20 %.

4.3.4 Phase selection during solidification

Since the glass-forming ability can also depend on competing crystal phases during solidification [282, 287], it is important to determine these. In-situ crystallization studies of undercooled $(Zr_{50}Cu_{50})_{96}(Ti, Al)_4$ minor-addition melts were carried out at the ID11 beamline at the ESRF in Grenoble.

In Fig. 4.30 two representative time-temperature profiles of respectively $(Zr_{50}Cu_{50})_{96}Al_4$ and $(Zr_{50}Cu_{50})_{96}Ti_4$ are shown. Here, the shaded band demarcates the solid-liquid coexistence region upon heating. After heating the levitated droplet to the desired temperature, the laser power is shut off and the temperature is thus lowered via radiative cooling of the sample. Heating to higher temperatures generally leads to a larger degree of undercooling before crystallization sets in, which is indicated by recalescence of the sample (an increase in the temperature due to the release of latent heat).

For both shown compositions $(Zr_{50}Cu_{50})_{96}Al_4$ and $(Zr_{50}Cu_{50})_{96}Ti_4$, similar crystallization behavior can be noticed in the time-temperature curves. For those samples that only undercool by approximately 100 K, a double recalescence behavior is observed. Those that undercool by roughly 250 K undergo only one crystallization event.

Examination of the X-ray diffraction patterns taken during these crystallization events reveals noticeable differences in the propagation of the resulting crystalline phases. However, for both $(Zr_{50}Cu_{50})_{96}Al_4$ and $(Zr_{50}Cu_{50})_{96}Ti_4$ alloys the final diffraction pattern of the respective alloy was similar after both solidification paths. In Fig. 4.31 the respective diffraction patterns of $(Zr_{50}Cu_{50})_{96}Al_4$ and $(Zr_{50}Cu_{50})_{96}Ti_4$ are depicted.

The ZrCu $B2$-bcc phase (high temperature phase at 50 at.% Zr in the phase diagram in Fig. 4.32 [298]) is the dominant crystallization product of both compositions, similar to what is observed in binary $Zr_{50}Cu_{50}$ [299]. The samples exhibiting only moderate undercoolings solidify in two crystallization events. For instance, the $(Zr_{50}Cu_{50})_{96}Al_4$ composition first crystallizes in the $B2$-bcc phase, out of which another phase grows, as is seen by an additional reflections at around 2.8 $Å^{-1}$ and 4.8 $Å^{-1}$, during the 2nd recalescence. This phase also appears to be present in the deeply undercooled sample. Further Rietveld analysis defined this additional crystallization product to be the ternary intermetallic Cu_2ZrAl bcc phase.

Fig. 4.33 shows SEM images the solidified microstructures of $(Zr_{50}Cu_{50})_{96}Al_4$ after both solidification paths, respectively. Although from an atomic structural point of view (diffraction pattern) both solids look identical, the microstructures differ significantly.

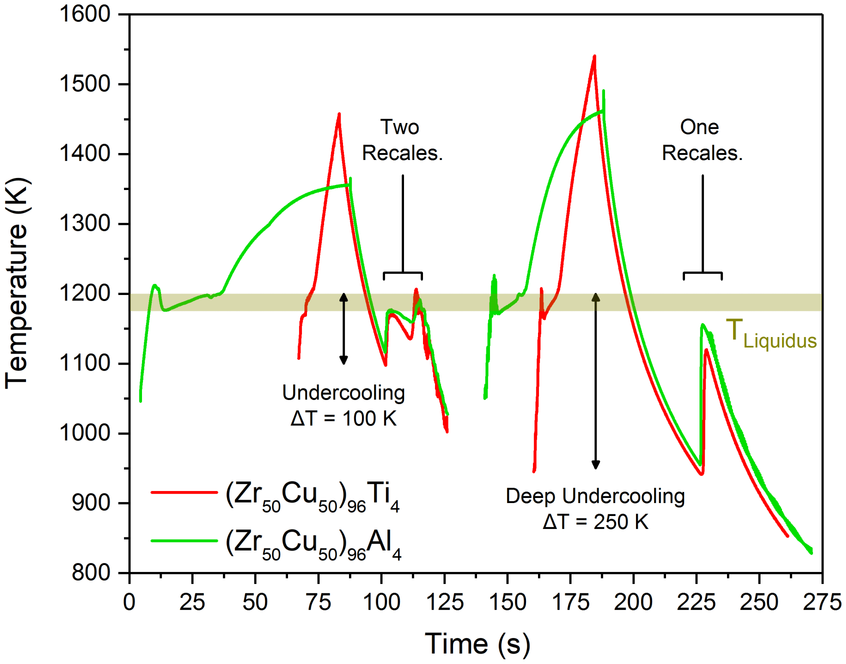

Figure 4.30: Temperature-time profile of the processing of $(Zr_{50}Cu_{50})_{96}Al_4$ (red) and $(Zr_{50}Cu_{50})_{96}Ti_4$ (green) alloys in electrostatic levitation. Different solidification paths with two solidification events (left) or one solidification event (right) are observed.

The top image shows the microstructure of a sample after two crystallization events. Here, EDX-analysis revealed the globular grains to be the during the first crystallization event grown $ZrCu$ $B2$-bcc phase. One can clearly see the grain boundaries appearing in lamellas, which usually stands for an eutectic composition. The dark blackish parts are identified to be the Cu_2ZrAl bcc phase. Contrary to that is the bottom image, which shows the microstructure of a sample that solidified with one crystallization event. Here, the microstructure shows a mixture of competing phases. Partially, dentritic growth paths can be suspected. Only on the bottom right side EDX reveals a grain originated by the Zr-Cu $B2$-bcc phase, which however appears in a different shape than from the solidification path with two crystallization events. The remaining microstructure is a mixture of the solidified phases and is not explicitly distinguishable by EDX-analysis. The increase of the total number of possible crystallization products has an impact on the nucleation probability in $(Zr_{50}Cu_{50})_{96}Al_4$.

On the other hand, the $(Zr_{50}Cu_{50})_{96}Ti_4$ composition, first crystallizes directly into the $B2$-bcc phase. During the 2nd recalescence another phase appears, identified with a reflection at around 2.6 Å^{-1}. This phase also grows out of the the deeply undercooled sample, alongside the $B2$-bcc phase. The Rietveld analysis revealed this phase to be

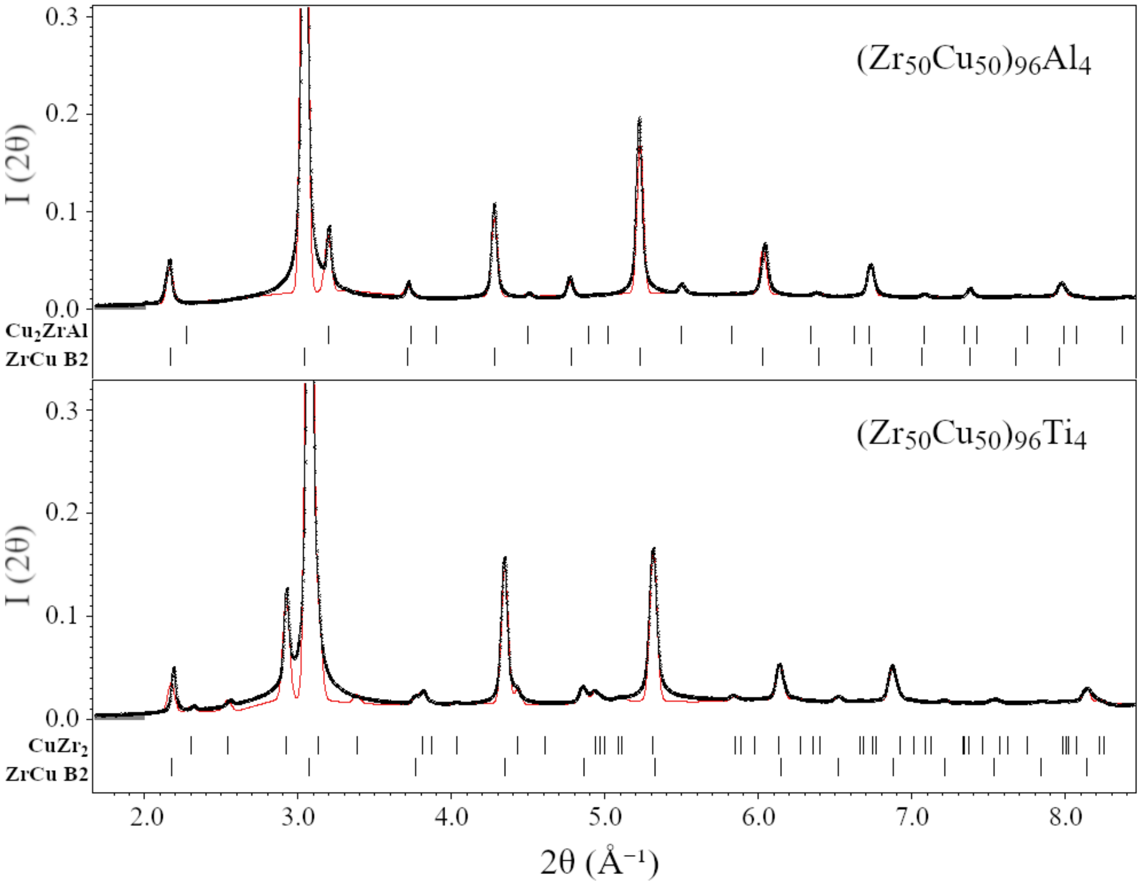

Figure 4.31: Diffractograms of $(Zr_{50}Cu_{50})_{96}Al_4$ (top) and $(Zr_{50}Cu_{50})_{96}Ti_4$ (bottom) alloys after both solidification paths. The red fits shows the phase selection of the Rietveld analysis. The respective phases are indicated.

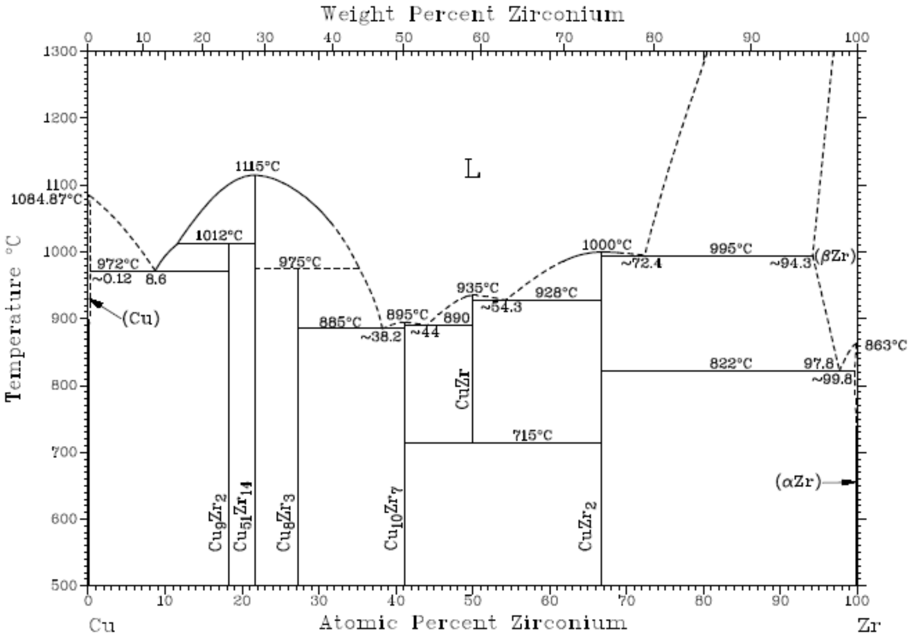

Figure 4.32: The phase diagram of the Zr-Cu system [298]. The left side refers to Copper and the right side to Zirconium.

the $CuZr_2$-tretagonal phase on the Zr-richer side of the Zr-Cu phase diagram, depicted in Fig. 4.32 [298]. Here, Titanium seems to be substituted on Zr-positions within the lattice. Referring back to the findings of the binary Zr-Ti system in the previous chapter this can be explained by the chemical and structural similarities in Zirconium-Titanium compositions.

The maximum degree of undercooling observed in both ternary compositions is almost 50 K lower than what is reported for $Zr_{50}Cu_{50}$ [299]. This reduced undercoolability of $(Zr_{50}Cu_{50})_{96}Al_4$ and $(Zr_{50}Cu_{50})_{96}Ti_4$ can have multiple origins. One possibility is that the addition of another element increases the total number of possible crystallization products and thereby increases the overall nucleation probability. Indeed, the presence of small amounts of an additional crystalline phase alongside the $B2$-bcc phase in both deeply undercooled compositions would seem to support this. Another possibility is that the strong oxygen affinity of both Aluminum and Titanium introduces oxide impurities into the melt, which act as heterogeneous nucleation centers and catalyze crystallization [290]. This latter interpretation would also contradict the viewpoint that such minor additions enhance the glass-forming ability by acting as “scavengers” that dissolve oxide impurities on atomic length scales and thereby remove them as heterogenous nucleation sites [300].

Still remains the question how an improved glass-forming ability can be correlated to the

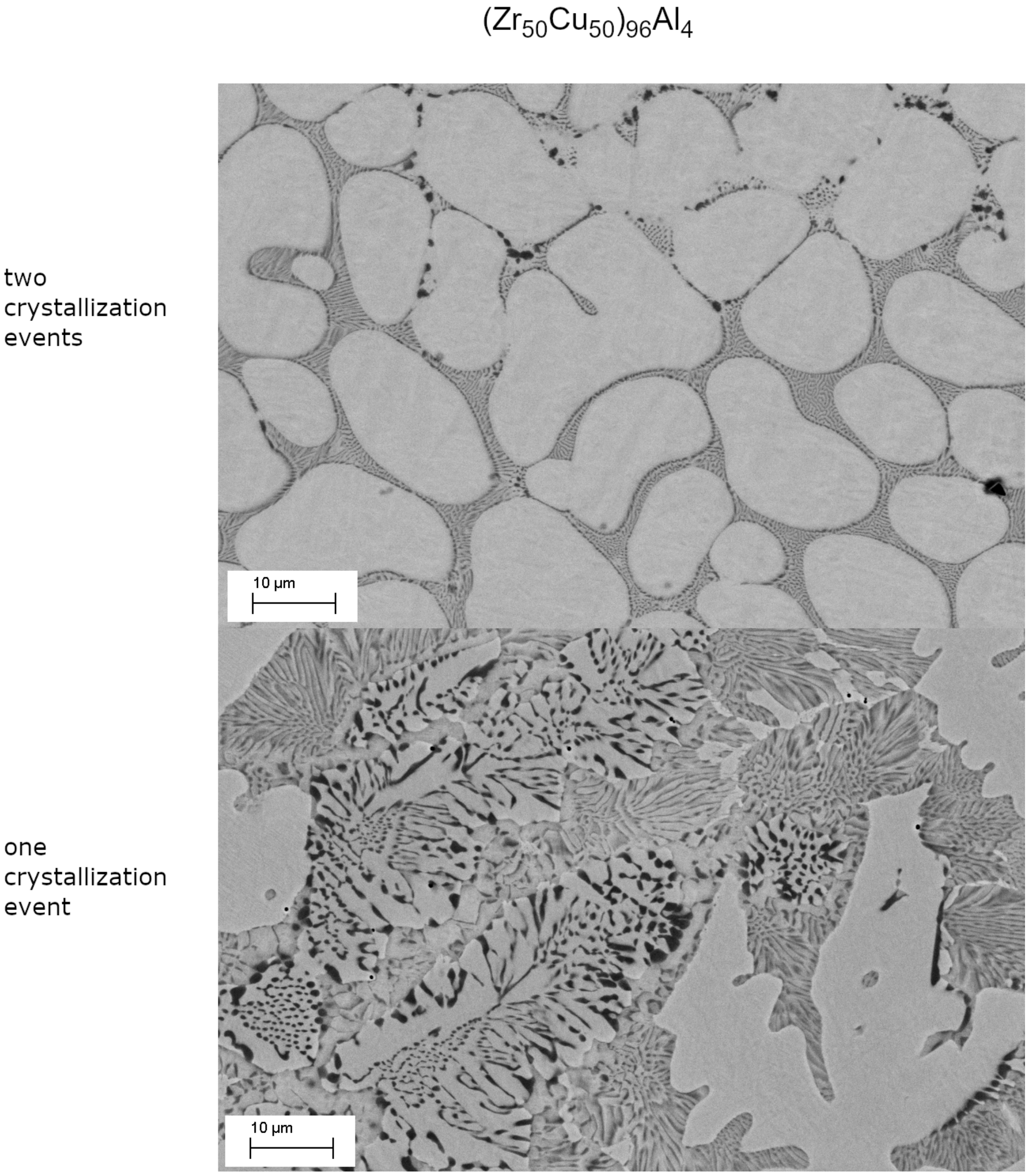
$(Zr_{50}Cu_{50})_{96}Al_4$
two crystallization events
10 µm
one crystallization event
10 µm

Figure 4.33: Pictures of detected backscattered electrons in SEM of Zr-Cu with minor Al additions after different solidification paths. The top one refers to solidification with two crystallization events and the bottom one to solidification after a single crystallization event.

lower undercoolabilities of the $(Zr_{50}Cu_{50})_{96}(Ti, Al)_4$ alloys during the moderate cooling in ESL. One explanation could be the overall nucleation rate, which depends - among other quantities - also on the mobility of the melt [301]. Due to the found decrease in the overall diffusivity in the $(Zr_{50}Cu_{50})_{96}(Ti, Al)_4$ systems dynamical effects are also likely on higher cooling rates.

4.3.5 Conclusion

Taken together, the $(Zr_{50}Cu_{50})_{96}(Ti, Al)_4$ systems suggest a positive correlation between an overall reduced atomic diffusivity and the reported enhanced glass-forming ability introduced by Aluminum and Titanium minor additions [287]. However, no correlation with a higher packing fraction is found. The Al-bearing composition shows a strong increase in viscosity opposite to the Ti-bearing one, where the viscosity appear to be very similar to the viscosity of $Zr_{50}Cu_{50}$. Both minor addition alloys show a similar crystallization behavior, which result in structures with different phases after solidification. Although there are different crystallization paths, the diffraction pattern of the completely solidified alloys appear similar. In case of the Al-bearing composition, beside the primary ZrCu $B2$-bcc phase the second phase is identified to be the ternary intermetallic Cu_2ZrAl-bcc phase, indicating a pronounced chemical short-range order of the system. For the Ti-bearing composition the second phase is the Zr-rich $CuZr_2$-tretagonal phase, where Titanium is substituted on Zr-positions in the lattice. The increase of total number of possible crystallization products (nucleation probability) can mark a structural origin for the enhanced glass forming ability of minor Al/Ti additions in the $Zr_{50}Cu_{50}$ system.

5 Conclusion and Outlook

5.1 Conclusion

Objective of this work was to study how structural properties like the atomic packing and chemical short-range order influence the atomic dynamics in metallic melts. Therefore, the highly dense pure element Mercury was investigated. In addition, a system with weak chemical short-range order, namely binary Zr-Ti alloys, and the ternary $(Zr_{50}Cu_{50})_{96}(Ti, Al)_4$ system with pronounced chemical short-range order was investigated.

Mercury, as the only liquid metallic element at ambient conditions, is an ideal candidate to investigate the transport mechanism in metallic liquids over a large temperature range. In this work an investigation of the atomic dynamics was carried out using quasielastic neutron scattering. The self-diffusivity of Mercury follows an Arrhenius behaviour over the entire investigated temperature range from 240 K to 350 K. The standard deviation of only 4 % is significantly more precise when compared to conventional long capillary measurements, which additionally are often hampered by convection.

Using the semi-empirical approach for liquid diffusion based on uncorrelated binary collisions derived by Kaptay [38] the self-diffusion coefficient at the melting point can be predicted. In case of Mercury the measured diffusive dynamics were found to be similar to alkali metal melts considering a hard-sphere model with an atomic packing of 45 % and an effective atom radius of 1.37 Å, which is close to the covalent radius. This indicates a dominant contribution of the repulsive part of the interatomic potential to the mass transport. However, the temperature dependence of the diffusion is less well predicted for Mercury as compared to that for the alkali melts, were also deviations from the prediction of the Sutherland-Einstein relation are found over a large temperature range.

Using neutron and x-ray scattering the melt dynamics and structure of binary Zr-Ti alloys was investigated. To avoid chemical interaction of the highly reactive melts with the container material, Zr-Ti melts were processed in electromagnetic levitation (EML). Zirconium and Titanium are both elements of the group 4 in the periodic table and show in the pure state very similar chemical and structural properties, but exhibit different atomic radii. Due to the negative coherent scattering length of Titanium, the binary composition $Zr_{32.4}Ti_{67.6}$ has a scattering length of zero for coherently scattered neutrons, such that the partial structure factor S_{CC}, that describes the chemical short-range order, can directly be measured. Neutron diffraction shows that barely any chemical short-range order is present in this composition.

Observed total structure factors of in the other Zr-Ti alloys, measured with x-rays from synchrotron radiation, are very similar to those of the pure elements. A normalization of the Q-range over the position of the structure factor maximum revealed that the local structures contain an icosahedral short-range order.

The macroscopic measured densities of Zr-Ti melts [273] are proportional to the degree of mixing and show ideal mixing behavior with negligible excess volume. Moreover, the volume expansion is similar in all investigated alloys. The atomic packing fraction is found to be steady at 46 % using Goldschmidt radii in all investigated Zr-Ti concentrations alike the pure elements.

Measurements of the self-diffusivity using quasielastic neutron scattering (QENS) show a concentration dependent motion of Ti-atoms in the melt. A calculation of the liquid dynamics using the mode-coupling theory (MCT), which predicts the dynamics from the static structure in dense fluids, was made based on an only topologically short-range ordered hard-sphere like approach without any chemical interactions. The results are in qualitative agreement with the results of the QENS measurements. This shows that the topological short-range order dominates the atomic motion in binary Zr-Ti melts. The concentration dependent changes can be attributed to differences in the atomic radii.

Minor additions of Aluminum and Titanium have shown to improve the glass-forming ability of $Zr_{50}Cu_{50}$. Using in-situ synchrotron x-ray diffraction and quasielastic neutron scattering (QENS), the interplay between melt structure and mass transport quantities like viscosity and self-diffusion was investigated in $(Zr_{50}Cu_{50})_{96}(Ti,Al)_4$ alloys, as well as the solidification behavior.

Combined with electrostatic levitation (ESL), the liquid properties of these chemically reactive alloys were measured over a large temperature range. At the liquidus temperature of $Zr_{50}Cu_{50}$, the self-diffusivity in the investigated $(Zr_{50}Cu_{50})_{96}Al_4$ and $(Zr_{50}Cu_{50})_{96}Ti_4$ alloys is almost a factor of two lower than in $Zr_{50}Cu_{50}$. For the $(Zr_{50}Cu_{50})_{96}Al_4$ alloy, this is in line with the observation that Aluminum addition leads to higher melt viscosities. In contrast, the average packing fractions of $Zr_{50}Cu_{50}$ and $(Zr_{50}Cu_{50})_{96}(Ti, Al)_4$ melts are very similar at about 55 %. Following the changes in the melt dynamics are very sensitive to the composition.

The ternary alloys also exhibit different crystallization behavior compared to that of $Zr_{50}Cu_{50}$, which vary with the heating temperature and cooling rate. Such, the melts either solidify by one or two crystallization events. However, the final diffraction pattern is similar after both crystallization paths, for the respective $(Zr_{50}Cu_{50})_{96}Al_4$ and $(Zr_{50}Cu_{50})_{96}Ti_4$ alloys. Both the sluggish dynamics and the complex solidification could contribute considerably to the improved glass-forming ability upon minor addition.

Finally, the investigations of this work reveal that the atomic packing of metallic melts cannot explain changes in the atomic motion only. Moreover, contributions from topological and chemical short-range order can have a dominant influence on the atomic dynamics in the metallic melts.

5.2 Outlook

The investigation of the influence of the short-range order on the melt dynamics can be continued based on the findings yielded in each chapter of this work. Those are respectively:

1. In order to investigate Kaptays approach of proportionality [38] with elements with low melting temperature one could consider Gallium (atomic number 31) or Indium (atomic number 49), which are both elements of the boron group. However, both elements exhibit higher melting temperatures than Mercury: $T_m(Ga) = 302.9$ K, $T_m(In) = 429.7$ K; and lower densities, which are 5.9 g/cm^3 in case of Ga and 7.3 g/cm^3 in case of In. Nevertheless, their orbital configuration make them interesting. The elements of the boron group exhibit a fully filled s-orbital and one electron in the d-orbital, relating them from the electronic configuration closer to the alkali metals than Mercury. This would lead to an investigation weather the deviation in the temperature dependence, as it was found in case of Hg, is also present in case of Ga and In melts.

Additionally, at least in case of Ga a liquid-liquid transition in the undercooled melt is found, which is accomplished to a changed density [302–304], where also changes in the melt dynamics are expected.

2. In the early transition metal group 4, where Zirconium is directly allocated under Titanium, there is a third element - namely Hafnium (with atomic number 72) - which also exhibits very similar chemical properties than Zr and Ti. Such, Hf pass through the same phase transition in the solid than Ti and Zr. In case of the crystalline β-phase, the phonon characteristics are similar for Ti, Zr and Hf [305, 306] and also the diffusion mechanism was found to be similar [307, 308]. Moreover, the Zr-Hf and the Ti-Hf phase diagrams are also completely miscible systems. Whereas the difference in melting temperature between Ti and Zr is only 90 K, the melting point of Hf is about 380 K higher than for Zr. But - and that makes Hf rather interesting - the atomic Goldschmidt radii in Hf and Zr are the same: $r_{Hf} = r_{Zr} = 1.60$ Å [67].

If assuming also an absence of chemical short-range order in Hf-containing metal group 4 binary systems, measured structure factors and also the melt dynamics should then show no concentration dependency.

That is why Zr can be substituted by Hf, e.g. to investigate the Hf self-diffusion in binary melts [63], where Zr itself exhibit a rather small incoherent scattering cross-section of $\sigma_{inc}(Zr) = 0.02$ barn (what is also the reason why on the Zr-rich side in the Zr-Ti system diffusion coefficients are missing in this work) [112]. In contrast, Hf has an incoherent scattering cross-section of $\sigma_{inc}(Hf) = 2.6$ barn [112]. This would allow to study an averaged Ti/Hf-diffusion in binary Hf-Ti-concentrations, since $\sigma_{inc}(Ti) = 2.87$ barn [112]. An access to values on the Hf-rich side in the Hf-Ti would be possible. However, investigations on the binary Zr-Hf system are required to determine whether those elements indeed can be substituted isomorphic. In addition, there is one great disadvantage: Hf is a strong absorber for neutrons $\sigma_{abs}(Hf) = 104.1$ barn [112], what would lower the collected statistics when using samples in electromagnetic levitation (which requires a certain sample size, especially at the high relevant temperatures). The high Z-number of Hf would also require higher energies in case of a x-ray scattering experiment.

Due to the similar coherent scattering lengths of Zr and Hf: $b_{coh}(Zr) = 7.16$ fm and $b_{coh}(Hf) = 7.76$ fm [112], a zero scattering binary Hf-Ti alloy with similar concentrations than the Zr-Ti zero scatterer $Zr_{32.4}Ti_{67.6}$ exists: $Hf_{30.9}Ti_{69.1}$. In case of a neutron diffraction experiment here the chemical short-range order could directly be investigated.

In their paper Jeon et. al also reported densities in the binary Zr-Hf system measured in ESL [273]. Here also a linear concentration dependency is found, which indicates the same argument concerning the excess volume and the binary packing for Hf-Ti, than for Zr-Ti in this work. Therefore, it would be interesting, whether the Zr-Hf binary system and the

Hf-Ti binary system also show similar (normalized) structure factors. In case of Zr-Hf the measured structure should then conform to the raw elements. However, the high relevant temperatures in Hf-containing melts yield some difficulties from an experimental point of view, since the high vapor pressure of Titanium would provoke an evaporation of the melt.

3. Ternary systems, which lead to investigate the dynamics of glass-forming melts, are subject of intensive research. Systems that enhance the glass-forming ability upon minor addition of a third element - like it is reported for $(Zr_{50}Cu_{50})_{96}(Ti,Al)_4$ - are Zr-Al-Ni [280], Ni-Nb-Sn [281], Ni-Nb-Fe [281], Ni-Nb-Cu [281] and Cu-Ti-Si [282]. Those ternary systems are all potential candidates to investigate the influence of minor additions on the glass-forming ability of binary melts. However, those systems show - already in the binary cases - different short-range orders than the investigated Zr-Cu system with minor Al and Ti additions, making reasonable relations rather challenging.

An example: The minor addition of Silicon to the $Cu_{54}Ti_{46}$ composition should enhance the glass-forming ability by decreasing the liquidus temperature and promoting the precipitation of the Cu_4Ti_3 phase instead of the γ-Cu-Ti during solidification [282]. However, it is not clear whether this effect is specific to Si and if it can be generalized to other elements. Additionally, melts containing semiconductors (like Si and Ge) can show structural changes (like indicated by a changed coordination number), which have an influence on the melt dynamics e.g. by increasing the self-diffusion coefficient [197, 309].

As depicted in Fig. 5.1 such effects can also be seen in case of the eutectic binary $Cu_{68}Si_{32}$, where due to the weak incoherent scattering cross-section of Si $\sigma_{inc}(Si) = 0.004$ barn [112] mostly the Cu-diffusion is investigated. However, an increased Cu-diffusivity is not found in case of the other eutectic composition of the Cu-Si system $Cu_{81}Si_{19}$, where the self-diffusion coefficient is decreased when compared to pure Cu, revealing a complex composition dependence in the Cu-Si system.

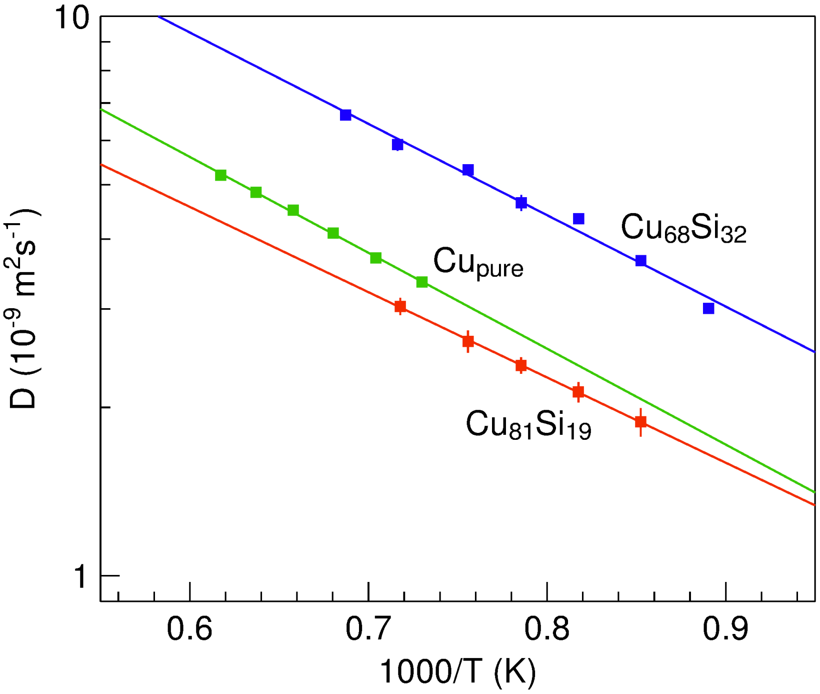

Figure 5.1: Self-diffusion coefficients measured by quasielastic neutron scattering for binary $Cu_{68}Si_{32}$ (blue) and $Cu_{81}Si_{19}$ (red) and compared to liquid pure Copper (green)[54]. The lines refer to Arrhenius fits of the measured values.

Appendices

A Diffusion coefficients

In the following the in this work measured diffusion coefficients are listed, sorted by the respective section.

A.1 Diffusion coefficients from section 4.1

Temperature	**Diffusion coefficient in 10^{-9} m^2s^{-1}**
350 K	2.29 ±0.09
320 K	2.04 ±0.08
300 K	1.83 ±0.06
280 K	1.60 ±0.10
260 K	1.39 ±0.08
240 K	1.25 ±0.07

Table 1: Self-diffusion coefficients of Mercury measured with quasielastic neutron scattering

A.2 Diffusion coefficients from section 4.2

Temperature	**Diffusion coefficient in 10^{-9} m^{2}s^{-1}**
1830 K	3.19 ±0.05
1897 K	3.54 ±0.03
1927 K	3.72 ±0.04
1987 K	3.95 ±0.07

Table 2: Self-diffusion coefficients of Zr_2Ti measured with quasielastic neutron scattering

Temperature	**Diffusion coefficient in 10^{-9} m^{2}s^{-1}**
1781 K	2.87 ±0.06
1870 K	3.38 ±0.04
1929 K	3.63 ±0.06
2004 K	3.95 ±0.05

Table 3: Self-diffusion coefficients of $Zr_{50}Ti_{50}$ measured with quasielastic neutron scattering

Temperature	**Diffusion coefficient in 10^{-9} m^{2}s^{-1}**
1790 K	3.17 ±0.05
1863 K	3.56 ±0.05
1907 K	3.79 ±0.04
1974 K	4.04 ±0.07

Table 4: Self-diffusion coefficients of $Zr_{32.4}Ti_{67.4}$ measured with quasielastic neutron scattering

Temperature	**Diffusion coefficient in 10^{-9} m^{2}s^{-1}**
1819 K	3.64 ±0.06
1893 K	4.04 ±0.03
1952 K	4.50 ±0.04
2020 K	4.91 ±0.06

Table 5: Self-diffusion coefficients of $Zr_{15}Ti_{85}$ measured with quasielastic neutron scattering

A.3 Diffusion coefficients from section 4.3

Temperature	**Diffusion coefficient in 10^{-9} m^2s^{-1}**
1116 K	0.64 ±0.06
1186 K	0.83 ±0.08
1251 K	1.16 ±0.10
1305 K	1.34 ±0.15

Table 6: Self-diffusion coefficients of $Zr_{50}Cu_{50}$ measured with quasielastic neutron scattering

Temperature	**Diffusion coefficient in 10^{-9} m^2s^{-1}**
1060 K	0.20 ±0.04
1096 K	0.26 ±0.03
1144 K	0.34 ±0.03
1192 K	0.53 ±0.03
1229 K	0.64 ±0.07
1278 K	1.09 ±0.09

Table 7: Self-diffusion coefficients of $(Zr_{50}Cu_{50})_{96}Al_4$ measured with quasielastic neutron scattering

Temperature	**Diffusion coefficient in 10^{-9} m^2s^{-1}**
1075 K	0.30 ±0.04
1135 K	0.43 ±0.04
1183 K	0.48 ±0.10
1247 K	0.75 ±0.15
1241 K	0.82 ±0.15

Table 8: Self-diffusion coefficients of $(Zr_{50}Cu_{50})_{96}Ti_4$ measured with quasielastic neutron scattering

B Viscosity Data

Below are the measured viscosity data as shown in section 4.3.2 listed for the respective alloys.

Temperature	**Viscosity in mPa s**
1307 K	19.8 ±0.6
1282 K	19.0 ±0.6
1255 K	20.4 ±0.9
1229 K	22.4 ±0.5
1204 K	23.3 ±0.7
1179 K	29.6 ±1.6
1153 K	38.0 ±1.6
1129 K	41.6 ±2.8
1104 K	43.4 ±1.7
1104 K	39.8 ±2.8
1079 K	57.4 ±3.8
1078 K	60.0 ±3.6
1054 K	71.2 ±4.1
1054 K	65.3 ±4.5
1028 K	108.7 ±8.0
1005 K	131.3 ±9.6
985 K	200.5 ±10.8
979 K	242.3 ±20.9

Table 9: Viscosity of $Zr_{50}Cu_{50}$ measured in electrostatic levitation employing the oscillated droplet method

Temperature	**Viscosity in mPa s**
1433 K	11.9 ±0.3
1413 K	12.1 ±0.7
1385 K	10.0 ±0.4
1364 K	14.3 ±0.6
1339 K	16.8 ±1.1
1313 K	14.2 ±0.4
1288 K	21.5 ±0.6
1268 K	20.9 ±0.7
1238 K	27.6 ±1.1
1223 K	33.7 ±1.7
1213 K	34.1 ±2.0
1196 K	30.5 ±0.9
1187 K	35.2 ±1.5
1184 K	34.6 ±0.8
1174 K	34.4 ±1.1
1164 K	39.8 ±1.1
1164 K	44.1 ±2.4
1154 K	43.6 ±1.1
1144 K	47.6 ±1.2
1135 K	52.8 ±1.7
1135 K	54.9 ±2.3
1124 K	62.5 ±1.7
1114 K	65.3 ±2.0
1113 K	71.4 ±4.4
1104 K	68.3 ±2.0
1094 K	77.4 ±2.6
1088 K	91.6 ±6.3
1084 K	91.2 ±3.9
1074 K	102.5 ±4.6
1064 K	116.4 ±9.8
1054 K	128.8 ±5.2
1044 K	153.4 ±10.3
1034 K	198.3 ±8.0
1034 K	204.0 ±23.8
1024 K	210.9 ±15.2
1014 K	268.4 ±17.2
1013 K	258.1 ±29.2
1004 K	388.6 ±25.3
994 K	457.0 ±28.2

Table 10: Viscosity of $(Zr_{50}Cu_{50})_{96}Al_4$ measured in electrostatic levitation employing the oscillated droplet method

Temperature	**Viscosity in mPa s**
1316 K	14.2 ±1.3
1316 K	14.8 ±0.4
1291 K	16.8 ±0.5
1291 K	15.4 ±0.3
1267 K	17.7 ±0.3
1266 K	20.2 ±0.6
1241 K	20.7 ±1.4
1239 K	19.6 ±0.7
1216 K	22.0 ±0.6
1216 K	21.0 ±0.6
1199 K	27.2 ±1.1
1193 K	30.2 ±1.0
1191 K	26.1 ±0.8
1166 K	32.1 ±1.0
1165 K	33.1 ±2.2
1141 K	38.3 ±1.4
1140 K	38.9 ±1.8
1126 K	42.0 ±1.7
1116 K	46.2 ±2.0
1097 K	55.1 ±2.5
1095 K	62.3 ±1.8
1091 K	57.3 ±3.0
1085 K	72.6 ±2.4
1076 K	73.8 ±4.6
1075 K	75.9 ±2.7
1065 K	87.8 ±2.8
1065 K	78.6 ±4.6
1056 K	84.6 ±5.2
1055 K	91.7 ±2.6
1045 K	100.2 ±2.9
1041 K	113.8 ±6.9
1035 K	107.3 ±3.7
1026 K	119.0 ±7.0
1025 K	114.5 ±3.5
1015 K	133.8 ±4.4
1015 K	151.7 ±12.8
1005 K	162.3 ±12.4
1005 K	152.2 ±6.0
995 K	172.1 ±6.4
985 K	178.0 ±7.7
975 K	223.5 ±10.0
965 K	268.2 ±10.2
955 K	292.8 ±12.6
945 K	373.5 ±15.6

Table 11: Viscosity of $(Zr_{50}Cu_{50})_{96}Ti_4$ measured in electrostatic levitation employing the oscillated droplet method

Bibliography

[1] A. Einstein, *Eine neue Bestimmung der Moleküldimensionen.* PhD thesis, Eidgenössische Technische Hochschule Zürich, 1905.

[2] T. Graham, “Flüssigkeits-Diffusion, angewandt auf Analyse,” *Annalen der Physik*, vol. 190, no. 9, pp. 187–192, 1861.

[3] G. Burkhardt, *Ueber die Transspiration reiner und mit verschiedenen Salzen versetzter Zuckerloesungen.* PhD thesis, Unversität zu Zürich, 1872.

[4] A. Einstein, “Berichtigung zu meiner Arbeit: „Eine neue Bestimmung der Moleküldimensionen”,” *Annalen der Physik*, vol. 339, no. 3, pp. 591–592, 1911.

[5] R. Brown, “XXVII. A brief account of microscopical observations made in the months of June, July and August 1827, on the particles contained in the pollen of plants; and on the general existence of active molecules in organic and inorganic bodies,” *The Philosophical Magazine*, vol. 4, no. 21, pp. 161–173, 1828.

[6] A. Einstein, “Über die von der molekularkinetischen Theorie der Wärme geforderte Bewegung von in ruhenden Flüssigkeiten suspendierten Teilchen,” *Annalen der Physik*, vol. 322, no. 8, pp. 549–560, 1905.

[7] H. Mehrer, *Diffusion in Solids: Fundamentals, Methods, Materials, Diffusion-Controlled Processes.* Springer Series in Solid-State Sciences, Springer Berlin Heidelberg, 2007.

[8] S. Burlatsky, G. Oshanin, and A. Ovchinnikov, “Kinetics of chemical short-range ordering in liquids and diffusion-controlled reactions,” *Chemical physics*, vol. 152, no. 1-2, pp. 13–21, 1991.

[9] V. Dybkov, “Reaction diffusion in heterogeneous binary systems,” *Journal of materials science*, vol. 21, no. 9, pp. 3078–3084, 1986.

[10] V. Dybkov, *Reaction diffusion and solid state chemical kinetics.* Trans Tech Publication, 2002.

[11] D. M. Herlach, "Solidification from undercooled melts," *Materials Science and Engineering: A*, vol. 226, pp. 348–356, 1997.

[12] C. Karrasch, *Solidification kinetics in undercooled pure iron and iron-boron alloys under different fluid flow conditions.* PhD thesis, Ruhr-Universität Bochum, 2016.

[13] R. Kobold, W. Kuang, H. Wang, W. Hornfeck, M. Kolbe, and D. M. Herlach, "Dendrite growth velocity in the undercooled melt of glass forming $Ni_{50}Zr_{50}$ compound," *Philosophical Magazine Letters*, vol. 97, no. 6, pp. 249–256, 2017.

[14] D. M. Herlach, R. Kobold, and S. Klein, "Crystal Nucleation and Growth in Undercooled Melts of Pure Zr, Binary Zr-Based and Ternary Zr-Ni-Cu Glass-Forming Alloys," *JOM*, vol. 70, no. 5, pp. 726–732, 2018.

[15] P. Danesi, E. Horwitz, G. Vandegrift, and R. Chiarizia, "Mass transfer rate through liquid membranes: interfacial chemical reactions and diffusion as simultaneous permeability controlling factors," *Separation science and Technology*, vol. 16, no. 2, pp. 201–211, 1981.

[16] G. Vogl, *Wandern ohne Ziel: von der Atomdiffusion zur Ausbreitung von Lebewesen und Ideen.* Springer, 2007.

[17] A. Bunde, J. Caro, J. Kärger, and G. Vogl, *Diffusive Spreading in Nature, Technology and Society.* Springer, 2017.

[18] S.-Y. Hong and H.-L. Pan, "Nonlocal boundary layer vertical diffusion in a medium-range forecast model," *Monthly Weather Review*, vol. 124, no. 10, pp. 2322–2339, 1996.

[19] P. J. Webster, A. M. Moore, J. P. Loschnigg, and R. R. Leben, "Coupled ocean–atmosphere dynamics in the Indian Ocean during 1997–98," *Nature*, vol. 401, no. 6751, pp. 356–360, 1999.

[20] N. L. Komarova and M. A. Nowak, "Language dynamics in finite populations," *Journal of Theoretical Biology*, vol. 221, no. 3, pp. 445–457, 2003.

[21] A. Kandler, R. Unger, and J. Steele, "Language shift, bilingualism and the future of Britain's Celtic languages," *Philosophical Transactions of the Royal Society B: Biological Sciences*, vol. 365, no. 1559, pp. 3855–3864, 2010.

[22] D. Brockmann, L. Hufnagel, and T. Geisel, “The scaling laws of human travel,” *Nature*, vol. 439, no. 7075, pp. 462–465, 2006.

[23] V. Belik, T. Geisel, and D. Brockmann, “The impact of human mobility on spatial disease dynamics,” in *2009 International Conference on Computational Science and Engineering*, vol. 4, pp. 932–935, IEEE, 2009.

[24] L. Hufnagel, D. Brockmann, and T. Geisel, “Forecast and control of epidemics in a globalized world,” *Proceedings of the National Academy of Sciences*, vol. 101, no. 42, pp. 15124–15129, 2004.

[25] B. F. Maier and D. Brockmann, “Effective containment explains subexponential growth in recent confirmed COVID-19 cases in China,” *Science*, 2020.

[26] “Coronavirus disease 2019 (COVID-19): situation report, 72,” *World Health Organization*, 2020.

[27] W. Petry, T. Flottmann, A. Heiming, J. Trampenau, M. Alba, and G. Vogl, “Atomistic study of anomalous self-diffusion in bcc β-titanium,” *Physical Review Letters*, vol. 61, no. 6, p. 722, 1988.

[28] G. Vogl, W. Petry, T. Flottmann, and A. Heiming, “Direct determination of the self-diffusion mechanism in bcc β-titanium,” *Physical Review B*, vol. 39, no. 8, p. 5025, 1989.

[29] M. Leitner, B. Sepiol, L.-M. Stadler, B. Pfau, and G. Vogl, “Atomic diffusion studied with coherent X-rays,” *Nature materials*, vol. 8, no. 9, p. 717, 2009.

[30] H. Schober, W. Petry, and J. Trampenau, “Migration enthalpies in FCC and BCC metals,” *Journal of Physics: Condensed Matter*, vol. 4, no. 47, p. 9321, 1992.

[31] S. Mantl, W. Petry, K. Schroeder, and G. Vogl, “Diffusion of iron in aluminum studied by Mössbauer spectroscopy,” *Physical Review B*, vol. 27, no. 9, p. 5313, 1983.

[32] K. H. Steinmetz, G. Vogl, W. Petry, and K. Schroeder, “Diffusion of iron in copper studied by Mössbauer spectroscopy on single crystals,” *Physical Review B*, vol. 34, no. 1, p. 107, 1986.

[33] R. Swalin, “On the theory of self-diffusion in liquid metals,” *Acta Metallurgica*, vol. 7, no. 11, pp. 736–740, 1959.

[34] N. H. Nachtrieb, "Self-diffusion in liquid metals," *Advances in Physics*, vol. 16, no. 62, pp. 309–323, 1967.

[35] P. Ascarelli and A. Paskin, "Dense-gas formulation of self-diffusion of liquid metals," *Physical Review*, vol. 165, no. 1, p. 222, 1968.

[36] P. Protopapas, H. C. Andersen, and N. Parlee, "Theory of transport in liquid metals. I. Calculation of self-diffusion coefficients," *The Journal of Chemical Physics*, vol. 59, no. 1, pp. 15–25, 1973.

[37] R. Chhabra and T. Sridhar, "Temperature dependence of self diffusion in liquid metals," *Physics and Chemistry of Liquids an International Journal*, vol. 13, no. 1, pp. 37–46, 1983.

[38] G. Kaptay, "A new theoretical equation for temperature dependent self-diffusion coefficients of pure liquid metals," *International Journal of Materials Research*, vol. 99, no. 1, pp. 14–17, 2008.

[39] J. Rohlin and A. Lodding, "Self-diffusion in molten potassium metal," *Zeitschrift für Naturforschung*, vol. 17, 1962.

[40] J. Murday and R. M. Cotts, "Self-diffusion coefficient of liquid lithium," *The Journal of Chemical Physics*, vol. 48, no. 11, pp. 4938–4945, 1968.

[41] E. F. Broome and H. Walls, "Self-diffusion measurements in liquid gallium," *Transactions of the Metallurgical Society of AIME*, vol. 245, no. 4, pp. 739–741, 1969.

[42] J. Foster and R. Reynik, "Self-diffusion in liquid tin and indium over extensive temperature ranges," *Metallurgical Transactions*, vol. 4, no. 1, pp. 207–216, 1973.

[43] G. Mathiak, A. Griesche, K. Kraatz, and G. Frohberg, "Diffusion in liquid metals," *Journal of Non-Crystalline Solids*, vol. 205, pp. 412–416, 1996.

[44] R. M. Banish and L. B. Jalbert, "In-situ diffusivity measurement technique," *Advances in Space Research*, vol. 24, no. 10, pp. 1311–1320, 1999.

[45] M. Bee, *Quasielastic neutron scattering. Principles and applications in solid state chemistry, biology and materials science.* Adam Hilger, Bristol, 1988.

[46] G. L. Squires and J. W. Lynn, "Introduction to the theory of thermal neutron scattering," *Physics Today*, vol. 32, p. 69, 1979.

[47] S. W. Lovesey, *Theory of Neutron Scattering from Condensed Matter. Vol. 1: Nuclear Scattering.* Oxford, 1984.

[48] A. Furrer, J. F. Mesot, and T. Strässle, *Neutron scattering in condensed matter physics.* World Scientific Publishing Company, 2009.

[49] Z. Evenson, F. Yang, G. G. Simeoni, and A. Meyer, "Self-diffusion and microscopic dynamics in a gold-silicon liquid investigated with quasielastic neutron scattering," *Applied Physics Letters*, vol. 108, no. 12, p. 121902, 2016.

[50] A. Meyer, "The measurement of self-diffusion coefficients in liquid metals with quasielastic neutron scattering," in *EPJ Web of Conferences*, vol. 83, p. 01002, EDP Sciences, 2015.

[51] T. Bodensteiner, C. Morkel, W. Gläser, and B. Dorner, "Collective dynamics in liquid cesium near the melting point," *Physical Review A*, vol. 45, no. 8, p. 5709, 1992.

[52] F. Demmel, D. Szubrin, W.-C. Pilgrim, and C. Morkel, "Diffusion in liquid aluminium probed by quasielastic neutron scattering," *Physical Review B*, vol. 84, no. 1, p. 014307, 2011.

[53] F. Kargl, H. Weis, T. Unruh, and A. Meyer, "Self diffusion in liquid aluminium," in *Journal of Physics: Conference Series*, vol. 340, p. 012077, IOP Publishing, 2012.

[54] A. Meyer, "Self-diffusion in liquid copper as seen by quasielastic neutron scattering," *Physical Review B*, vol. 81, no. 1, p. 012102, 2010.

[55] A. Meyer, L. Hennig, F. Kargl, and T. Unruh, "Iron self diffusion in liquid pure iron and iron-carbon alloys," *Journal of Physics: Condensed Matter*, vol. 31, p. 395401, jul 2019.

[56] H. Weis, F. Kargl, M. Kolbe, M. Koza, T. Unruh, and A. Meyer, "Self-and inter-diffusion in dilute liquid germanium-based alloys," *Journal of Physics: Condensed Matter*, vol. 31, no. 45, p. 455101, 2019.

[57] A. Meyer, S. Stüber, D. Holland-Moritz, O. Heinen, and T. Unruh, "Determination of self-diffusion coefficients by quasielastic neutron scattering measurements of levitated Ni droplets," *Physical Review B*, vol. 77, no. 9, p. 092201, 2008.

[58] S. M. Chathoth, A. Meyer, M. Koza, and F. Juranyi, “Atomic diffusion in liquid Ni, NiP, PdNiP, and PdNiCuP alloys,” *Applied Physics Letters*, vol. 85, no. 21, pp. 4881–4883, 2004.

[59] F. Yang, D. Holland-Moritz, J. Gegner, P. Heintzmann, F. Kargl, C. Yuan, G. Simeoni, and A. Meyer, “Atomic dynamics in binary Zr-Cu liquids,” *EPL (Europhysics Letters)*, vol. 107, no. 4, p. 46001, 2014.

[60] S. Stüber, D. Holland-Moritz, T. Unruh, and A. Meyer, “Ni self-diffusion in refractory Al-Ni melts,” *Physical Review B*, vol. 81, no. 2, p. 024204, 2010.

[61] S. Das, J. Horbach, M. Koza, S. Mavila Chatoth, and A. Meyer, “Influence of chemical short-range order on atomic diffusion in Al–Ni melts,” *Applied Physics Letters*, vol. 86, no. 1, p. 011918, 2005.

[62] C. Yuan, F. Yang, F. Kargl, D. Holland-Moritz, G. Simeoni, and A. Meyer, “Atomic dynamics in Zr-(Co,Ni)-Al metallic glass-forming liquids,” *Physical Review B*, vol. 91, no. 21, p. 214203, 2015.

[63] B. Nowak, D. Holland-Moritz, F. Yang, T. Voigtmann, Z. Evenson, T. Hansen, and A. Meyer, “Effect of component substitution on the atomic dynamics in glass-forming binary metallic melts,” *Physical Review B*, vol. 96, no. 5, p. 054201, 2017.

[64] B. Nowak, D. Holland-Moritz, F. Yang, T. Voigtmann, T. Kordel, T. Hansen, and A. Meyer, “Partial structure factors reveal atomic dynamics in metallic alloy melts,” *Physical Review Materials*, vol. 1, no. 2, p. 025603, 2017.

[65] T. Schenk, D. Holland-Moritz, V. Simonet, R. Bellissent, and D. Herlach, “Icosahedral short-range order in deeply undercooled metallic melts,” *Physical Review Letters*, vol. 89, no. 7, p. 075507, 2002.

[66] D. Holland-Moritz, O. Heinen, R. Bellissent, and T. Schenk, “Short-range order of stable and undercooled liquid titanium,” *Materials Science and Engineering: A*, vol. 449, pp. 42–45, 2007.

[67] L. Pauling, “Atomic radii and interatomic distances in metals,” *Journal of the American Chemical Society*, vol. 69, no. 3, pp. 542–553, 1947.

[68] W. Gotze and L. Sjogren, “Relaxation processes in supercooled liquids,” *Reports on progress in Physics*, vol. 55, no. 3, p. 241, 1992.

[69] D. M. Wroughton and O. E. Carl, “Magnetic levitation and heating of conductive materials,” Aug. 17 1954. US Patent 2,686,864.

[70] D. Holland-Moritz, T. Schenk, P. Convert, T. Hansen, and D. Herlach, “Electromagnetic levitation apparatus for diffraction investigations on the short-range order of undercooled metallic melts,” *Measurement Science and Technology*, vol. 16, no. 2, p. 372, 2005.

[71] D. Holland-Moritz, T. Schenk, R. Bellissent, V. Simonet, K. Funakoshi, J. Merino, T. Buslaps, and S. Reutzel, “Short-range order in undercooled Co melts,” *Journal of Non-Crystalline Solids*, vol. 312, pp. 47–51, 2002.

[72] T. Schenk, V. Simonet, D. Holland-Moritz, R. Bellissent, T. Hansen, P. Convert, and D. Herlach, “Temperature dependence of the chemical short-range order in undercooled and stable Al-Fe-Co liquids,” *EPL (Europhysics Letters)*, vol. 65, no. 1, p. 34, 2004.

[73] D. Holland-Moritz, S. Stüber, H. Hartmann, T. Unruh, and A. Meyer, “Ni self-diffusion in Zr-Ni(-Al) melts,” in *Journal of Physics: Conference Series*, vol. 144, p. 012119, IOP Publishing, 2009.

[74] D. Ma, H. Cao, L. Ding, Y. A. Chang, K. Hsieh, and Y. Pan, “Bulkier glass formability enhanced by minor alloying additions,” *Applied Physics Letters*, vol. 87, no. 17, p. 171914, 2005.

[75] Q. Wang, C. Liu, Y. Yang, J. Liu, Y. Dong, and J. Lu, “The atomic-scale mechanism for the enhanced glass-forming-ability of a Cu-Zr based bulk metallic glass with minor element additions,” *Scientific reports*, vol. 4, p. 4648, 2014.

[76] D. Xu, G. Duan, and W. L. Johnson, “Unusual glass-forming ability of bulk amorphous alloys based on ordinary metal copper,” *Physical Review Letters*, vol. 92, no. 24, p. 245504, 2004.

[77] W. H. Wang, “Roles of minor additions in formation and properties of bulk metallic glasses,” *Progress in Materials Science*, vol. 52, no. 4, pp. 540–596, 2007.

[78] J. H. Na, M. D. Demetriou, M. Floyd, A. Hoff, G. R. Garrett, and W. L. Johnson, “Compositional landscape for glass formation in metal alloys,” *Proceedings of the National Academy of Sciences*, vol. 111, no. 25, pp. 9031–9036, 2014.

[79] P. Yu, H. Bai, M. Tang, and W. Wang, “Excellent glass-forming ability in simple $Cu_{50}Zr_{50}$-based alloys,” *Journal of Non-Crystalline Solids*, vol. 351, no. 14-15, pp. 1328–1332, 2005.

[80] B. Nowak, D. Holland-Moritz, F. Yang, Z. Evenson, and A. Meyer, “Mixing effects in a ternary Hf-Zr-Ni metallic melt,” *Physical Review B*, vol. 97, no. 9, p. 094202, 2018.

[81] D. Holland-Moritz, B. Nowak, F. Yang, and A. Meyer, “Structure and dynamics of glass-forming alloy melts investigated by application of levitation techniques,” *Pure and Applied Chemistry*, vol. 91, no. 6, pp. 895–910, 2019.

[82] J. Brillo, A. Pommrich, and A. Meyer, “Relation between Self-Diffusion and Viscosity in Dense Liquids: New Experimental Results from Electrostatic Levitation,” *Physical Review Letters*, vol. 107, no. 16, p. 165902, 2011.

[83] N. Mauro, M. Blodgett, M. Johnson, A. Vogt, and K. Kelton, “A structural signature of liquid fragility,” *Nature communications*, vol. 5, p. 4616, 2014.

[84] H. Yoo, C. Park, S. Jeon, S. Lee, and G. W. Lee, “Uncertainty evaluation for density measurements of molten Ni, Zr, Nb and Hf by using a containerless method,” *Metrologia*, vol. 52, no. 5, p. 677, 2015.

[85] P. Heintzmann, F. Yang, S. Schneider, G. Lohöfer, and A. Meyer, “Viscosity measurements of metallic melts using the oscillating drop technique,” *Applied Physics Letters*, vol. 108, no. 24, p. 241908, 2016.

[86] A. Fick, “Ueber diffusion,” *Annalen der Physik*, vol. 170, no. 1, pp. 59–86, 1855.

[87] J. C. Maxwell, “XV. On the dynamical theory of gases,” *The London, Edinburgh, and Dublin Philosophical Magazine and Journal of Science*, vol. 35, no. 235, pp. 129–145, 1868.

[88] J. Crank, *The mathematics of diffusion.* Oxford University Press, 1979.

[89] T. Springer and R. Lechner, *Diffusion in condensed matter*, vol. 1. Springer New York, 2005.

[90] P. Heitjans and J. Kärger, *Diffusion in condensed matter: methods, materials, models.* Springer Science & Business Media, 2006.

[91] H. C. Andersen, “Self-diffusion,” in *Time-Dependent Statistical Mechanics*, Stanford University Press, 2009.

[92] R. M. Moon and H. G. Smith, “Clifford Glenwood Shull 1915–2001,” *Acta Crystallographica Section A: Foundations of Crystallography*, vol. 58, no. 1, pp. 1–3, 2002.

[93] M. Tanabashi, P. D. Group, *et al.*, “Review of particle properties,” *Physical Review D*, vol. 98, p. 030001, 2018.

[94] A. Czarnecki, W. J. Marciano, and A. Sirlin, “Neutron lifetime and axial coupling connection,” *Physical Review Letters*, vol. 120, no. 20, p. 202002, 2018.

[95] J. Chadwick, “Possible existence of a neutron,” *Nature*, vol. 129, no. 3252, pp. 312–312, 1932.

[96] G. Knoll, “Radioisotope neutron sources,” in *Neutron sources for basic physics and applications*, 1983.

[97] F. Coensgen, T. Casper, D. Correll, C. Damm, A. Futch, B. Logan, A. Molvik, and C. Walter, “Beam plasma neutron sources based on beam-driven mirror,” *Journal of Fusion Energy*, vol. 8, no. 3-4, pp. 237–247, 1989.

[98] G. Clark, “Neutron sources,” Dec. 10 1957. US Patent 2,816,242.

[99] J. M. Carpenter and W. B. Yelon, “2. Neutron Sources,” in *Methods in Experimental Physics*, vol. 23, pp. 99–196, Elsevier, 1986.

[100] L. Meitner, O. Hahn, and F. Straßmann, “Über die Umwandlungsreihen des Urans, die durch Neutronenbestrahlung erzeugt werden,” *Zeitschrift für Physik*, vol. 106, no. 3-4, pp. 249–270, 1937.

[101] O. Hahn and F. Strassmann, “Über den Nachweis und das Verhalten der bei der Bestrahlung des Urans mittels Neutronen entstehenden Erdalkalimetalle,” *Naturwissenschaften*, vol. 27, no. 1, pp. 11–15, 1939.

[102] J. J. Duderstadt, *Nuclear reactor analysis.* Wiley, 1976.

[103] J. M. Carpenter, “Pulsed spallation neutron sources for slow neutron scattering,” *Nuclear Instruments and Methods*, vol. 145, no. 1, pp. 91–113, 1977.

[104] D. Habs, M. Gross, P. Thirolf, and P. Böni, “Neutron halo isomers in stable nuclei and their possible application for the production of low energy, pulsed, polarized neutron beams of high intensity and high brilliance,” *Applied Physics B*, vol. 103, no. 2, pp. 485–499, 2011.

[105] J. Alvarez, J. Fernández-Tobias, K. Mima, S. Nakai, S. Kar, Y. Kato, and J. Perlado, “Laser driven neutron sources: characteristics, applications and prospects,” *Physics Procedia*, vol. 60, pp. 29–38, 2014.

[106] P. Böni and W. Petry, “Neutron Science with Highly Brilliant Beams,” in *Applications of Laser-Driven Particle Acceleration*, pp. 315–332, CRC Press, 2018.

[107] G. Roth, “Diffraction,” *Lecture Notes of the 43rd IFF Spring School “Scattering Methods for Condensed Matter Research: Towards Novel Applications at Future Sources", M. Angst, T. Brückel, D. Richter, and R. Zorn, Eds. Jülich,*, 2012.

[108] S. Blügel, “Scattering Theory: Born Series,” *Lecture Notes of the 43rd IFF Spring School “Scattering Methods for Condensed Matter Research: Towards Novel Applications at Future Sources", M. Angst, T. Brückel, D. Richter, and R. Zorn, Eds. Jülich,*, 2012.

[109] L. De Broglie, “The wave nature of the electron,” *Nobel lecture*, vol. 12, pp. 244–256, 1929.

[110] W. L. Bragg, “The diffraction of short electromagnetic waves by a crystal,” *Scientia*, vol. 23, no. 45, 1929.

[111] A. Einstein, “Zur Quantentheorie der Strahlung,” *Physikalische Zeitschrift*, vol. 18, pp. 121–128, 1917.

[112] V. F. Sears, “Neutron scattering lengths and cross sections,” *Neutron news*, vol. 3, no. 3, pp. 26–37, 1992.

[113] L. Van Hove, “Correlations in space and time and Born approximation scattering in systems of interacting particles,” *Physical Review*, vol. 95, no. 1, p. 249, 1954.

[114] M. A. Gonzalez, “Quasielastic Neutron Scattering,” in *Seiminar talk Inst. Laue Langevin (ILL), Grenoble, France*, 2007.

[115] B. Brockhouse, “Diffusive motions in liquids and neutron scattering,” *Physical Review Letters*, vol. 2, no. 7, p. 287, 1959.

[116] B. Brockhouse and N. Pope, “Time-dependent pair correlations in liquid lead,” *Physical Review Letters*, vol. 3, no. 6, p. 259, 1959.

[117] B. Brockhouse, *Inelastic scattering of neutrons in solids and liquids: Proceedings of the symposium on inelastic scattering of neutrons in solids and liquids. Sponsored by the International atomic energy agency held in Vienna, 11-14 October 1960.* International atomic energy agency, 1961.

[118] J.-P. Hansen and I. R. McDonald, *Theory of simple liquids.* Elsevier, 1990.

[119] K. Singwi and A. Sjölander, “Diffusive motions in water and cold neutron scattering,” *Physical Review*, vol. 119, no. 3, p. 863, 1960.

[120] G. Williams and D. C. Watts, “Non-symmetrical dielectric relaxation behaviour arising from a simple empirical decay function,” *Transactions of the Faraday society*, vol. 66, pp. 80–85, 1970.

[121] T. Faber and J. Ziman, “A theory of the electrical properties of liquid metals: III. The resistivity of binary alloys,” *Philosophical Magazine*, vol. 11, no. 109, pp. 153–173, 1965.

[122] A. Bhatia and D. Thornton, “Structural aspects of the electrical resistivity of binary alloys,” *Physical Review B*, vol. 2, no. 8, p. 3004, 1970.

[123] “Properties of the Neutron.” http://pd.chem.ucl.ac.uk/pdnn/inst3/neutrons.htm, 2020. Birkbeck College, University of London.

[124] F. C. Frank, “Supercooling of liquids,” *Proceedings of the Royal Society of London. Series A. Mathematical and Physical Sciences*, vol. 215, no. 1120, pp. 43–46, 1952.

[125] D. Turnbull, “Formation of crystal nuclei in liquid metals,” *Journal of Applied Physics*, vol. 21, no. 10, pp. 1022–1028, 1950.

[126] V. Simonet, F. Hippert, M. Audier, and R. Bellissent, “Local order in liquids forming quasicrystals and approximant phases,” *Physical Review B*, vol. 65, no. 2, p. 024203, 2001.

[127] D. Holland-Moritz, F. Yang, J. Gegner, T. Hansen, M. D. Ruiz-Martín, and A. Meyer, “Structural aspects of glass-formation in Ni-Nb melts,” *Journal of Applied Physics*, vol. 115, no. 20, p. 203509, 2014.

[128] S. Gruner, J. Marczinke, L. Hennet, W. Hoyer, and G. Cuello, “On the atomic structure of liquid Ni–Si alloys: a neutron diffraction study,” *Journal of Physics: Condensed Matter*, vol. 21, no. 38, p. 385403, 2009.

[129] D. Holland-Moritz, S. Stüber, H. Hartmann, T. Unruh, T. Hansen, and A. Meyer, “Structure and dynamics of liquid $Ni_{36}Zr_{64}$ studied by neutron scattering,” *Physical Review B*, vol. 79, no. 6, p. 064204, 2009.

[130] M. Stolpe, I. Jonas, S. Wei, Z. Evenson, W. Hembree, F. Yang, A. Meyer, and R. Busch, “Structural changes during a liquid-liquid transition in the deeply undercooled $Zr_{58.5}Cu_{15.6}Ni_{12.8}Al_{10.3}Nb_{2.8}$ bulk metallic glass forming melt,” *Physical Review B*, vol. 93, no. 1, p. 014201, 2016.

[131] S. Wei, M. Stolpe, O. Gross, W. Hembree, S. Hechler, J. Bednarcik, R. Busch, and P. Lucas, “Structural evolution on medium-range-order during the fragile-strong transition in $Ge_{15}Te_{85}$,” *Acta Materialia*, vol. 129, pp. 259–267, 2017.

[132] N. Jakse and A. Pasturel, “Dynamic properties and local order in liquid Al-Ni alloys,” *Applied Physics Letters*, vol. 105, no. 13, p. 131905, 2014.

[133] J.-F. Wax, M. Johnson, L. Bove, and M. Mihalkovič, “Multiscale study of the influence of chemical order on the properties of liquid Li-Bi alloys,” *Physical Review B*, vol. 83, no. 14, p. 144203, 2011.

[134] L. Xiong, K.Chen, F.S.Ke, H.B.Lou, G.Q.Yue, B.Shen, F.Dong, S.Y.Wang, L.Y.Chen, C.Z.Wang, K.M.Ho, X.D.Wang, L.H.Lai, H.L.Xie, T.Q.Xiao, and J.Z.Jiang, “Structural and dynamical properties of liquid $Ag_{74}Ge_{26}$ alloy studied by experiments and ab initio molecular dynamics simulation,” *Acta Materialia*, vol. 92, pp. 109–116, 2015.

[135] L. Huang, C. Wang, and K. Ho, “Structure and dynamics of liquid $Ni_{36}Zr_{64}$ by ab initio molecular dynamics,” *Physical Review B*, vol. 83, no. 18, p. 184103, 2011.

[136] W. Wang, J. Han, H. Fang, J. Wang, Y. Liang, S. Shang, Y. Wang, X. Liu, L. Kecskes, S. Mathaudhu, X. Hui, and Z. Liu, “Anomalous structural dynamics in liquid $Al_{80}Cu_{20}$: An ab initio molecular dynamics study,” *Acta Materialia*, vol. 97, pp. 75–85, 2015.

[137] C. J. Smithells and E. A. Brandes, *Smithells metals reference book*. Butterworth, 1992.

[138] C. Yuan, F. Yang, X. Xi, C. Shi, D. Holland-Moritz, M. Li, F. Hu, B. Shen, X. Wang, A. Meyer, and W. Wang, “Impact of hybridization on metallic-glass formation and design,” *Materials Today*, vol. 32, pp. 26–34, 2020.

[139] W. Götze, “Recent tests of the mode-coupling theory for glassy dynamics,” *Journal of Physics: Condensed Matter*, vol. 11, no. 10A, p. A1, 1999.

[140] W. Kob, “Computer simulations of supercooled liquids and glasses,” *Journal of Physics: Condensed Matter*, vol. 11, no. 10, p. R85, 1999.

[141] A. Meyer, “Atomic transport in dense multicomponent metallic liquids,” *Physical Review B*, vol. 66, no. 13, p. 134205, 2002.

[142] T. Voigtmann, A. Meyer, D. Holland-Moritz, S. Stüber, T. Hansen, and T. Unruh, “Atomic diffusion mechanisms in a binary metallic melt,” *EPL (Europhysics Letters)*, vol. 82, no. 6, p. 66001, 2008.

[143] P. Kuhn, J. Horbach, F. Kargl, A. Meyer, and T. Voigtmann, “Diffusion and interdiffusion in binary metallic melts,” *Physical Review B*, vol. 90, no. 2, p. 024309, 2014.

[144] W. Götze and T. Voigtmann, “Statistische Physik: Ideale Glasübergänge: Die Modenkopplungstheorie beschreibt die Dynamik glasbildender Systeme,” *Physikalische Blätter*, vol. 57, no. 4, pp. 41–47, 2001.

[145] W. Götze, *Complex dynamics of glass-forming liquids: A mode-coupling theory*, vol. 143. Oxford University Press, 2008.

[146] J. Brillo, *Thermophysical properties of multicomponent liquid alloys.* Walter de Gruyter GmbH & Co KG, 2016.

[147] A. Einstein, *Investigations on the Theory of the Brownian Movement.* Courier Corporation, 1956.

[148] G. G. Stokes, *On the effect of the internal friction of fluids on the motion of pendulums*, vol. 9. Cambridge University Press, 1901.

[149] H. Parkhurst Jr and J. Jonas, “Dense liquids. II. The effect of density and temperature on viscosity of tetramethylsilane and benzene,” *The Journal of Chemical Physics*, vol. 63, no. 6, pp. 2705–2709, 1975.

[150] P. Bordat, F. Affouard, M. Descamps, and F. Müller-Plathe, "The breakdown of the Stokes–Einstein relation in supercooled binary liquids," *Journal of Physics: Condensed Matter*, vol. 15, no. 32, p. 5397, 2003.

[151] A. Meyer, W. Petry, M. Koza, and M.-P. Macht, "Fast diffusion in ZrTiCuNiBe melts," *Applied Physics Letters*, vol. 83, no. 19, pp. 3894–3896, 2003.

[152] S. R. Becker, P. H. Poole, and F. W. Starr, "Fractional Stokes-Einstein and Debye-Stokes-Einstein relations in a network-forming liquid," *Physical Review Letters*, vol. 97, no. 5, p. 055901, 2006.

[153] S. K. Kumar, G. Szamel, and J. F. Douglas, "Nature of the breakdown in the Stokes-Einstein relationship in a hard sphere fluid," *The Journal of Chemical Physics*, vol. 124, no. 21, p. 214501, 2006.

[154] F. Affouard, M. Descamps, L.-C. Valdes, J. Habasaki, P. Bordat, and K. Ngai, "Breakdown of the Stokes–Einstein relation in Lennard-Jones glassforming mixtures with different interaction potential," *The Journal of Chemical Physics*, vol. 131, no. 10, p. 104510, 2009.

[155] F. Demmel and A. Tani, "Stokes-Einstein relation of the liquid metal rubidium and its relationship to changes in the microscopic dynamics with increasing temperature," *Physical Review E*, vol. 97, no. 6, p. 062124, 2018.

[156] S. Zimmermann, *Untersuchung der Zusammenhänge von Selbstdiffusion und Viskosität in flüssigen metallischen Schmelzen.* PhD thesis, Ruhr-Universität Bochum, 2018.

[157] A. Bartsch, K. Rätzke, A. Meyer, and F. Faupel, "Dynamic arrest in multicomponent glass-forming alloys," *Physical Review Letters*, vol. 104, no. 19, p. 195901, 2010.

[158] D. A. Winborne, P. C. Nordine, D. E. Rosner, and N. F. Marley, "Aerodynamic levitation technique for containerless high temperature studies on liquid and solid samples," *Metallurgical and Materials Transactions B*, vol. 7, no. 4, pp. 711–713, 1976.

[159] L. Hennet, I. Pozdnyakova, A. Bytchkov, V. Cristiglio, P. Palleau, H. E. Fischer, G. J. Cuello, M. Johnson, P. Melin, D. Zanghi, S. Brassamin, J.-F. Brun, D. L. Price, and M.-L. Saboungi, "Levitation apparatus for neutron diffraction investigations on

high temperature liquids," *Review of Scientific Instruments*, vol. 77, no. 5, p. 053903, 2006.

[160] W.-K. Rhim, S. K. Chung, D. Barber, K. F. Man, G. Gutt, A. Rulison, and R. E. Spjut, "An electrostatic levitator for high-temperature containerless materials processing in 1-g," *Review of Scientific Instruments*, vol. 64, no. 10, pp. 2961–2970, 1993.

[161] T. Meister, *Aufbau und Regelung eines elektrostatischen Positionierers*. PhD thesis, Ruhr-Universität Bochum, 2000.

[162] J. Brillo and I. Egry, "Density determination of liquid copper, nickel, and their alloys," *International Journal of Thermophysics*, vol. 24, no. 4, pp. 1155–1170, 2003.

[163] L. Hennet, D. H. Moritz, R. Weber, and A. Meyer, "High-temperature levitated materials," in *Experimental Methods in the Physical Sciences*, vol. 49, pp. 583–636, Elsevier, 2017.

[164] P.-F. Paradis, T. Ishikawa, G.-W. Lee, D. Holland-Moritz, J. Brillo, W.-K. Rhim, and J. T. Okada, "Materials properties measurements and particle beam interactions studies using electrostatic levitation," *Materials Science and Engineering: R: Reports*, vol. 76, pp. 1–53, 2014.

[165] S. Wei, F. Yang, J. Bednarcik, I. Kaban, O. Shuleshova, A. Meyer, and R. Busch, "Liquid–liquid transition in a strong bulk metallic glass-forming liquid," *Nature communications*, vol. 4, no. 1, pp. 1–9, 2013.

[166] V. Wessels, A. Gangopadhyay, K. Sahu, R. Hyers, S. Canepari, J. Rogers, M. J. Kramer, A. Goldman, D. Robinson, J. W. Lee, J. Morris, and K. Kelton, "Rapid chemical and topological ordering in supercooled liquid $Cu_{46}Zr_{54}$," *Physical Review B*, vol. 83, no. 9, p. 094116, 2011.

[167] J. Brillo and I. Egry, "Density and excess volume of liquid copper, nickel, iron, and their binary alloys," *Zeitschrift für Metallkunde*, vol. 95, no. 8, pp. 691–697, 2004.

[168] J. Brillo, I. Egry, and J. Westphal, "Density and thermal expansion of liquid binary Al–Ag and Al–Cu alloys," *International Journal of Materials Research*, vol. 99, no. 2, pp. 162–167, 2008.

[169] J. J. Li, W. Rhim, C. Kim, K. Samwer, and W. Johnson, "Evidence for a liquid–liquid phase transition in metallic fluids observed by electrostatic levitation," *Acta Materialia*, vol. 59, no. 5, pp. 2166–2171, 2011.

[170] S. Mukherjee, H.-G. Kang, W. Johnson, and W.-K. Rhim, "Noncontact measurement of crystallization behavior, specific volume, and viscosity of bulk glass-forming Zr-Al-Co-(Cu) alloys," *Physical Review B*, vol. 70, no. 17, p. 174205, 2004.

[171] S. Mukherjee, J. Schroers, Z. Zhou, W. Johnson, and W.-K. Rhim, "Viscosity and specific volume of bulk metallic glass-forming alloys and their correlation with glass forming ability," *Acta Materialia*, vol. 52, no. 12, pp. 3689–3695, 2004.

[172] S. Mukherjee, W. Johnson, and W. Rhim, "Noncontact measurement of high-temperature surface tension and viscosity of bulk metallic glass-forming alloys using the drop oscillation technique," *Applied Physics Letters*, vol. 86, no. 1, p. 014104, 2005.

[173] W.-K. Rhim, K. Ohsaka, P.-F. Paradis, and R. E. Spjut, "Noncontact technique for measuring surface tension and viscosity of molten materials using high temperature electrostatic levitation," *Review of Scientific Instruments*, vol. 70, no. 6, pp. 2796–2801, 1999.

[174] P.-F. Paradis, T. Ishikawa, and S. Yoda, "Non-contact measurements of surface tension and viscosity of niobium, zirconium, and titanium using an electrostatic levitation furnace," *International Journal of Thermophysics*, vol. 23, no. 3, pp. 825–842, 2002.

[175] R. Busch, Y. Kim, W. Johnson, A. Rulison, W. Rhim, and D. Isheim, "Hemispherical total emissivity and specific heat capacity of deeply undercooled $Zr_{41.2}Ti_{13.8}Cu_{12.5}Ni_{10.0}Be_{22.5}$ melts," *Applied Physics Letters*, vol. 66, no. 23, pp. 3111–3113, 1995.

[176] J. Bendert, M. Blodgett, A. Gangopadhyay, and K. Kelton, "Measurements of volume, thermal expansion, and specific heat in $Zr_{57}Cu_{15.4}Ni_{12.6}Al_{10}Nb_5$ and $Zr_{58.5}Cu_{15.6}Ni_{12.8}Al_{10.3}Nb_{2.8}$ liquids and glasses," *Applied Physics Letters*, vol. 102, no. 21, p. 211913, 2013.

[177] D. M. Herlach, T. Palberg, I. Klassen, S. Klein, and R. Kobold, "Overview: Experimental studies of crystal nucleation: Metals and colloids," *The Journal of Chemical Physics*, vol. 145, no. 21, p. 211703, 2016.

[178] W. Hornfeck, R. Kobold, M. Kolbe, M. Conrad, and D. Herlach, “Quasicrystal nucleation and Z module twin growth in an intermetallic glass-forming system,” *Nature communications*, vol. 9, no. 1, p. 4054, 2018.

[179] R. Kobold, M. Kolbe, W. Hornfeck, and D. Herlach, “Nucleation study for an undercooled melt of intermetallic NiZr,” *The Journal of Chemical Physics*, vol. 148, no. 11, p. 114502, 2018.

[180] Q. Wang, L.-M. Wang, M. Ma, S. Binder, T. Volkmann, D. Herlach, J. Wang, Q. Xue, Y. Tian, and R. Liu, “Diffusion-controlled crystal growth in deeply undercooled melt on approaching the glass transition,” *Physical Review B*, vol. 83, no. 1, p. 014202, 2011.

[181] H. Wang, D. Herlach, and R. Liu, “Dendrite growth in $Cu_{50}Zr_{50}$ glass-forming melts, thermodynamics vs. kinetics,” *EPL (Europhysics Letters)*, vol. 105, no. 3, p. 36001, 2014.

[182] S. Klein and D. Herlach, “Crystal nucleation in undercooled melts of $PdZr_2$,” *Journal of Applied Physics*, vol. 114, no. 18, p. 183510, 2013.

[183] P. Fopp, W. Hornfeck, F. Kargl, M. Kolbe, and R. Kobold, “Unexpected behaviour of the crystal growth velocity at the hypercooling limit,” *arXiv preprint arXiv:1807.02507*, 2018.

[184] T. Kordel, D. Holland-Moritz, F. Yang, J. Peters, T. Unruh, T. Hansen, and A. Meyer, “Neutron scattering experiments on liquid droplets using electrostatic levitation,” *Physical Review B*, vol. 83, no. 10, p. 104205, 2011.

[185] I. Egry and D. Holland-Moritz, “Levitation methods for structural and dynamical studies of liquids at high temperatures,” *The European Physical Journal Special Topics*, vol. 196, no. 1, p. 131, 2011.

[186] F. Yang, T. Kordel, D. Holland-Moritz, T. Unruh, and A. Meyer, “Structural relaxation as seen by quasielastic neutron scattering on viscous Zr–Ti–Cu–Ni–Be droplets,” *Journal of Physics: Condensed Matter*, vol. 23, no. 25, p. 254207, 2011.

[187] K. Kelton, G. Lee, A. K. Gangopadhyay, R. Hyers, T. Rathz, J. Rogers, M. Robinson, and D. Robinson, “First x-ray scattering studies on electrostatically levitated metallic liquids: Demonstrated influence of local icosahedral order on the nucleation barrier,” *Physical Review Letters*, vol. 90, no. 19, p. 195504, 2003.

[188] D. Holland-Moritz, F. Yang, T. Kordel, S. Klein, F. Kargl, J. Gegner, T. Hansen, J. Bednarcik, I. Kaban, O. Shuleshova, N. Mattern, and A. Meyer, "Does an icosahedral short-range order prevail in glass-forming Zr-Cu melts?," *EPL (Europhysics Letters)*, vol. 100, no. 5, p. 56002, 2012.

[189] S. Klein, D. Holland-Moritz, D. Herlach, N. Mauro, and K. Kelton, "Short-range order of undercooled melts of $PdZr_2$ intermetallic compound studied by X-ray and neutron scattering experiments," *EPL (Europhysics Letters)*, vol. 102, no. 3, p. 36001, 2013.

[190] S. Earnshaw, "On the nature of the molecular forces," in *Cambridge Philosophical Society*, vol. 7, pp. 97–112, 1842.

[191] T. Meister, H. Werner, G. Lohoefer, D. Herlach, and H. Unbehauen, "Gain-scheduled control of an electrostatic levitator," *Control Engineering Practice*, vol. 11, no. 2, pp. 117–128, 2003.

[192] I. Jonas, *Thermophysical and structural properties of the equilibrium and undercooled melt of bulk metallic glasses investigated by electrostatic levitation.* PhD thesis, Universität des Saarlandes Saarbrücken, 2016.

[193] I. Egry and J. Brillo, "Surface tension and density of liquid metallic alloys measured by electromagnetic levitation," *Journal of Chemical & Engineering Data*, vol. 54, no. 9, pp. 2347–2352, 2009.

[194] J. Brillo and I. Egry, "Density of multicomponent melts measured by electromagnetic levitation," *Japanese Journal of Applied Physics*, vol. 50, 2011.

[195] J. J. Wessing and J. Brillo, "Density, Molar Volume, and Surface Tensionof Liquid Al-Ti," *Metallurgical and Materials Transactions A*, vol. 48, no. 2, pp. 868–882, 2017.

[196] J. Brillo and I. Egry, "Surface tension of nickel, copper, iron and their binary alloys," *Journal of Materials Science*, vol. 40, no. 9-10, pp. 2213–2216, 2005.

[197] A. Pommrich, A. Meyer, D. Holland-Moritz, and T. Unruh, "Nickel self-diffusion in silicon-rich Si–Ni melts," *Applied Physics Letters*, vol. 92, no. 24, p. 241922, 2008.

[198] J. Horbach, R. Rozas, T. Unruh, and A. Meyer, "Improvement of computer simulation models for metallic melts via quasielastic neutron scattering: A case study of liquid titanium," *Physical Review B*, vol. 80, no. 21, p. 212203, 2009.

[199] A. Meyer, J. Horbach, O. Heinen, D. Holland-Moritz, and T. Unruh, “Self diffusion in liquid titanium: quasielastic neutron scattering and molecular dynamics simulation,” in *Defect and Diffusion Forum*, vol. 289, pp. 609–614, Trans Tech Publ, 2009.

[200] D. Holland-Moritz, T. Schenk, V. Simonet, R. Bellissent, P. Convert, T. Hansen, and D. Herlach, “Short-range order in undercooled metallic liquids,” *Materials Science and Engineering: A*, vol. 375, pp. 98–103, 2004.

[201] D. Holland-Moritz, T. Schenk, V. Simonet, and R. Bellissent, “Short-range order in undercooled and stable melts forming quasicrystals and approximants and its influence on nucleation,” *Philosophical Magazine*, vol. 86, no. 3-5, pp. 255–262, 2006.

[202] I. Egry, G. Lohöfer, I. Seyhan, S. Schneider, and B. Feuerbacher, “Viscosity of eutectic $Pd_{78}Cu_6Si_{16}$ measured by the oscillating drop technique in microgravity,” *Applied Physics Letters*, vol. 73, no. 4, pp. 462–463, 1998.

[203] G. Lohöfer, S. Schneider, and I. Egry, “Thermophysical properties of undercooled liquid $Co_{80}Pd_{20}$,” *International Journal of Thermophysics*, vol. 22, no. 2, pp. 593–604, 2001.

[204] J. Brillo, G. Lohofer, F. Schmidt-Hohagen, S. Schneider, and I. Egry, “Thermophysical property measurements of liquid metals by electromagnetic levitation,” *International Journal of Materials and Product Technology*, vol. 26, no. 3-4, pp. 247–273, 2006.

[205] G. Lohöfer and J. Piller, “The new ISS Electromagnetic Levitation Facility-’MSL-EML’,” in *40th AIAA Aerospace Sciences Meeting & Exhibit*, p. 764, 2002.

[206] D. M. Matson, X. Xiao, J. Rodriguez, and R. K. Wunderlich, “Preliminary experiments using electromagnetic levitation on the International Space Station,” *International Journal of Microgravity Science and Application*, vol. 33, no. 2, p. 330206, 2016.

[207] M. A. Khan, C. Allemand, and T. W. Eagar, “Noncontact temperature measurement. I. Interpolation based techniques,” *Review of Scientific Instruments*, vol. 62, no. 2, pp. 392–402, 1991.

[208] M. K. E. L. Planck, “Zur Theorie des Gesetzes der Energieverteilung in Normalspectrum,” *Verhandlungen der Deutschen Physikalischen Gesellschaft*, vol. 2, p. 237, 1900.

[209] S. Klein, *Nucleation in undercooled melts of pure zirconium and zirconium based alloys.* PhD thesis, Ruhr-Universität Bochum, 2011.

[210] S. Krishnan, C. Anderson, J. Weber, P. Nordine, W. Hofmeister, and R. Bayuzick, “Optical properties and spectral emissivities at 632.8 nm in the titanium-aluminum system,” *Metallurgical Transactions A*, vol. 24, no. 1, pp. 67–72, 1993.

[211] W. Wien, “XXX. On the division of energy in the emission-spectrum of a black body,” *The London, Edinburgh, and Dublin Philosophical Magazine and Journal of Science*, vol. 43, no. 262, pp. 214–220, 1897.

[212] T. Kordel, *Nahordnung und atomare Dynamik in elektrostatisch levitierten Zr-Basis-Schmelzen.* PhD thesis, Ruhr-Universität Bochum, 2012.

[213] T. Unruh, J. Neuhaus, and W. Petry, “The high-resolution time-of-flight spectrometer TOFTOF,” *Nuclear Instruments and Methods in Physics Research Section A: Accelerators, Spectrometers, Detectors and Associated Equipment*, vol. 580, no. 3, pp. 1414–1422, 2007.

[214] W. Lohstroh and Z. Evenson, “TOFTOF: Cold neutron time-of-flight spectrometer,” *Journal of large-scale research facilities*, vol. 1, p. 15, 2015.

[215] J. Wuttke, “Self-absorption coefficient for tubular samples:–Erratum and Addendum to Physica B 266 (1999) 112,” *Physica B: Condensed Matter*, vol. 292, no. 3-4, pp. 194–195, 2000.

[216] J. Wuttke, “FRIDA (fast reliable inelastic data analysis),” 2006.

[217] H. Paalman and C. Pings, “Numerical evaluation of X-ray absorption factors for cylindrical samples and annular sample cells,” *Journal of Applied Physics*, vol. 33, no. 8, pp. 2635–2639, 1962.

[218] T. C. Hansen, P. F. Henry, H. E. Fischer, J. Torregrossa, and P. Convert, “The D20 instrument at the ILL: a versatile high-intensity two-axis neutron diffractometer,” *Measurement Science and Technology*, vol. 19, no. 3, p. 034001, 2008.

[219] D. Swinehart, “The Beer-Lambert Law,” *Journal of Chemical Education*, vol. 39, no. 7, p. 333, 1962.

[220] G. Placzek, "The scattering of neutrons by systems of heavy nuclei," *Physical Review*, vol. 86, no. 3, p. 377, 1952.

[221] J. Yarnell, M. Katz, R. G. Wenzel, and S. Koenig, "Structure factor and radial distribution function for liquid argon at 85 K," *Physical Review A*, vol. 7, no. 6, p. 2130, 1973.

[222] I. Blech and B. Averbach, "Multiple scattering of neutrons in vanadium and copper," *Physical Review*, vol. 137, no. 4A, p. A1113, 1965.

[223] G. Vaughan, J. Wright, A. Bytchkov, C. Curfs, C. Gundlach, M. Orlova, L. Erra, H. Gleyzolle, T. Buslaps, A. Götz, G. Suchet, S. Petitdemange, M. Rossat, L. Margulies, W. Ludwig, A. Snigirev, I. Snigireva, S. Schmidt, H. O. Sørensen, E. M. Lauridsen, U. L. Olsen, J. Oddershede, and H. F. Poulsen, "The extension of ID11 for nanoscale and hierarchical characterization," in *Proceedings of the Risø International Symposium on Materials Science*, vol. 31, pp. 457–476, Risø National Laboratory, 2010.

[224] J.-C. Labiche, O. Mathon, S. Pascarelli, M. A. Newton, G. G. Ferre, C. Curfs, G. Vaughan, A. Homs, and D. F. Carreiras, "The fast readout low noise camera as a versatile x-ray detector for time resolved extended x-ray absorption fine structure and diffraction studies of dynamic problems in materials science, chemistry, and catalysis," *Review of Scientific Instruments*, vol. 78, p. 091301, 2007.

[225] J. Kieffer and J. Wright, "PyFAI: a Python library for high performance azimuthal integration on GPU," *Powder Diffraction*, vol. 28, no. S2, pp. S339–S350, 2013.

[226] L. Brown and R. Feynman, "Radiative corrections to Compton scattering," *Physical Review*, vol. 85, no. 2, p. 231, 1952.

[227] I.-K. Jeong, J. Thompson, T. Proffen, A. Turner, and S. Billinge, "PDFgetX: a program for obtaining the atomic pair distribution function from X-ray powder diffraction data," *Journal of Applied Crystallography*, vol. 34, no. 4, pp. 536–536, 2001.

[228] L. V. Azaroff, "Polarization correction for crystal-monochromatized X-radiation," *Acta Crystallographica*, vol. 8, no. 11, pp. 701–704, 1955.

[229] A. Mallock, "III. Experiments on fluid viscosity," *Philosophical Transactions of the Royal Society of London. Series A, Containing Papers of a Mathematical or Physical Character*, no. 187, pp. 41–56, 1896.

[230] S. Njemirovsky, *Über die hydroschweflige Säure und deren Einwirkung auf Zuckerlösungen.* PhD thesis, Technische Hochschule Wien, 1907.

[231] H. A. Barnes, J. F. Hutton, and K. Walters, *An Introduction to Rheology*, vol. 3. Elsevier Science Publishers, BV, 1989.

[232] I. Egry, H. Giffard, and S. Schneider, "The oscillating drop technique revisited," *Measurement Science and Technology*, vol. 16, no. 2, p. 426, 2005.

[233] A. I. Pommrich, *Selbstdiffusion in siliziumreichen Legierungsschmelzen.* PhD thesis, Ruhr-Universität Bochum, 2010.

[234] S. Schneider, I. Egry, R. Wunderlich, R. Willnecker, and M. Putz, "Evaluation of Thermophysical Data from Electromagnetic Levitation Experiments with Digital Image Processing," *Journal of the Japan Society of Microgravity Application*, vol. 25, no. 3, pp. 387–391, 2008.

[235] L. Rayleigh, "On the capillary phenomena of jets," *Proceedings of the Royal Society of London*, vol. 29, no. 196-199, pp. 71–97, 1879.

[236] T. Ishikawa, P.-F. Paradis, N. Koike, and Y. Watanabe, "Effects of the positioning force of electrostatic levitators on viscosity measurements," *Review of Scientific Instruments*, vol. 80, no. 1, p. 013906, 2009.

[237] P. Heintzmann, *Untersuchungen der Zusammenhänge von atomarer Struktur, Selbstdiffusion, Interdiffusion und Viskosität in flüssigen Zr-Ni Legierungen.* PhD thesis, Ruhr-Universität Bochum, 2016.

[238] V. L. Stout and M. D. Gibbons, "Gettering of gas by titanium," *Journal of Applied Physics*, vol. 26, no. 12, pp. 1488–1492, 1955.

[239] E. Cussler, *Diffusion: Mass Transfer in Fluid Systems.* Cambridge Series in Chemical Engineering, Cambridge University Press, 2009.

[240] G. Mathiak, A. Griesche, K. Kraatz, and G. Frohberg, "Diffusion in liquid metals," *Journal of Non-Crystalline Solids*, vol. 205-207, pp. 412 – 416, 1996. Ninth International Conference on Liquid and Amorphous Metals.

[241] K. Sommer and J. Poziemski, "Density, thermal expansion and compressibility of mercury," *Metrologia*, vol. 30, no. 6, p. 665, 1994.

[242] R. Hoffman, “The Self-Diffusion of Liquid Mercury,” *The Journal of Chemical Physics*, vol. 20, no. 10, pp. 1567–1570, 1952.

[243] R. E. Meyer, “Self-diffusion of liquid mercury,” *The Journal of Physical Chemistry*, vol. 65, no. 3, pp. 567–568, 1961.

[244] D. Brown and D. Tuck, “New method for studying self-diffusion in liquids: self-diffusion in liquid mercury,” *Transactions of the Faraday Society*, vol. 60, pp. 1230–1235, 1964.

[245] N. H. Nachtrieb and J. Petit, “Self-diffusion in liquid mercury,” *The Journal of Chemical Physics*, vol. 24, no. 4, pp. 746–750, 1956.

[246] L. Bove, F. Sacchetti, C. Petrillo, B. Dorner, F. Formisano, and F. Barocchi, “Neutron investigation of the ion dynamics in liquid mercury: Evidence for collective excitations,” *Physical Review Letters*, vol. 87, no. 21, p. 215504, 2001.

[247] L. Bove, F. Sacchetti, C. Petrillo, B. Dorner, F. Formisano, M. Sampoli, and F. Barocchi, “Self-dynamics and collective dynamics of liquid mercury,” *Philosophical Magazine B*, vol. 82, no. 3, pp. 365–374, 2002.

[248] Y. S. Badyal, U. Bafile, K. Miyazaki, I. M. de Schepper, and W. Montfrooij, “Cage diffusion in liquid mercury,” *Physical Review E*, vol. 68, no. 6, p. 061208, 2003.

[249] S. Hosokawa, H. Sinn, F. Hensel, A. Alatas, E. Alp, and W.-C. Pilgrim, “Collective dynamics of liquid Hg investigated by inelastic X-ray scattering,” *Journal of Non-Crystalline Solids*, vol. 312, pp. 163–167, 2002.

[250] E. d. C. Andrade, “A theory of the viscosity of liquids,” *Philosophical Magazine*, vol. 17, p. 497, 1934.

[251] F. A. Lindemann, “Über die Berechnung molekularer Eigenfrequenzen,” *Physikalische Zeitschrift*, vol. 11, no. 14, pp. 609–612, 1910.

[252] J. Qvist, H. Schober, and B. Halle, “Structural dynamics of supercooled water from quasielastic neutron scattering and molecular simulations,” *The Journal of Chemical Physics*, vol. 134, no. 14, p. 144508, 2011.

[253] C. C. Miller, “The Stokes-Einstein law for diffusion in solution,” *Proceedings of the Royal Society of London. Series A, Containing Papers of a Mathematical and Physical Character*, vol. 106, no. 740, pp. 724–749, 1924.

[254] M. H. Jacobs, *Diffusion processes.* Springer, 1935.

[255] M. J. Assael, I. J. Armyra, J. Brillo, S. V. Stankus, J. Wu, and W. A. Wakeham, "Reference Data for the Density and Viscosity of Liquid Cadmium, Cobalt,Gallium, Indium, Mercury, Silicon, Thallium, and Zinc," *Journal of Physical and Chemical Reference Data*, vol. 41, no. 3, p. 033101, 2012.

[256] A. Kasama, T. Iida, and Z.-i. Morita, "Viscosity of mercury-based dilute binary alloys," *Transactions of the Japan Institute of Metals*, vol. 16, no. 8, pp. 527–536, 1975.

[257] L. Bosio, R. Cortes, and C. Segaud, "X-ray diffraction study of liquid mercury over temperature range 173 to 473 K," *The Journal of Chemical Physics*, vol. 71, no. 9, pp. 3595–3600, 1979.

[258] Y. Waseda, *The structure of non-crystalline materials: liquids and amorphous solids.* Advanced Book Program, McGraw-Hill International Book Co., 1980.

[259] J. Brillo, A. I. Pommrich, and A. Meyer, "Relation between Self-Diffusion and Viscosity in Dense Liquids: New Experimental Results from Electrostatic Levitation," *Physical Review Letters*, vol. 107, p. 165902, Oct 2011.

[260] G. Kidson, "On the anomalous self-diffusion in body-centered cubic zirconium," *Canadian Journal of Physics*, vol. 41, no. 10, pp. 1563–1570, 1963.

[261] J. M. Sanchez and D. De Fontaine, "Model for anomalous self-diffusion in group-IV B transition metals," *Physical Review Letters*, vol. 35, no. 4, p. 227, 1975.

[262] C. Herzig and U. Köhler, "Anomalous Self-Diffusion in BCC IVB Metals and Alloys," in *Materials Science Forum*, vol. 15, pp. 301–322, Trans Tech Publ, 1987.

[263] M. Köppers, C. Herzig, M. Friesel, and Y. Mishin, "Intrinsic self-diffusion and substitutional Al diffusion in α-Ti," *Acta Materialia*, vol. 45, no. 10, pp. 4181–4191, 1997.

[264] J. Horvath, F. Dyment, and H. Mehrer, "Anomalous self-diffusion in a single crystal of α-zirconium," *Journal of Nuclear Materials*, vol. 126, no. 3, pp. 206–214, 1984.

[265] C. Herzig and H. Eckseler, "On the anomalous self-diffusion in β-zirconium: Temperature dependence of the isotope effect," *Zeitschrift für Metallkunde*, vol. 70, no. 10, pp. 215–223, 1979.

[266] J. Murray, "The Ti-Zr (Titanium-Zirconium) system," *Bulletin of Alloy Phase Diagrams*, vol. 2, no. 2, pp. 197–201, 1981.

[267] D. Shechtman, I. Blech, D. Gratias, and J. W. Cahn, "Metallic phase with long-range orientational order and no translational symmetry," *Physical Review Letters*, vol. 53, no. 20, p. 1951, 1984.

[268] K. Kelton, W. Kim, and R. Stroud, "A stable Ti-based quasicrystal," *Applied Physics Letters*, vol. 70, no. 24, pp. 3230–3232, 1997.

[269] K. Kelton, A. Gangopadhyay, G. Lee, L. Hannet, R. W. Hyers, S. Krishnan, M. B. Robinson, J. Rogers, and T. J. Rathz, "X-ray and electrostatic levitation undercooling studies in Ti–Zr–Ni quasicrystal forming alloys," *Journal of Non-Crystalline Solids*, vol. 312, pp. 305–308, 2002.

[270] D. Holland-Moritz, D. M. Herlach, and K. F. Kelton, "Unterkühlt und dicht gepackt," *Physik Journal*, vol. 4, no. 4, p. 38, 2005.

[271] N. N. Greenwood and A. Earnshaw, *Chemistry of the Elements*. Elsevier, 2012.

[272] G. B. Skinner and H. L. Johnston, "Thermal expansion of zirconium between 298 K and 1600 K," *The Journal of Chemical Physics*, vol. 21, no. 8, pp. 1383–1384, 1953.

[273] S. Jeon, D.-H. Kang, Y. Lee, S. Lee, and G. Lee, "Effect of atomic size on undercoolability of binary solid solution alloy liquids with Zr, Ti, and Hf using electrostatic levitation," *The Journal of Chemical Physics*, vol. 145, no. 17, p. 174504, 2016.

[274] J. K. Percus and G. J. Yevick, "Analysis of classical statistical mechanics by means of collective coordinates," *Physical Review*, vol. 110, no. 1, p. 1, 1958.

[275] W. Götze and T. Voigtmann, "Effect of composition changes on the structural relaxation of a binary mixture," *Physical Review E*, vol. 67, no. 2, p. 021502, 2003.

[276] C. Chen, J. Huang, H. Chou, Y. Lai, L. Chang, X. Du, J. Chu, and T. Nieh, "On the amorphous and nanocrystalline Zr–Cu and Zr–Ti co-sputtered thin films," *Journal of Alloys and Compounds*, vol. 483, no. 1-2, pp. 337–340, 2009.

[277] M. Ashby and A. Greer, "Metallic glasses as structural materials," *Scripta Materialia*, vol. 54, no. 3, pp. 321–326, 2006.

[278] A. L. Greer and E. Ma, "Bulk metallic glasses: at the cutting edge of metals research," *Materials Research Bulletin*, vol. 32, no. 8, pp. 611–619, 2007.

[279] A. L. Greer, "Metallic glasses… on the threshold," *Materials Today*, vol. 12, no. 1-2, pp. 14–22, 2009.

[280] A. Inoue, T. Zhang, and T. Masumoto, "Zr–Al–Ni amorphous alloys with high glass transition temperature and significant supercooled liquid region," *Materials Transactions, JIM*, vol. 31, no. 3, pp. 177–183, 1990.

[281] H. Choi-Yim, D. Xu, and W. L. Johnson, "Ni-based bulk metallic glass formation in the Ni–Nb–Sn and Ni–Nb–Sn–X (X= B, Fe, Cu) alloy systems," *Applied Physics Letters*, vol. 82, no. 7, pp. 1030–1032, 2003.

[282] P. Gargarella, S. Pauly, M. De Oliveira, U. Kühn, and J. Eckert, "Glass formation in the Ti–Cu system with and without Si additions," *Journal of Alloys and Compounds*, vol. 618, pp. 413–420, 2015.

[283] A. Inoue, T. Zhang, and T. Masumoto, "Glass-forming ability of alloys," *Journal of Non-Crystalline Solids*, vol. 156, pp. 473–480, 1993.

[284] H.-K. Kim, M. Lee, K.-R. Lee, and J.-C. Lee, "How can a minor element added to a binary amorphous alloy simultaneously improve the plasticity and glass-forming ability?," *Acta Materialia*, vol. 61, no. 17, pp. 6597–6608, 2013.

[285] X. Wang, Q. Jiang, Q. Cao, J. Bednarcik, H. Franz, and J. Jiang, "Atomic structure and glass forming ability of $Cu_{46}Zr_{46}Al_8$ bulk metallic glass," *Journal of Applied Physics*, vol. 104, no. 9, p. 093519, 2008.

[286] Y. Cheng, E. Ma, and H. Sheng, "Atomic level structure in multicomponent bulk metallic glass," *Physical Review Letters*, vol. 102, no. 24, p. 245501, 2009.

[287] W. Wang, J. Lewandowski, and A. Greer, "Understanding the glass-forming ability of $Cu_{50}Zr_{50}$ alloys in terms of a metastable eutectic," *Journal of Materials Research*, vol. 20, no. 9, pp. 2307–2313, 2005.

[288] L. Shadowspeaker and R. Busch, "On the fragility of Nb-Ni-based and Zr-based bulk metallic glasses," *Applied Physics Letters*, vol. 85, no. 13, pp. 2508–2510, 2004.

[289] R. Busch, J. Schroers, and W. Wang, "Thermodynamics and kinetics of bulk metallic glass," *Materials Research Bulletin*, vol. 32, no. 8, pp. 620–623, 2007.

[290] J. Heinrich, R. Busch, F. Müller, S. Grandthyll, and S. Hüfner, “Role of aluminum as an oxygen-scavenger in zirconium based bulk metallic glasses,” *Applied Physics Letters*, vol. 100, no. 7, p. 071909, 2012.

[291] O. Senkov and D. Miracle, “Effect of the atomic size distribution on glass forming ability of amorphous metallic alloys,” *Materials Research Bulletin*, vol. 36, no. 12, pp. 2183–2198, 2001.

[292] R. Busch, “The thermophysical properties of bulk metallic glass-forming liquids,” *JOM*, vol. 52, no. 7, pp. 39–42, 2000.

[293] G. Chen, X. Hui, S. Fan, H. Kou, and K. Yao, “Concept of chemical short range order domain and the glass forming ability in multicomponent liquid,” *Intermetallics*, vol. 10, no. 11-12, pp. 1221–1232, 2002.

[294] N. Jakse and A. Pasturel, “Local Order of Liquid and Supercooled Zirconium by Ab Initio Molecular Dynamics,” *Physical Review Letters*, vol. 91, p. 195501, Nov 2003.

[295] H. Sheng, W. Luo, F. Alamgir, J. Bai, and E. Ma, “Atomic packing and short-to-medium-range order in metallic glasses,” *Nature*, vol. 439, no. 7075, pp. 419–425, 2006.

[296] N. Jakse and A. Pasturel, “Glass forming ability and short-range order in a binary bulk metallic glass by ab initio molecular dynamics,” *Applied Physics Letters*, vol. 93, no. 11, p. 113104, 2008.

[297] A. E. Lagogianni, J. Krausser, Z. Evenson, K. Samwer, and A. Zaccone, “Unifying interatomic potential, g(r), elasticity, viscosity, and fragility of metallic glasses: analytical model, simulations, and experiments,” *Journal of Statistical Mechanics: Theory and Experiment*, vol. 2016, no. 8, p. 084001, 2016.

[298] D. Arias and J. Abriata, “Cu-Zr (copper-zirconium),” *Journal of Phase Equilibria*, vol. 11, no. 5, pp. 452–459, 1990.

[299] J. Gegner, O. Shuleshova, R. Kobold, D. Holland-Moritz, F. Yang, W. Hornfeck, J. Bednarcik, and D. Herlach, “In situ observation of the phase selection from the undercooled melt in Cu–Zr,” *Journal of Alloys and Compounds*, vol. 576, pp. 232–235, 2013.

[300] J. Heinrich, R. Busch, and B. Nonnenmacher, “Processing of a bulk metallic glass forming alloy based on industrial grade Zr,” *Intermetallics*, vol. 25, pp. 1–4, 2012.

[301] D. Holland-Moritz, *Ordnungsphänomene, fest-flüssig Grenzfläche und Phasenselektionsverhalten in unterkühlten Metallschmelzen.* Habilitation, Ruhr-Universität Bochum, 01 2003.

[302] M. Patty, K. Schoen, W. Montfrooij, and Z. Yamani, “Polarized neutron scattering investigation of excitations at low momentum transfer in liquid Ga: The mystery continues,” *Journal of Non-Crystalline Solids*, vol. 357, no. 3, pp. 1000–1003, 2011.

[303] S. Cajahuaringa, M. de Koning, and A. Antonelli, “Dynamics near a liquid-liquid phase transition in a non-tetrahedral liquid: The case of gallium,” *The Journal of Chemical Physics*, vol. 136, no. 6, p. 064513, 2012.

[304] S. Cajahuaringa, M. de Koning, and A. Antonelli, “Revisiting dynamics near a liquid-liquid phase transition in Si and Ga: The fragile-to-strong transition,” *The Journal of Chemical Physics*, vol. 139, no. 22, p. 224504, 2013.

[305] J. Trampenau, A. Heiming, W. Petry, M. Alba, C. Herzig, W. Miekeley, and H. Schober, “Phonon dispersion of the bcc phase of group-IV metals. III. bcc hafnium,” *Physical Review B*, vol. 43, no. 13, p. 10963, 1991.

[306] W. Petry, “Phonons at martensitic phase transitions of bcc-Ti, bcc-Zr and bcc-Hf,” *Phase Transitions*, vol. 31, no. 1-4, pp. 119–136, 1991.

[307] W. Petry, A. Heiming, C. Herzig, and J. Trampenau, “On the Diffusion Mechanism in bcc Metals, a Neutron Scattering Approach,” in *Defect and Diffusion Forum*, vol. 75, pp. 211–228, Trans Tech Publ, 1991.

[308] W. Petry, “Dynamical precursors of martensitic transitions,” *Le Journal de Physique IV*, vol. 5, no. C2, pp. C2–15, 1995.

[309] S. Szabó and Z. Evenson, “Self-diffusion in liquid Al-Ge investigated with quasielastic neutron scattering,” *Applied Physics Letters*, vol. 110, no. 16, p. 161903, 2017.

List of Figures

2.1 The two main types of diffusion processes, where (a.) refers to self-diffusion and (b.) to inter-diffusion at the interface between two substances 8

2.2 The general geometry of an experiment, where an incident beam is scattered by a sample. E indicates the energy and $\vec{k}$ the wave vector [108] . . . 14

2.3 a. Pair correlation, where a particle j is at time t in position $\vec{r}$ and a particle j' has been in the origin $\vec{r} = 0$ at time $t = 0$; b. self correlation, where one and the same particle is at time t when it has been in the origin $\vec{r} = 0$ at time $t = 0$. 18

2.4 Schematic of different excitation modes and their resulting scattering contributions in the dynamic structure factor $S(Q, \omega)$ [114] 19

2.5 Scattering length b in fm as a function of the atomic number Z of elements [123]. Some elements are labeled. Here, the red lines refer to elements with positive scattering length and the blue lines to elements with negative scattering length. Unmarked elements are referred by green lines. 23

2.6 Schematic 2D model of a monoatomic melt to visualize the "cage effect" in MCT. The red sphere depicts the center atom, which is surrounded by the cage formed by the violet atoms. 26

2.7 Schematic model of viscosity η. A is the surface layer of the liquid, where the force F causes a displacement with the velocity profile $\frac{dv}{dy}$ 28

3.1 Schematic sketch of a sample processed in electrostatic levitation (ESL). The sample is levitated between the top and bottom electrode. The four surrounding electrodes control the horizontal sample position. [192] 33

3.2 A molten metallic sample in electrostatic levitation (ESL). Image by courtesy of DLR-MP. 34

3.3 Sketch of the occurring Lorenz force in electromagnetic levitation (EML). Drawing by courtesy of DLR-MP. 35

3.4 A molten metallic sample in electromagnetic levitation (EML). The sample is levitated and heated by the coil system. Gas cooling can be applied through the bottom nozzle. Image by courtesy of DLR-MP. 36

3.5 Detailed sketch of the multi-disc chopper time-of-flight spectrometer TOFTOF at the Heinz Maier Leibnitz Zentrum (MLZ) in Munich. Drawing by courtesy of TUM-MLZ. 39

3.6 (a) Picture of a chopper disc; (b) illustration of the chopper rotation frequency according to equation 3.7. Figure and graph by courtesy of TUM-MLZ. 40

3.7 (a) Calculated elastic line widths for different chopper frequency; (b) accessible dynamic range with respect to the incident neutron wavelength. Graphs by courtesy of TUM-MLZ. 42

3.8 Measured time-of-flight spectra of a $Zr_{50}Cu_{50}$ at 1208 K (green) when compared to the empty ESL furnace (grey). The quasielastic broadening of the elastic line of the liquid sample is depicted, which shows a two orders of magnitude larger intensity then the background. 43

3.9 Schematic view of the high intensity 2-axis diffractometer D20 at the Institute-Laue Langevin (ILL) in Grenoble, France [218] 45

3.10 Electromagnetic levitator (EML) installed at the instrument D20. Photo by courtesy of DLR-MP. 46

3.11 Electrostatic levitator (ESL) installed at the materials science beamline ID11 at the European Synchrotron Radiation Facility (ESRF) in Grenoble, France 47

3.12 Sketch of the density measurement setup in electrostatic levitation (ESL) . 49

3.13 Damped oscillations of a $Cu_{41}Ti_{59}$ alloy at 1240 K as ivestigated in electrostatic levitation (ESL). The insert shows an detailed view of the change in sample radius in the time range between 0 and 0.05 seconds. 51

4.1 Schematic view of the assembly of the sample cell at TOFTOF to measure scattered neutrons in reflection geometry. 56

4.2 Explosion sketch of the constructed sample cell for the mercury measurement made out of Polytetrafluorethylene (Teflon) (brown). The mount (grey) is made out of Aluminum. 57

4.3 Thermal analysis of the sample cell for the mercury measurement heated by the sample stick. In the sample position an isothermal temperature distribution is noticeable. 57

4.4 Dynamic structure factor $S(Q,\omega)$ of Hg at two temperatures 240 K (blue) and 350 K (red) and a Q-value of 1 Å^{-1}. The spectra are fitted with a Lorentzian function convoluted with the instrumental resolution function (black dashed line). In the insert the resulting HWHMs as a function of Q^2 are shown for both temperatures. Due to the reflection scattering geometry the elastic contribution is dominated by the Nb-lid of the sample cell and is excluded from the evaluation. 59

4.5 Self-diffusion coefficients of Mercury measured with QENS compared to previous measurements available in the literature [242–246, 248] as a function of inverse temperature. 61

4.6 Self-diffusion coefficients of pure metals and water at their respective melting points [51–57, 252] as a function of $V_{m,M}^{\frac{1}{3}} T_m^{\frac{1}{2}} M_m^{-\frac{1}{2}}$. The line is a linear fit to the values according to equation 4.4. 63

4.7 Activation energy of self-diffusion for pure alkali metals, Mercury and water as a function of the the melting temperature. The line is a linear fit to the values for the alkali metals according to equation 4.5 with $B = 3.11$. 63

4.8 Temperature dependence of viscosity of Mercury. The measurement error is smaller than the size of the symbols and of about 0.2 %. Concrete values can be found in [256]. 66

4.9 Temperature dependence of the diffusion-viscosity relation in Mercury when compared with the Stokes-(Sutherland-)Einstein relation (solid line). The dashed line would hold if $D\eta$ would be a temperature independent constant. 66

4.10 Radial distribution function of Mercury at temperatures of 173 K, 293 K, and 473 K; obtained from the Fourier transformed liquid structure factor investigated with x-ray diffraction [257]. 68

4.11 The phase diagram of the Zr-Ti system [266]. The left side refers to pure Titanium and the right side to pure Zirconium. 71

4.12 Comparison of self-diffusion coefficient in different phases of Zirconium and Titanium. All shown data can be found in literature: Liquid Ti [198], α-Ti [263], β-Ti [27], α-Zr [264], β-Zr [265]. 71

4.13 The liquid structure factor of melts of the zero scattering $Zr_{32.4}Ti_{67.6}$ composition (red) and Zr_2Ti composition (green) at a temperature of 1420 K investigated using neutron diffraction and processed by electromagnetic levitation. 74

4.14 Comparison of the liquid structure factor of zero scattering $Zr_{32.4}Ti_{67.6}$ melt as seen by neutron diffraction (red) and x-ray diffraction (blue). . . . 74

4.15 Comparison of the total structure factors of binary Zr-Ti melts with composition $Zr_{15}Ti_{85}$ (violet), $Zr_{32.4}Ti_{67.6}$ (red), $Zr_{50}Ti_{50}$ (blue) and Zr_2Ti (green), investigated using x-ray diffraction and compared to the liquid structure factors of pure Titanium (orange) [66] and pure Zirconium (black) [65] at $T = 1900$ K. 76

4.16 Comparison of the total x-ray structure factor of melts with different Zr-Ti compositions normalized over the structure factor maximum at $T = 1900$ K. 76

4.17 Fit of the liquid structure factor of raw Titanium at $T = 1845$ K assuming different short-range structures of icosahedral, dodecahedral or fcc type [66]. The short-range order of the measured melt is best described by an icosahedral one. 77

4.18 Concentration and temperature dependent density of Zr-Ti melts with various compositions measured in ESL [273]. The error is smaller than the size of the symbols. 79

4.19 Concentration dependency of the molar volume and inserted respective packing fraction of Zr-Ti alloys as deduced from the density data at $T = 1850$ K. The color code is alike the other graphs in this work and unlike Fig. 4.18. 79

4.20 Dynamic structure factor $S(Q,\omega)$ at a Q-value of 0.4 Å^{-1} of $Zr_{50}Ti_{50}$ at two temperatures 1870 K (blue) and 2000 K (red) (top) and of $Zr_{15}Ti_{85}$ at two temperatures 1820 K (blue) and 2020 K (red) (bottom). The spectra are fitted with a Lorentzian function convoluted with the instrumental resolution function (black dashed line). In the inserts the resulting HWHMs as a function of Q^2 are shown for both respective temperatures. 82

4.21 Temperature dependent self-diffusion coefficients of $Zr_{15}Ti_{85}$ (violet), $Zr_{32.4}Ti_{67.6}$ (red), $Zr_{50}Ti_{50}$ (blue) and Zr_2Ti (green) composition when compared to the self-diffusion coefficients of pure Titanium (orange) [198]. 83

4.22 Self-diffusion coefficients of $Zr_{15}Ti_{85}$ (violet), $Zr_{32.4}Ti_{67.6}$ (red), $Zr_{50}Ti_{50}$ (blue) and Zr_2Ti (green) and pure Titanium (orange) [198] at $T = 1973$ K. 84

4.23 Dynamic structure factor $S(Q,\omega)$ of pure Zirconium processed by electromagnetic levitation at $T = 2123$ K, investigated for 1h at TOFTOF. The different colors refer to different momentum transfers. 84

4.24 Comparison of MCT calculations with measured self-diffusion coefficients of $Zr_{15}Ti_{85}$ (violet), $Zr_{32.4}Ti_{67.6}$ (red), $Zr_{50}Ti_{50}$ (blue) and Zr_2Ti (green) compositions and pure Titanium (orange) [198] at $T = 1973$ K. 87

4.25 Improved glass-forming ability of Zr-Cu alloys with minor Aluminum and Titanium additions. Shown is the increase in critical casting thickness dc from 2 mm in case of the binary $Zr_{50}Cu_{50}$ to 5 mm in case of the ternary $(Zr_{50}Cu_{50})_{96}Al_4$ [77]. 90
4.26 The liquid structure factor of $Zr_{50}Cu_{50}$ (blue), $(Zr_{50}Cu_{50})_{96}Al_4$ (red) and $(Zr_{50}Cu_{50})_{96}Ti_4$ (green) melts at 1175 K, measured by synchrotron X-ray diffraction. 93
4.27 Temperature dependent packing fraction in $Zr_{50}Cu_{50}$ (blue), $(Zr_{50}Cu_{50})_{96}Al_4$ (red) and $(Zr_{50}Cu_{50})_{96}Ti_4$ (green) alloys as as calculated from the macroscopic density. 93
4.28 Temperature dependent viscosity in $Zr_{50}Cu_{50}$ (blue squares), $(Zr_{50}Cu_{50})_{96}Al_4$ (red diamonds) and $(Zr_{50}Cu_{50})_{96}Ti_4$ (green dots) alloys as determined by the oscillated droplet method in electrostatic levitation. 94
4.29 Self-diffusion coefficients of $Zr_{50}Cu_{50}$ (blue squares), $(Zr_{50}Cu_{50})_{96}Al_4$ (red diamonds) and $(Zr_{50}Cu_{50})_{96}Ti_4$ (green dots) melts, investigated with quasielastic neutron scattering. The lines refer to Arrhenius fits of the measured values. 97
4.30 Temperature-time profile of the processing of $(Zr_{50}Cu_{50})_{96}Al_4$ (red) and $(Zr_{50}Cu_{50})_{96}Ti_4$ (green) alloys in electrostatic levitation. Different solidification paths with two solidification events (left) or one solidification event (right) are observed. 99
4.31 Diffractograms of $(Zr_{50}Cu_{50})_{96}Al_4$ (top) and $(Zr_{50}Cu_{50})_{96}Ti_4$ (bottom) alloys after both solidification paths. The red fits shows the phase selection of the Rietveld analysis. The respective phases are indicated. 100
4.32 The phase diagram of the Zr-Cu system [298]. The left side refers to Copper and the right side to Zirconium. 101
4.33 Pictures of detected backscattered electrons in SEM of Zr-Cu with minor Al additions after different solidification paths. The top one refers to solidification with two crystallization events and the bottom one to solidification after a single crystallization event. 102

5.1 Self-diffusion coefficients measured by quasielastic neutron scattering for binary $Cu_{68}Si_{32}$ (blue) and $Cu_{81}Si_{19}$ (red) and compared to liquid pure Copper (green)[54]. The lines refer to Arrhenius fits of the measured values. 110

List of Tables

1 Self-diffusion coefficients of Mercury measured with quasielastic neutron scattering . . . 112

2 Self-diffusion coefficients of Zr_2Ti measured with quasielastic neutron scattering . . . 113

3 Self-diffusion coefficients of $Zr_{50}Ti_{50}$ measured with quasielastic neutron scattering . . . 113

4 Self-diffusion coefficients of $Zr_{32.4}Ti_{67.4}$ measured with quasielastic neutron scattering . . . 113

5 Self-diffusion coefficients of $Zr_{15}Ti_{85}$ measured with quasielastic neutron scattering . . . 113

6 Self-diffusion coefficients of $Zr_{50}Cu_{50}$ measured with quasielastic neutron scattering . . . 114

7 Self-diffusion coefficients of $(Zr_{50}Cu_{50})_{96}Al_4$ measured with quasielastic neutron scattering . . . 114

8 Self-diffusion coefficients of $(Zr_{50}Cu_{50})_{96}Ti_4$ measured with quasielastic neutron scattering . . . 114

9 Viscosity of $Zr_{50}Cu_{50}$ measured in electrostatic levitation employing the oscillated droplet method . . . 115

10 Viscosity of $(Zr_{50}Cu_{50})_{96}Al_4$ measured in electrostatic levitation employing the oscillated droplet method . . . 116

11 Viscosity of $(Zr_{50}Cu_{50})_{96}Ti_4$ measured in electrostatic levitation employing the oscillated droplet method . . . 117

Copyright permissions

Figure	Permission
2.2	permitted by FZ Jülich GmbH, Zentralbibliothek
2.5	permitted by Birkbeck College, London
3.1	permitted by DLR-MP
3.3	permitted by DLR-MP
3.9	License Order N°1039243-1
4.8	permitted by The Japan Institute of Metals and Materials
4.10	License N°4841241041720
4.11	License N°4841250807051
4.17	License N°4841250217460
4.18	License N°4841250330452
4.25	License N°4841250449605
4.32	License N°4841250602550

Copyright permissions for reused published material

Acknowledgments

This is the place to acknowledge all the people for their contribution to this work.

Primary I thank Prof. Dr. Winfried Petry (TUM) for supervising my doctoral research and his never ending support on various topics.

Another special thank to Prof. Dr. Dirk Holland-Moritz (DLR) for critical reviewing this work and many hours of discussion, suggestions, providing the levitation facilities, as well as help during beam time.

I thank my supervisors Dr. Fan Yang (DLR) and Dr. Zach Evenson (TUM) for countless suggestions, ideas, discussion, support, constructive criticism and above all patience.

Generally, I thank all members of the Institut für Materialphysik im Weltraum at Deutschen Zentrum für Luft und Raumfahrt (DLR) and especially Prof. Dr. Andreas Meyer and his deputy Prof. Dr. Florian Kargl for the friendly integration to their environment and the good cooperation.

I thank Prof. Dr. Thomas Voigtmann and Julian Reichert (both DLR) for the introduction to mode-coupling theory and helpful discussions to various theoretical topics.

Furthermore, I gratefully acknowledge Dr. Wiebke Lohstroh, Dr. Michael Leitner and Dr. Jürgen Neuhaus (all TUM) for their contentious support at MLZ.

Another thank to all beam line scientists at the large scale facilities, were we carried out experiments. Those are Dr. Marcell Wolf (TOFTOF, MLZ), Dr. Thomas Buslaps (ID11, ESRF) and Dr. Thomas Hansen (D20, ILL). Furthermore, I acknowledge the respective technicians and the radiation protection crew.

Thanks to everyone, who helped during beam time. Those are Dr. Benedikt Nowak, Dr. Sarah Nell, Dr. Patrick Fopp, Dr. Elke Sondermann, Johanna Wilden, Toni Schiller, Tobias Aumüller (all DLR), Dr. Benedikt Bochtler, Dr. Alexander Kuball (both Universität

des Saarlandes), Prof. Dr. Chenchen Yuan (Southeast University of China) and Prof. Dr. Robert W. Hyers (University of Massachusetts).

I want to thank Dr. Matthias Kolbe (DLR) for analyzing my samples at the scanning electron microscope (SEM) and the constructive discussions.

Stefan Burggraf (DLR) is gratefully acknowledged for the winding of the EML coils and the exchange.

A special thank to my fellow office mates Dr. Luca Silvi (TUM) and Raphael Kessler (DLR) for the discussions and friendly atmosphere you created. It's a pleasure to thank Raphael Kessler for the construction and drawing of the Mercury sample cell.

Another thank to Prof. Dr. Matthias Sperl, P.D. Dr. Jürgen Brillo, Dr. Georg Lohöfer, Dr. Mareike Wegener, Dr. Isabell Neumann, Dr. Marc Engelhardt, Dr. Raphael Kobold, Dr. Dirk Bäuer, Dr. Anthony Rawson, Jonathan Ónody, Juliane Baumann and Thomas Werner (all DLR), Dr. Marcus Reinartz (Universität Jena) and Sebastian Biesenkamp (University of Cologne) for daily discussions, assistance and time in the lab.

Theodora Kennel and Armin Kriele (both MLZ) is thanked for the lab environment and safely handling of the Mercury.

I thank the TEMPUS crew for the support during the parabolic flight campaign.

Thanks also to Konstantin Afanasev, Horst Esser and Matthias Nell of the DLR-MP work shop for manufacturing many parts and components for our beam times.

Last but not least a big thank to all my family and friends for continuous backing and everyone I forgot.

This research was partially supported by the German Research Foundation (DFG) via Grant No. EV211/2-1.